COMPUTATIONAL FLUID–STRUCTURE INTERACTION OF SOFT TISSUES USING AN IMMERSED-BOUNDARY METHOD

BY
Ye Chen

Dissertation
Submitted to the Faculty of the
Graduate School of Vanderbilt University
in partial fulfillment of the requirements
for the degree of

DOCTOR OF PHILOSOPHY
in
Mechanical Engineering

February 29, 2020

Nashville, Tennessee

Approved:
Professor Haoxiang Luo, Chair
Professor Robert W. Pitz
Professor Caglar Oskay
Professor D. Greg Walker
Professor Deyu Li

To my grandparents

for their endless supply of love and support.

ACKNOWLEDGMENTS

The journey of pursuing the doctorate degree has been tough with joy. Along this journey, there have been many to whom I owe my gratitude.

First and foremost, I would like to express my sincere gratitude to my adviser, Prof. Haoxiang Luo, for his endless support, guidance, and encouragement. He has been continuously providing insightful advice on my research and encouraging me to develop professional research habits. I thank him for carefully reading, commenting, revising and polishing the manuscripts for publication. In addition, I have also learned from him how to build and expand my network for later career development. Besides, I am grateful for his great efforts of sharing plenty of possible career opportunities with me. It is a precious privilege for me to have the experience of working with him.

I am also profoundly grateful to Prof. Robert Pitz, Prof. Caglar Oskay, Prof. Greg Walker and Prof. Deyu Li. for serving on my dissertation committee and providing constructive comments and suggestions on my dissertation. Besides, I feel so fortunate to have the opportunity of learning from their courses such as Gas Dynamics, Advanced Solid Mechanics, Thermodynamics, and Microfluidics. These courses greatly expanded my knowledge and provided the fundamental training of my doctorate degree.

I owe my great thanks to Dr. Ng Kam and Dr. Brad Coltrain at Kodak Research Lab, Rochester, NY. It has been a great experience to work under their guidance and learn from them during the 12-week stay as a summer intern in 2017.

Special thanks go to my former and current labmates, Dr. Fangbao Tian, Dr. Zheng Li, Dr. Jialei song, Dr. Siyuan Chang, Dr. Yang Zhang, Dr. Yingkun Li and Yi Song, for their helpful discussion in research and companion of friendship. Thanks also go to all my friends during my stay at Vanderbilt University. They have made the time I spent in Nashville enjoyable, meaningful, and unforgettable.

Most importantly, none of my work would have been accomplished without the unconditional love of my family. I am so grateful for their firm faith in knowledge that has been consistently passed on and rooted in my heart.

Table of Contents

Page

List of Figures

Figure **Page**

List of Tables

Table **Page**

Chapter I

Introduction

Fluid–structure interaction (FSI) is the mechanical interaction of some movable or deformable solid structures with an internal or surrounding fluid flow. It represents a class of continuum-mechanics problems with mutual dependence between the fluid and structural mechanics. The fluid mechanics depends on the instantaneous shape and motion of the structure, and on the other hand, the motion and deformation of the structure depend on the fluid forces acting on the surface of the structure as part of the loading.

FSI is almost ubiquitous in our daily lives. Multiple FSI problems are the research subjects in the field of engineering, such as fluttering of aircraft wings, elastic deformation of wind turbine blades, and the dam-break flow impacting on the wall. FSI problems are also widely seen in the field of biological sciences. For instance, different species of birds and fishes are studied from an FSI point of view in order to improve the understanding of their efficient flying or swimming mechanisms through flexible wings or fins. In particular, FSI finds a lot of its applications within the human body. For example, the interaction between blood flow and a deformable vessel provides understanding of the major physical changes (dilation and stiffening) seen in the elderly known as vascular aging. The venous valves in legs, also interacting with blood flow to open and close as a result of FSI, facilitate the ability of the cardiovascular system to carry the blood back to the heart. Four different sets of heart valves, which turn on and off properly at each cardiac beat, are essential in regulating the unidirectional flow in the blood circulation system. The interaction between the blood and artery aneurysm can be investigated to understand the aneurysm rupture mechanism. The airflow within the lung alveoli is also important in understanding transport of particles and designing aerosol drug delivery systems. The study on obstructive sleep apnea (OSA) represents another example of FSI between airflow and the structures in upper airway (i.e., the soft palate and tongue). The studies of the above-mentioned biomedical FSI problems are of great significance in enhancing the understanding of the physiological performance, facilitating the clinical diagnosis and treatment, and improving the optimal design of bio-prostheses.

These FSI problems typically involve sophisticated mechanics, and they are in general still computationally very challenging in several aspects. First, each problem involves a complicated three-dimensional anatomical geometry for the fluid flow that varies from patient to patient. The movement due to deformation of the soft tissue further complicates the dynamics of the flow. Sec-

ond, the soft tissue in each problem generally consists of inhomogeneous and anisotropic materials that may go through large deformations. Therefore, the nonlinear tissue mechanics is not straightforward to model either with high accuracy in most cases. Lastly, FSI modeling of these soft tissues would require solving fluid mechanics and tissue mechanics simultaneously. A numerical method coupling both parts is often subject to limitation in mesh resolution, time step restriction, and numerical stability issues. Therefore, developing efficient computational methods for these FSI problems is still an active area of research.

In this dissertation, I will focus on two specific FSI problems: 1) the aortic valve, and 2) the vocal fold vibration. Both problems have strong applications in health care of patients, for which we aim to develop patient-specific computationally based tools for disease treatment, especially surgical planning. In the following sections, I will described medical background of each problem and discuss the state-of-the-art of computational modeling to provide a context for my study.

1.1 Fluid–structure interaction of heart valves and its computational modeling

1.1.1 Fluid–structure interaction of heart valves and applications

The human heart has four different sets of valves, one for each chamber of the heart. They are mitral valve, aortic valve, tricuspid valve, and pulmonary valve. The heart valves are thin, membrane-like structures, and they open and close mostly passively in response to the hemodynamic forces at each heart beat, regulating the unidirectional blood flow through the heart [3]. Specifically, during the systole, the left ventricle contracts and the aortic valve opens to allow the oxygen-rich blood being pumped through the aorta. Meanwhile, the pulmonary valve opens to allow the oxygen-poor blood in right ventricle go through the pulmonary artery to the lung. During the diastole, the pulmonary and aortic valves close while the tricuspid valve and mitral valve open, such that the blood fills inside the left and right ventricles, respectively.

According to the World Health Organization (WHO), the cardiovascular disease has been identified as the number 1 cause for death globally. Early detection and appropriate management using counselling and medicine are needed for people with cardiovascular disease or who are at high cardiovascular risk (due to the presence of one or more risk factors such as hypertension, diabetes, hyperlipidaemia or already established disease). Two common vascular diseases within the heart valve community are the aortic stenosis (AS) and the aortic regurgitation (AR). The AS occurs when the aortic valve becomes calcified and thickened (usually due to aging). The opening of the valve is narrowed and thus reduces or blocks the blood flow from the heart to the rest of the body. The AR happens when the valve fails to close tightly and the blood flows back due to the valve leakage. More than 85,000 valve substitutes are now implanted in the United states and 280,000 worldwide each year [4, 5].

Aside from *in-vivo* and *in-vitro* studies from the experimental side, the development of efficient and reliable computational FSI simulation tools in heart valve application provides an alternative way for the study of its performing mechanism. Many FSI simulations have been conducted in order

to promote the understanding of the fundamental physics of heart valves (both natural valves and prosthetic valves). Earlier FSI studies mainly focus on the construction of robust FSI simulation tool, with some discussion on the valve deformation, flow field and vortex structure [6–11]. With the advancement in computation power and medical imaging technique, recent studies are able to incorporate more realistic computational models into the FSI simulation, such as subject-specific aorta geometry, nonlinear and anisotropic valve material properties and physiological pressure loading [12–17]. Patient-specific FSI simulation can provide unique insights into the disease states and help the physicians to evaluate the valve/device and select the one that best fits the individual patient in transcatheter aortic valve implantation (TAVI) [18].

1.1.2 Literature review for computational modeling of heart valves

Due to substantial simulation challenges involved in handling the large three-dimensional (3D) geometrical variations, topological change of the flow domain (i.e., on and off of the valves), and numerical instability of the FSI algorithm, to date few methods can solve this FSI problem to a satisfactory level. It remains an active area of research to develop computationally efficient and yet high-fidelity simulation tools to model the FSI of heart valves.

Given the complex 3D geometry of heart valves and large displacement of the valve leaflets in a cardiac cycle, it is extremely difficult to apply a conventional computational fluid dynamics (CFD) method that is based on boundary-conformal meshing of the fluid domain, as frequent mesh regeneration would be needed to avoid severe mesh distortion and deterioration. Therefore, the existing numerical methods for the heart valve FSI have mostly relied on non-boundary-conformal or immersed-boundary type of approaches to solve the fluid flow. In these methods, the mesh discretizing the flow domain is a typically fixed grid, either structured (e.g., Cartesian) or unstructured, and is independent from the Lagrangian mesh that discretizes and tracks the solid domain representing the elastic leaflets. As the Lagrangian mesh moves across the fixed grid, special treatment needs to be done in the flow solver to accounts for the presence of the immersed leaflets and the effects of their movement.

To do so, De Hart et al. [19] introduced a Lagrange multiplier into the governing Navier−−Stokes equation to replace the surface force at the boundary for simulation of the aortic valve. Even though the flow simulation was limited to a coarse resolution of less than 1000 finite elements, this work nevertheless represents one of the early studies of full 3D FSI models of the heart valves. Later Griffith and coworkers [20, 10] advanced the aortic valve model by using a diffuse-interface immersed-boundary method that is based on the Cartesian grid for the flow. The use of a structured grid, and thus the efficient algorithms associated with the grid, allows the method to deploy much more mesh points to resolve the flow. In the diffuse-interface immersed-boundary method, the no-slip/no-penetration boundary conditions are not directly imposed when solving the Navier−Stokes equation; rather, in one computational step, the solid structure is first allowed to convect along with the fluid, and then the required stress from the fluid leading to the structural deformation is

computed by solving the solid mechanics; this fluid force is then fed into the momentum equation of the fluid as a regularized volumetric force to advance the time step. Conceptually, this approach only changes the sequence of the solution process and would still provide the same solution once convergence is reached. However, such sequencing could be prone to spurious fluid forces and numerical instability, especially when the stiffness of the structure is high and the computed fluid stress is sensitive to the structural deformation. In those simulations, the valve leaflets have low bending stiffness and thus may develop wrinkly deformations.

Borazjani [11] used a sharp-interface immersed-boundary method to model the flow for both a mechanical and a bio-prosthetic aortic valve. The method in this work was also based on a fixed but curvilinear grid, and fine resolution was applied to capture the detailed vortex structures in the flow. However, the structural model in the work utilizes membrane finite elements, which do not include the bending stress in the structure; thus, the leaflets also develop wrinkly deformations. Later, this method was extended to include shell elements to handle bending of the leaflets [21, 22]. The closing phase was not considered in those studies. Recently, Hsu and coworkers [3, 23] used a so-called immersogeometric FSI method to model both the flow and structure. Several advancements have been made in their study. For example, the mesh for the flow is not boundary-fitted but is adaptive around the solid surface; both stretching (in-plane) and bending (out-of-plane) deformation were included; a contact model was introduced for leaflet collision; and wall compliance was also incorporated. One limitation is that their study has not yet examined the flow field in detail. More recently, Mao et al. [24] combined a commercial finite-element package with a custom flow solver based on the smoothed particle hydrodynamics to simulate FSI of the aortic valve. With the help of the commercial package, their structural model is detailed and displays realistic pattern of deformation. However, their discussion on the flow field is also very limited.

To summarize this brief literature review, the FSI model of the heart valves has been advanced significantly in recent years, but there is still lack of modeling study that provides reasonable details for both the valve deformation and the flow pattern. To address this issue, we propose a 3D FSI simulation of the aortic valve to investigate both the leaflet deformation and vortex pattern in the flow. Studies like this are significant because it is understandable that for systems like the heart valves, the flow pattern is intricately associated with the structural deformation through the interaction, and understanding the relationship between these two parts may lead to useful tools to diagnose any abnormality of one part based on available information about the other. Thus, in my study I will consider both the flow and the structural mechanics in detail.

1.2 Fluid–structure interaction of vocal fold and its applications

1.2.1 Vocal fold vibration and voice production

Phonation is one critical component of many human activities, such as singing, communication, and expression of emotion. The phonation process is represented by a rapid and periodic opening and closing of glottis through the separation and apposition of a pair of valve-like structure of muscle

and tissue called vocal fold with the accompany of airflow under lung pressure [25]. During this process, the air is expelled from the lung through the glottis and the self-oscillating motion of the vocal fold is sustained, generating fundamental frequency between 80 and 220 Hz for normal voiced speech [26]. As reported in a statistical study [27], approximately 7.5 million people in the United States have a type of voice disorder, which can lead to discomfort, pain, poor work performance, social withdrawal, and even long-term disability.

The key objective of constructing a high-fidelity computational modeling tool is to investigate the behaviour of the intraglottal air flow, the vibrating vocal fold dynamics as well as the coupling between these two. Meanwhile, such modeling tools should be able to account for the complex geometry of musculo-cartilaginous structure, the multi-layer structure of vocal fold, and the accurate parameterization of tissue property of the vocal fold [26]. Being an alternative way to experimental study, the computational modeling is of important use to enhance the understanding of the phonation process in the larynx, to assist the diagnosis and treatment of voice disorders in clinical situations, to provide new explanations to laryngeal pathology such as acute phonotrauma, to improve the design of prosthetic larynges, and to predict the performance of surgical implants.

1.2.2 Literature review for computational modelling of vocal fold

Many FSI models have been developed in the past with various levels of complexity to simulate the vocal fold vibration. In terms of spatial setup, these models can be generally categorized depending on whether the airflow and the tissue respectively assume a zero-, one-, two-, or three-dimensional configuration. Within each configuration, the models can still differ significantly from one another depending on how to treat various details such as the structural tissue layers, elastic properties of the tissue, and anatomical features of the larynx. In early stages, discrete or lumped-mass systems were created to understand onset of phonation [28–30]. In these models, the vocal fold was simplified to two or more mass blocks connected to elastic springs, and the Bernoulli equation or other simplified flow equations were used to model the airflow. Despite its simplicity, such models can capture self-induced oscillations and have been used extensively to understand basic effects of governing parameters, e.g., the subglottal pressure and tissue stiffness, and also to investigate characteristic behavior of normal and abnormal phonation, e.g., chaotic vibration and vocal fold polyps [29]. With the development of high-performance computing hardware and software, continuum-mechanics based computational models have been increasingly used for vocal fold modeling. For example, both two-dimensional (2D) and 3D finite-element models have been developed to simulate the vocal fold deformation [31–35]. More recently, high-resolution simulations have been more frequently used in the FSI modeling of the vocal fold. Examples of previous works include[36–39]. Using the intensive, typically parallelized computations, many of these studies have reported the unsteady vortex structures in the airflow and their interaction with the vocal fold.

As modern medical imaging technology is being advanced, internal anatomy of human bodies can be viewed with unprecedented details using noninvasive approaches such as computed tomog-

raphy (CT) and magnetic resonance imaging (MRI). Such imaging modalities may provide 3D geometry of the larynx as well as the interior structure of the tissues [40, 41, 2]. The images generated by these techniques could be used to develop more sophisticated computational models that have much realistic representation of the laryngeal anatomy. Compared with the previous computational models that are based on greatly simplified geometries (even for continuum-based models), the anatomical models are a significant step closer to patient-specific and high-fidelity modeling of phonation, which is eventually needed for clinical care of voices of individual patients. Some recently work, e.g., [42] and [43], provide insights into the development towards such medical imaging based models of the vocal fold. More details about the development and improvement of vocal fold modeling can be found in review papers of [44] and [26]. Only a brief summary of literature is provided here to set up the context for the present study.

One issue related to patient-specific modeling is that even if a patient's anatomy could be reconstructed with high fidelity, there are still a few other modeling parameters whose values cannot be specified with accuracy, for example, the elastic properties of the tissue material that may vary from patient to patient. Even for the same patient, the effective stiffness of the tissue highly depends on neurological control of various muscle groups and consequently the adduction state of the vocal fold [45]. These uncertain parameters are important to capture the patient-specific vibration features [46]. Therefore, either ad hoc assumptions have to be made, or some parameter identification approach must be used to estimate those parameters. It will be too expensive to perform parameter identification using 3D FSI models due to their high computational cost. One possible method is thus to use a reduced-order model to determine those unknown material properties, which could then be used to enhance fidelity of the 3D models.

To construct a reduced-order FSI model for vocal fold vibration, it may be appropriate to simplify the description of the flow rather than the description of the tissue mechanics, especially when accurate capture of the vibration characteristics is desirable. This is because the vocal fold deformation is three-dimensional and can be complicated, requiring at least a 3D model representation; furthermore, 3D simulation of the turbulent glottal flow is typically much more expensive than 3D simulation of the tissue deformation, and reducing flow simulation can largely lower the overall computational cost. For such a purpose, the Bernoulli equation has been most widely used in the past to describe the pressure and velocity of the glottal flow. A comparison of the Bernoulli equation with the Navier−Stokes equation was studied by [47], who used a 2D setup, assuming either steady flow or FSI, to assess the accuracy of the Bernoulli principle. Their comparison showed that all Bernoulli based models result in similar predictions of the mean intraglottal pressure, maximum orifice area, and vibration frequency; however, those predictions rely on the heuristic specification of flow separation location in the Bernoulli models, and the location is quite different from that obtained from the simulation based on the Navier−Stokes equation.

In a previous work [48], the authors coupled an anatomical vocal fold model that was based on the MRI scan of the rabbit larynx with a Bernoulli based flow model to perform fast FSI simulations. Their flow model was calibrated a priori using 3D flow simulation of the same larynx,

in which the 3D flow data were used to set up the curved flow path along the airway for the 1D model and also to specify the proper location of flow separation. Using a hybrid FSI model of the 1D flow and the 3D tissue and trying to match the model prediction with the experimental measurement of the vibration, they estimated the elastic constants of the vocal fold of each subject. Next, with the material properties identified for individual samples, the updated 3D FSI simulations were able to capture the specific vibration characteristics for each subject used in the study. In a later study, the same authors compared the hybrid FSI model with 3D FSI by using a simplified vocal fold geometry to more thoroughly assess the performance of such Bernoulli based 1D flow models [48]. They found that that model prediction can be sensitive to the subjective specification of the separation location; in some case where the medial thickness of the vocal fold is small, the hybrid FSI model leads to a significantly different vibration mode of the vocal fold than the 3D FSI model. From these previous studies, it is clear that the Bernoulli equation has serious limitation in its capability to satisfactorily compute the pressure in the flow for a given geometrical configuration of the glottis, and a new model that can better predict the pressure is desirable.

Computational modelling of vocal fold can also find its application in the clinical treatment of unilateral vocal fold paralysis (UVFP). Based on a conservative estimation, more than 20,000 patients are diagnosed with UVFP annually in the United States [49]. Type I laryngoplasty is commonly used in surgical re-positioning of the paralyzed vocal fold and an implant is placed in the thyroid cartilage to medialize the affected vocal fold. The implant changes not only the shape of the glottis but also the dynamic response of the vocal folds to the airflow exiting through the glottis. Although patients benefit significantly from intervention, variability exists in approaches to surgical management due to the subject-specific differences in the laryngeal anatomy and tissue properties. This variability produces undesirable inconsistency in clinical outcomes, increases healthcare costs and an unnecessary burden on patients and their families.

In the context of voice production, the complex interaction among glottal airflow, vocal fold tissue, and implant design presents a perfect FSI problem for computational modeling to solve. A physics-based, high-fidelity and efficient computational tool that incorporates the individual-specific features of the laryngeal anatomy and tissue properties can be used to assist surgeons with pre-operative planning and to improve surgical outcomes.

1.3 Overview of the dissertation

In this dissertation, we will computationally study both the aortic valve and the vocal fold. These two topics are included in one dissertation because of two main reasons. First, we use essentially the same numerical method to solve the 3D fluid–structure interaction for both the aortic valve and the vocal fold. That is, a Cartesian grid based immersed-boundary method is utilized to solve the viscous incompressible flow (blood or air), and a nonlinear finite-element method is utilized to solve the deformation of the soft tissue (the leaflets or the vocal fold); furthermore, a partitioned, strong coupling approach is adopted to handle the FSI process.

Second, for both problems we have complemented the 3D simulation with a similar reduced-order approach to model the flow. In particular, a one-dimensional (1D) flow model is developed in each case to represent the transient flow with drastically reduced computational cost. Such a 1D model is coupled with the 3D FEM tissue model to simulate the FSI with the goal of reproducing the deformation and dynamics of the tissue as close as possible to the full 3D FSI model. In each case, we will describe the 1D flow model development, reduced-order FSI simulation, and its performance assessment.

The following sections summarize each chapter and their relationship.

1.3.1 Parallelization of an immersed-boundary method based on domain decomposition (Chapter 2)

In this chapter, we present a parallel algorithm of the immersed-boundary method based on the simple idea of multi-dimensional domain decomposition. The structured Cartesian grid is divided into multiple partition blocks, or subdomains, and each processor core will work on its assigned partition. Data exchange among the processor cores is done via MPI calls. Speedup and code efficiency are analyzed for several benchmark test cases; then the parallel code is applied to case studies for demonstration, including hummingbird flight, vocal fold, and aortic valve.

1.3.2 A computational study of the 3D FSI of aortic valve (Chapter 3)

In this chapter, a 3D computational study of the FSI of the aortic valve is presented, where the leaflet thickness is set to 0.1 mm. This represents our first exploration of using the in-house immersed-boundary method to model the heart valve and studying the underlying FSI from a perspective that has not been well discussed before. In particular, we present a balanced approach to model both flow and valve mechanics and use high resolution to resolve the transient flow field. Both the flow field and deformation of the aortic valve are discussed in detail. On the flow side, the pressure and velocity field, the transient flow rate, the momentum balance along the flow direction and the vortex development are analyzed. On the structure side, the geometric and effective opening areas, the deformation pattern, the transient hemodynamic force experienced by the valve, and the pressure loading on the leaflet surface are quantitatively examined.

1.3.3 Effect of bending stiffness on the FSI of aortic valve (Chapter 4)

After completing a baseline case study in Chapter 2, we move on to perform a parameter study using the same aortic valve model. In particular, the thickness of the valve leaflets is varied from 0.1 mm to 0.8 mm, and therefore the corresponding normalized bending stiffness (scaled by the driving pressure gradient along the aorta) varies in a wide range, representing both healthy and diseased aortic valves. Through the 3D simulation, we perform detailed analyses of the valve deformation and the transient flow field, including pressure distribution over the leaflets, flow rate,

vortex dynamics, as well as the overall force on the valve. An optimal bending stiffness of the leaflets is found through this study. Furthermore, we propose a new 1D flow model and perform the reduced-order FSI simulation using this model. Its successes and limitations are studied in juxtaposition with the 3D FSI simulation.

1.3.4 A reduced-order flow model for fluid–structure interaction simulation of vocal fold vibration (Chapter 5)

In this chapter, we first consider an idealized vocal fold geometry and use the 3D FSI approach to simulate the vocal fold vibration. Based on insight from the 3D simulation, we developed a reduced-order flow model for the glottal airflow. Unlike the previous reduced-order flow models, the present 1D flow model is based on the viscous momentum equation, as opposed to the Bernoulli principle for ideal flow. In addition, an "entrance effect" is introduced to account for flow focusing at the glottal entrance. The performance of this model in FSI simulation is evaluated using full 3D FSI as the benchmark.

1.3.5 A reduced-order flow model for vocal fold vibration: from idealized to subject-specific models (Chapter 6)

In this chapter, we extend the reduced-order flow model developed for an idealized vocal fold model in the preceding chapter to subject-specific vocal fold models. The material properties of the vocal fold tissue used here are based on parameter estimation in our previous study. The numerical results are compared with those from the high-speed imaging experiment of *in vivo* phonation. Good agreement is found in the vibration frequency, amplitude, phase delay, and deformation pattern of the vocal fold, which suggests potential application of the present approach for future patient-specific modeling.

Chapter II

Parallelization of an immersed-boundary method based on domain decomposition

2.1 Introduction

Immersed-boundary method was originally proposed by Peskin in the numerical analysis of blood flow in the heart [50, 51]. Unlike the traditional methods that are based on body-conformal mesh, one key feature of the immersed-boundary method is the usage of a Cartesian background mesh for discretization of the flow domain, which greatly simplifies the preprocessing step of mesh generation. The immersed solid body, usually represented by a Lagrangian mesh, moves through the Cartesian flow mesh, and its effect on the flow can be modeled by constructing the forcing term at the fluid–structure interface [52]. The immersed-boundary method has been proven suitable for solving moving boundary problems with complex geometry and large deformation [53], which are often encountered in biological flows since complex anatomies and soft tissues are typically involved in biological systems. Moreover, the concern for numerical stability associated with mesh regeneration in traditional body-conformal methods is relieved by using the immersed-boundary method. Thanks to these advantages, the immersed-boundary method has been gaining more popularity recently for modeling biofluid dynamics. Since its original employment, many modifications and improvements have been made, and similar methods have found wide applications such as cardiovascular flows [6, 10, 14, 1, 54] and biological locomotion problems [53, 55].

Three-dimensional flow simulations are usually time-consuming, especially when a fine mesh needs to be used and large deformation of flow domain is involved. In typical cases, parallel computing is indispensable in flow simulations. Different parallelization approaches have been devised specifically for the immersed-boundary method. Givelberg and Yelick proposed a parallel framework for their immersed-boundary method software package called IB using the object-oriented Titanium language [56]. In their framework, fluid nodes on the mesh are assigned to different processor cores for calculation of the fluid force and update of the boundary position. The scalability of their approach was carried out with up to 16 million mesh points and 128 processor cores. Yildirim et al. presented a parallel scheme to solve FSI problems, and the parallel efficiencies for the immersed-boundary method and the body-conformal method are compared on up to 1024 processor cores using a mesh size of 5 million points [57]. Wiens and Stockie put forward a domain decomposition parallelization for an immersed-boundary algorithm, and the speedup and efficiency

were tested with no more than 256 processor cores [58]. Spandan et al. presented a domain decomposition framework for simulating the flow in the left ventricle of the heart, in which strong scaling was achieved up to 1000 cores [59]. Parallel techniques for the immersed-boundary method were also specifically used to accelerate the FSI simulation of heart valves [10, 11, 23, 1].

In this work, a parallel algorithm for our flow solver, which is based on a direct-forcing immersed-boundary method, is implemented for the FSI study of soft tissues. This parallel algorithm takes advantage of the structured mesh. The entire flow domain can be divided into multiple subdomains with the flexibility of either 1D, 2D, or 3D decomposition. All the processor cores are indexed to facilitate data exchange between neighboring cores through the MPI protocols. We first test this parallel algorithm by using two benchmark cases, Taylor–Green vortex and Hills spherical vortex, where the analytical expressions exist at least for initial flow specification. The parallel performance will be analyzed using different mesh sizes. Then, we apply this parallel algorithm to three biological flow problems: the unsteady aerodynamics of hummingbird during fast forward flight, the vocal fold vibration, and the aortic valve functioning.

2.2 Parallel algorithm for the immersed-boundary method

In a previous work from our group [53], an in-house FORTRAN code has been developed for the simulation of 3D fluid–structure interaction (FSI) problems in biological systems involving large deformation. This method uses a partitioned framework with strong FSI coupling. The viscous incompressible Navier−Stokes equation is solved with a sharp-interface immersed-boundary method based on Cartesian grid. A hybrid formulation was implemented in this method to reduce the numerical oscillations for moving boundaries [60]. The large deformation involved in solid-body dynamics is solved with a conventional finite-element method accounting for both geometric and material nonlinearity. The entire FSI system is solved in a block-wise iterative manner until the convergence criterion is achieved at the fluid–structure interface. This numerical approach has been validated through several benchmark test cases and its versatility has been presented through its applications in several FSI studies by our group, such as the hovering and forward flight of the hummingbird [61, 55], vocal fold vibration [45, 62], and the heart valve [1].

In a partitioned FSI framework, data exchange is necessary at the fluid–structure interface between the flow solver and the structure solver. To be more specific, the force is interpolated on the flow side from the instantaneous flow field and is then sent to the structure solver. The displacement and velocity of the fluid–structure interface are computed by the solid solver and sent to the flow solver to be used as internal boundary condition for the flow. Thus, the overall computation time of the FSI simulation depends on both the flow solver and the solid solver. Comparable time spending between the flow solver and the solid solver can effectively reduce the waiting time between these two solvers and thus accelerate the FSI simulation. However, the FSI simulation often becomes very time-consuming, especially when fine mesh is employed on the flow side in order to capture accurately the flow characteristics and calculate the stresses on the structure. In this situation, implementation of parallel computing becomes necessary for flow simulations.

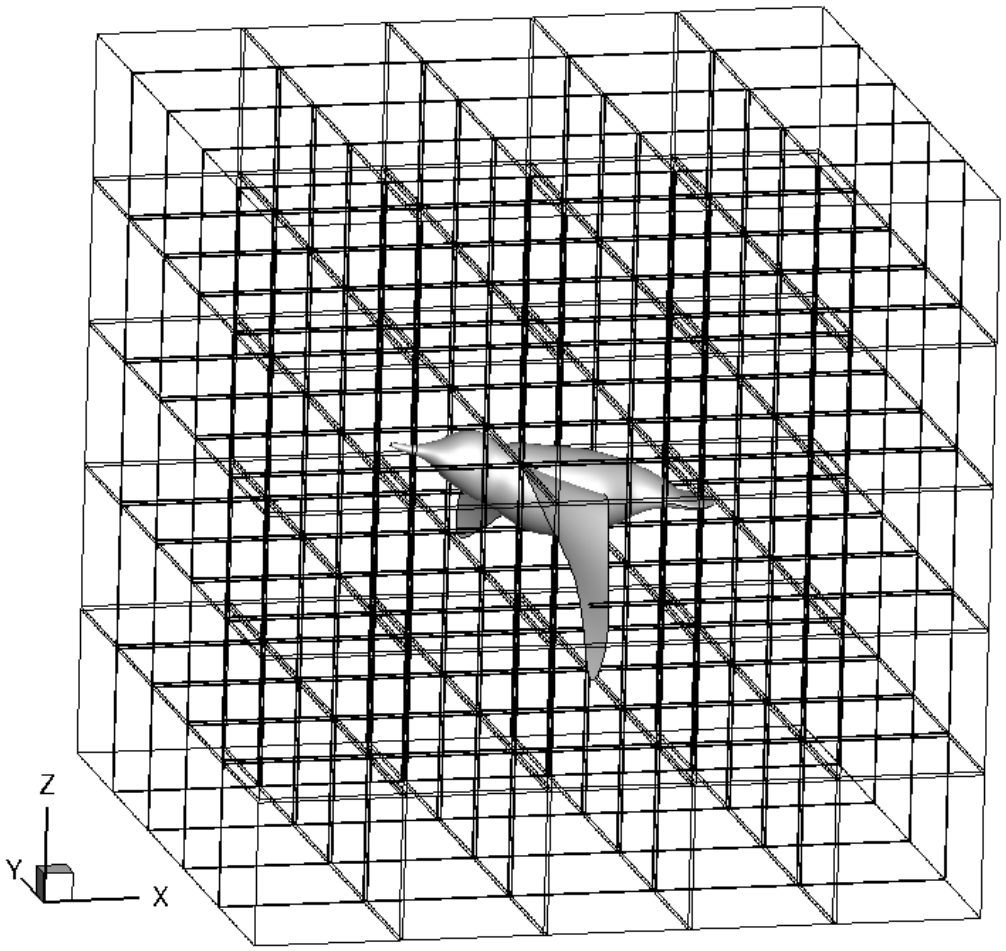

Figure 2.1: Illustration of 3D domain decomposition for a hummingbird simulation.

In one of our FSI studies of the aortic valve [1] (also Chapter III), we have successfully implemented a simple MPI parallelization approach for the flow based on one-dimensional domain decomposition. The rectangular computational domain, which is discretized by a single-block Cartesian grid, is divided into multiple subdomains along one spatial direction, and each processor core is assigned to handle one subdomain only. At each overlapping boundary of a subdomain, two buffer slices are used to store the flow data exchanged from the neighboring processor core. The setup of the buffer slices and the storage of the flow data are necessary to support the correct interpolation, extrapolation, or the finite-difference discretization at the grid points within the subdomain. The structure solver is parallelized with an OpenMP strategy since the mesh size for the solid body is much smaller than that on the flow side in the applications we consider.

In order to further accelerate the costly flow simulation, it is desirable to split the computational domain in the other two spatial directions as well, which would result in two- and three-dimensional domain decomposition approaches. By doing so, much more processor cores can be deployed for the flow simulation and for each core, the subdomain and the corresponding computational load would be further reduced. In this work, we implement both 2D and 3D domain decomposition and test the parallelization performance for these strategies.

Details of the current immersed-boundary method for solving the flow have been described previously [63, 60]. A brief description of the 1D domain decomposition has also been introduced in the application to the FSI of the aortic valve [1] (also Chapter III). In order to facilitate the understanding of the strategies here, we demonstrate the 2D domain decomposition as an example. In the current sharp-interface direct-forcing immersed-boundary method, the Cartesian grid points are divided into four categories: fluid nodes, solid nodes, ghost nodes, and hybrid nodes. The fluid nodes occupy the flow region and anchor the standard second-order finite-difference stencil used in the discretized equation, while the solid nodes in the interior of the solid body are simply dummy nodes. The ghost nodes and hybrid nodes are defined in the vicinity of the fluid–structure interface. Calculation on the ghost nodes requires the local extrapolation of the flow field into the solid domain. For each hybrid node, both a local flow field interpolation and finite-difference discretization of the momentum equation are used to improve the solution near the interface when a moving boundary is involved. For both ghost and hybrid nodes, the numerical treatment involves a few nearby nodes and also the boundary conditions at the fluid–structure interface to support the interpolation, extrapolation, or finite-difference discretization.

The extension of domain decomposition from 1D to 2D and 3D is straightforward conceptually. In the 1D domain decomposition, the entire computational domain is divided into several slabs along one direction. Each processor core only works on its own assigned partition that is indexed using a one-dimensional array. For each subdomain, two extra buffer slices are included on each of the two ends to store the necessary flow data obtained from the neighbouring subdomain. For instance, for the k-th core in 1D domain decomposition, the flow data on the buffer slices are directly from the $(k-1)$-th core on the left side and from the $(k+1)$-th core on the right side. For 2D domain decomposition, the entire computational domain is further divided in the second

spatial direction, resulting in long cubes of subdomains. Indexing of each subdomain and processor core now requires two-dimensional arrays. The size of the subdomains is reduced thanks to the added decomposition in the second direction, while the number of communication calls increases as the number of neighboring subdomain becomes more. For example, for the (j,k)-th core, it needs to receive the flow data from $(j-1,k)$-th, $(j+1,k)$-th, $(j,k-1)$-th, and $(j,k+1)$-th cores on its left, right, top, and bottom sides, respectively. Note that the size of the flow data for the communication at each overlapping subdomain-subdomain interface reduces as more subdomains are created, which helps reduce the communication load even though the number of communication calls increases.

Within each subdomain, identification of all four types of nodes on the Cartesian mesh and also setup of the interpolation and extrapolation stencils associated with the ghost/hybrid nodes are carried out by its assigned processor core only. Doing so helps increase scalability of the entire simulation time step. Note that some ghost nodes and hybrid nodes could be located near the subdomain boundary, and the flow data at the two extra buffer slices will be used for those nodes to support the correct computation of interpolation and extrapolation.

Since the current FSI simulation employs a partitioned framework, parallelization of the structure solver can be done independently from that of the flow solver. Furthermore, the flow solver and structure solver can run in parallel and necessary data exchange is coordinated through MPI. The number of the OpenMP threads to parallelize the structure solver is set to provide a balanced cost between these two solvers.

At each time step, the current configuration of the solid body is updated from the structure solver, and the identification of the fluid nodes, solid nodes, ghost nodes, and hybrid nodes is carried out by the flow solver. Then, the interpolation and extrapolation stencils for the ghost nodes and hybrid nodes are prepared. The solution procedure for one flow step consists of three substeps and can be summarized as follows. In the first substep, an advection-diffusion equation is solved in the absence of the pressure, and an intermediate velocity field is obtained. In this step, both the nonlinear advection term and the viscous term are discretized using the Crank–Nicolson scheme to improve the numerical stability, and the spatial derivatives are discretized by a second-order central scheme. Gauss–Siedel line relaxation method is used to solve the linearized system. In the second substep, the Poisson equation is solved to obtain the pressure field, and in the third substep, the velocity is updated using the pressure to become divergence-free.

In order to accelerate the convergence of the Poisson equation in the second substep, which is the most expensive part in the flow simulation, we have implemented a parallel multigrid method in the solver. A V-cycle iteration strategy is adopted in the multigrid implementation. In the V-cycle, the residual of the Possion equation is first computed from a nested Gauss–Siedel relaxation method at a finer grid level and is then interpolated to the next coarser grid through the injection step. The same process is repeated until the coarsest grid level is reached. Then, the solution from the coarser level is interpolated onto the next finer level to correct the pressure at that level.

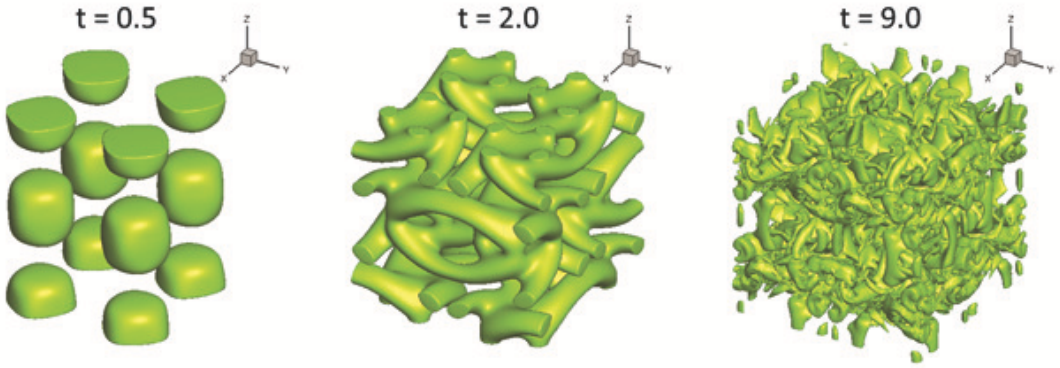

Figure 2.2: Decay of the Taylor–Green vortex at Re=1600.

All of our tests are done on Stampede 2 at the Texas Advanced Computing Center (TACC).

2.3 Performance tests

2.3.1 Taylor–Green vortex

The Taylor–Green vortex represents decaying of an isotropic, homogeneous turbulence in an unbounded domain and is often used for the purpose of code validation or numerical approach evaluation [64, 65]. The flow is computed by directly solving the Navier−Stokes equation in the primitive variables. The flow domain is a cubic bounding box with a length of $2\pi L$ and is discretized by a uniform Cartesian grid. Within the domain, the flow variables, velocity (u, v, w) and pressure p, are initialized according to the following formula:

$$\begin{aligned} u &= V_0 \sin\left(\frac{x}{L}\right)\cos\left(\frac{y}{L}\right)\cos\left(\frac{z}{L}\right), \\ v &= -V_0 \sin\left(\frac{x}{L}\right)\cos\left(\frac{y}{L}\right)\cos\left(\frac{z}{L}\right), \\ w &= 0, \\ p &= p_0 + \frac{\rho {V_0}^2}{16}\left[\cos\left(\frac{2x}{L}\right)+\cos\left(\frac{2y}{L}\right)\right]\left[\cos\left(\frac{2z}{L}\right)+2\right], \end{aligned} \tag{2.1}$$

where $L = 1$ is the reference length, $V_0 = 1$ is the reference velocity, $p_0 = 0$ is the reference pressure, ρ is the density. The Reynolds number, $Re = \rho V_0 L/\mu$, is set to 1600, where μ is the viscosity.

Fig. 2.2 presents the contours of the vorticity at $t = 0.5$, $t = 2.0$ and $t = 9.0$. The flow field transforms from the initial solution specified by the analytical expression Eq. (2.2), which contains one single length scale, to rapid build-up of a fully turbulent dissipative spectrum due to the nonlinear interaction of the developing eddies. The smaller eddies will eventually die out if the simulation continues.

Fig. 2.3 shows the transient evolution history of the kinetic energy E_k within the flow domain computed using a total number of 64 processor cores and 2D domain decomposition with 8×8

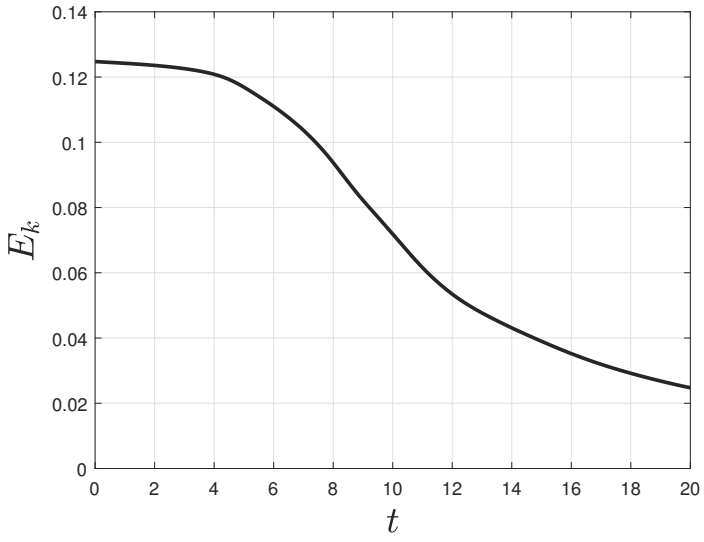

Figure 2.3: Evolution of the kinetic energy in the Taylor–Green vortex.

in the y- and z-directions. The kinetic energy is defined by $E_k = \frac{1}{\rho\Omega}\int_\Omega \frac{\rho u_i u_i}{2}\, d\Omega$, where Ω is the flow domain. The evolution curve starts at about 0.125 and gradually reduces to about 0.025 when $t = 20.0$. This result is in good agreement with Debonis [64].

In order to test the parallel performance of our domain-decomposition strategy, four different grid sizes are used, namely, 256^3, 512^3, 1024^3, and 2048^3. The wall-clock times, measured in seconds, are listed in Table 2.1. In Fig. 2.4, we plot the speedup and parallel efficiency for different grid sizes. From these results, we can see that scaling performance is significantly affected by the mesh size. For the smallest mesh, 256^3, the scaling performance drops below 60% for more than 256 cores; for the 512^3 mesh, the scaling performance is below 60% for more than 1000 cores. Clearly, the speedup and parallel efficiency are improved as the grid size increases. For both 1024^3 and 2048^3 meshes, even super-linear performance is observed for intermediate number of cores. For instance, the parallel efficiency with 64 cores for the 1024^3 and 2048^3 meshes is 103.4% and 108.5%, respectively. For the 2048^3 mesh, the code scales very well for even 4000 cores.

2.3.2 Hill's spherical vortex

Hill's spherical vortex represents the steady flow of a spherical vortex in a rotating fluid. Such a vortex can be produced inside an air bubble immersed in a uniform passing flow. The velocity

(a)

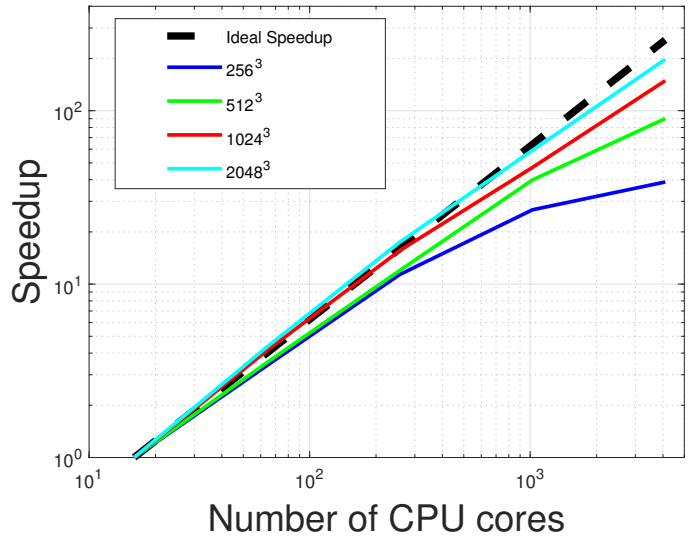

(b)

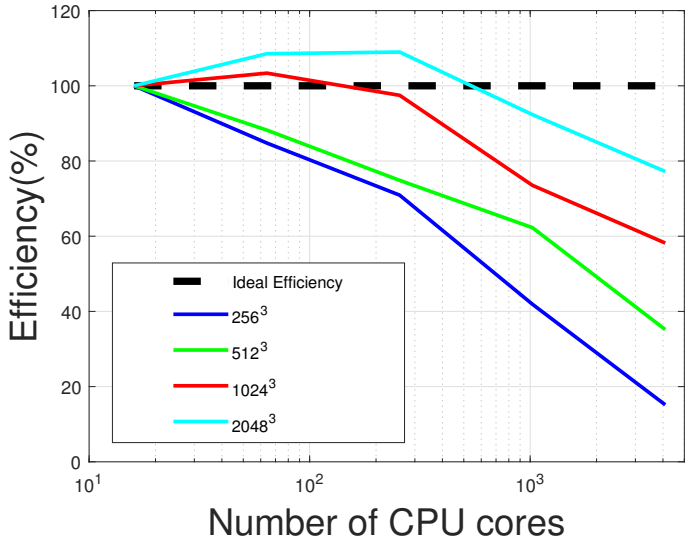

Figure 2.4: Speedup and parallel efficiency for the Taylor–Green Vortex with different mesh sizes.

y	z	Total	256^3	512^3	1024^3	2048^3
1	1	1	433.7	3626.7	–	–
2	2	4	117.9	985.6	7620.4	–
4	4	16	29.5	243.1	2159.9	20339.2
8	8	64	8.7	68.9	522.4	4685.2
16	16	256	2.6	20.3	138.5	1166.5
32	32	1024	1.1	6.1	45.9	344.2
64	64	4096	0.42	2.7	14.5	102.9

Table 2.1: The wall-clock time measured in seconds with various domain decomposition for the Taylor–Green vortex.

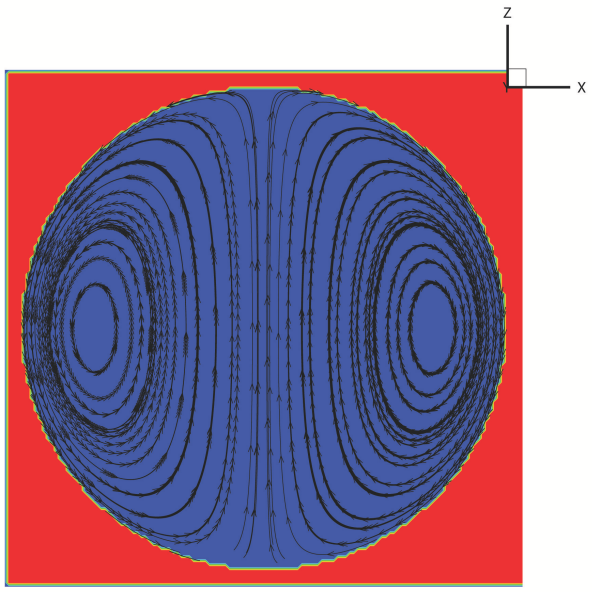

Figure 2.5: Flow pattern in Hill's spherical vortex.

y	z	Total	256^3	512^3	1024^3	2048^3
1	1	1	377.1	2935.9	–	–
2	2	4	99.3	771.1	6668.6	–
4	4	16	30.8	244.6	2097.9	23651.4
8	8	64	9.3	69.7	569.6	4859.1
16	16	256	2.5	20.0	160.5	1287.6
32	32	1024	1.0	7.8	41.7	356.9
64	64	4096	0.72	2.7	14.3	104.1

Table 2.2: The wall time measured in seconds for various domain decomposition and grid sizes in Hill's spherical vortex.

components within the sphere are described as

$$\begin{aligned} u &= V_0 \frac{xz}{R^2} \\ v &= V_0 \frac{yz}{R^2} \\ w &= V_0 \left[1 - \left(\frac{z}{R}\right)^2 - 2\left(\frac{r}{R}\right)^2 \right] \end{aligned} \tag{2.2}$$

where R is the radius of the sphere, $r = \sqrt{x^2 + y^2}$, and V_0 is the reference velocity. Fig. 2.5 shows the flow pattern within the sphere from our simulation using 64 cores and 2D decomposition (8×8 in the y- and z-directions).

Compared with the preceding case of the Taylor–Green vortex where there is no solid body present, the Hill's vortex contains the immersed-boundary treatment. We purposely set the sphere as the fluid-solid interface and specify the velocity at the spherical surface. Therefore, the immersed-boundary algorithm is activated in the code, including identification of the fluid and solid regions, setting up stencils for the ghost and hybrid nodes near the interface, and calculation of solutions at these nodes. The numerical tests would serve the purpose of evaluating scaling performance when the immersed-boundary treatment is active in the simulation.

To test the parallel performance, four different grid sizes are used, 256^3, 512^3, 1024^3, and 2048^3. The wall-clock times, measured in seconds, are listed in Table 2.2. In Fig. 2.6, we plot the speedup and parallel efficiency for different grid sizes. From these results, we can see that scaling performance is again significantly affected by the mesh size. For the smallest mesh, 256^3, the scaling performance drops below 70% for more than 256 cores; for the 512^3 mesh, the scaling performance is similar. The speedup and parallel efficiency are improved as the grid size increases further. For the 1024^3 mesh, the efficiency is near 60% for 4096 cores; for the 2048^3 mesh, the efficiency displays super-linear performance for up to 1000 cores, and it is still around 80% for 4096 cores. These results indicate that the current immersed-boundary solver can scale up to 4096 cores when handing large-size problems of more than one billion mesh points.

(a)

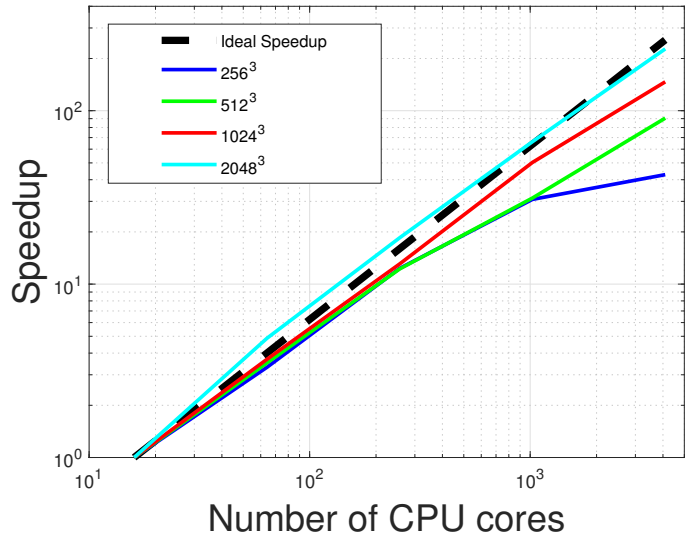

(b)

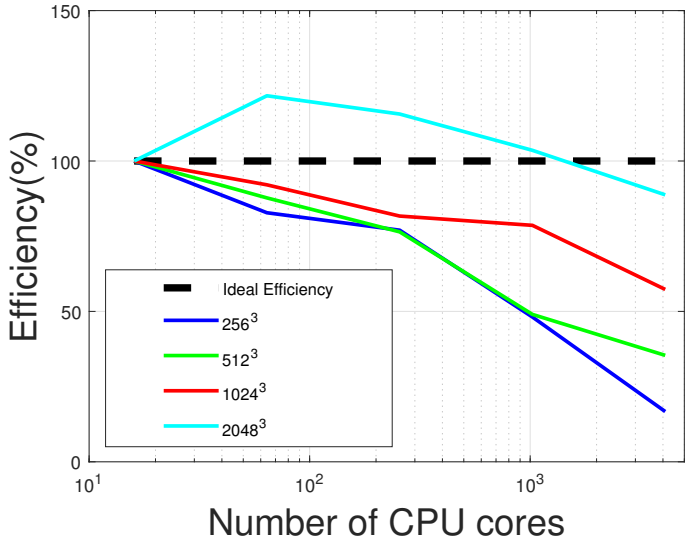

Figure 2.6: Speedup and parallel efficiency for different grid sizes in Hill's spherical vortex.

y	z	Total	Wall time	Speedup	Efficiency
5	5	25	333.7	1.00	100.0%
10	5	50	164.3	2.03	101.6%
10	10	100	94.0	3.55	88.8%
20	10	200	49.1	6.80	85.0%
25	10	250	40.1	8.32	83.2%
25	20	500	21.5	15.52	77.6%
25	40	1000	11.4	29.27	73.2%
25	80	2000	6.8	49.07	61.3%
50	80	4000	4.9	68.10	42.6%

Table 2.3: The wall time measured in seconds and parallel performance on a $600 \times 500 \times 400$ mesh for hummingbird flight.

2.3.3 Case demo 1: hummingbird flight

We further test the scaling performance of our flow solver through a computational study of the flapping-wing aerodynamics of the hummingbird. The background of the problem and hummingbird model setup are described in detail in Song *et al.* [55]. Briefly, the wing kinematics of a calliope hummingbird was obtained a high-speed filming of the bird in wind tunnel and was reconstructed for flow simulation. The bird's wing span is around 10 cm. Its flight speed is 8.3 m/s, and the wingbeat frequency is 45.5 Hz. The computational domain is represented by a $24 \times 20 \times 16$ cm^3 rectangular box. We tested the code performance by using different domain decomposition on a Cartesian mesh of $600 \times 500 \times 400$ (120 million) points. The results are listed in Table 2.3, and Fig. 2.7 presents the corresponding speedup and parallel efficiency. In this simulation, the subdomains have the same size, but the computational load among the processor cores are not well balanced since some of the subdomains contain part of the hummingbird body and some do not. Nevertheless, the flow code scales well up to 2000 CPU cores with a speedup around 49 (with respect to 25 cores) and a parallel efficiency near 61%. If the number of cores is further increased to 4000, the speedup increases to about 68 (with respect to 25 cores); however, the efficiency drops to around 43%.

Figure 2.8 shows the vortex structures around the hummingbird within one wingbeat cycle from a complete simulation. This simulation uses a stretched Cartesian grid of $680 \times 600 \times 480$ (about 196 million) points. Around the hummingbird, the grid resolution is 0.025 cm in all three directions. The Reynolds number based on the flight speed and the average wing chord length is around 3000. The time step is $\Delta t = 0.005$ ms, which leads to approximately 4400 steps per wingbeat cycle. For domain decomposition, 50 and 40 cores are used in y- and z-directions, respectively, which leads to a total number of 2000 cores.

(a)

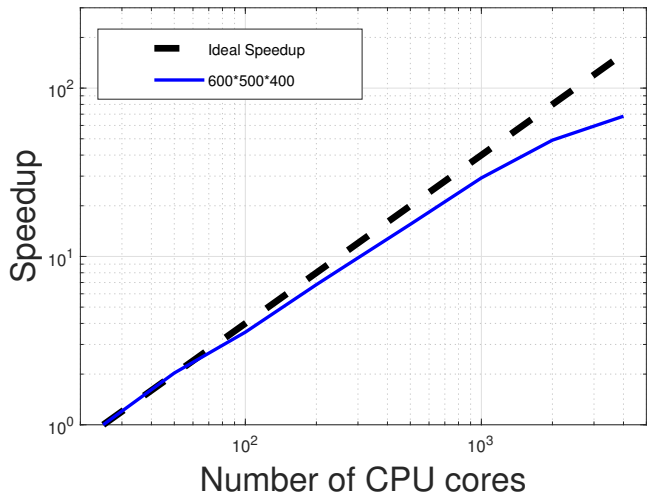

(b)

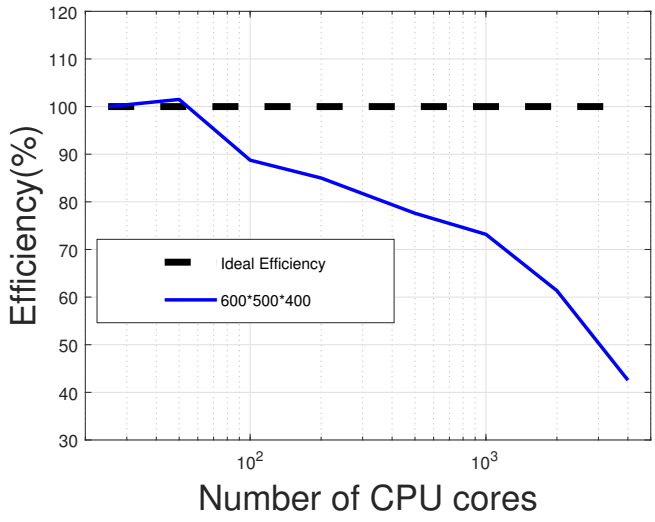

Figure 2.7: Speedup and parallel efficiency in the simulation of hummingbird flight.

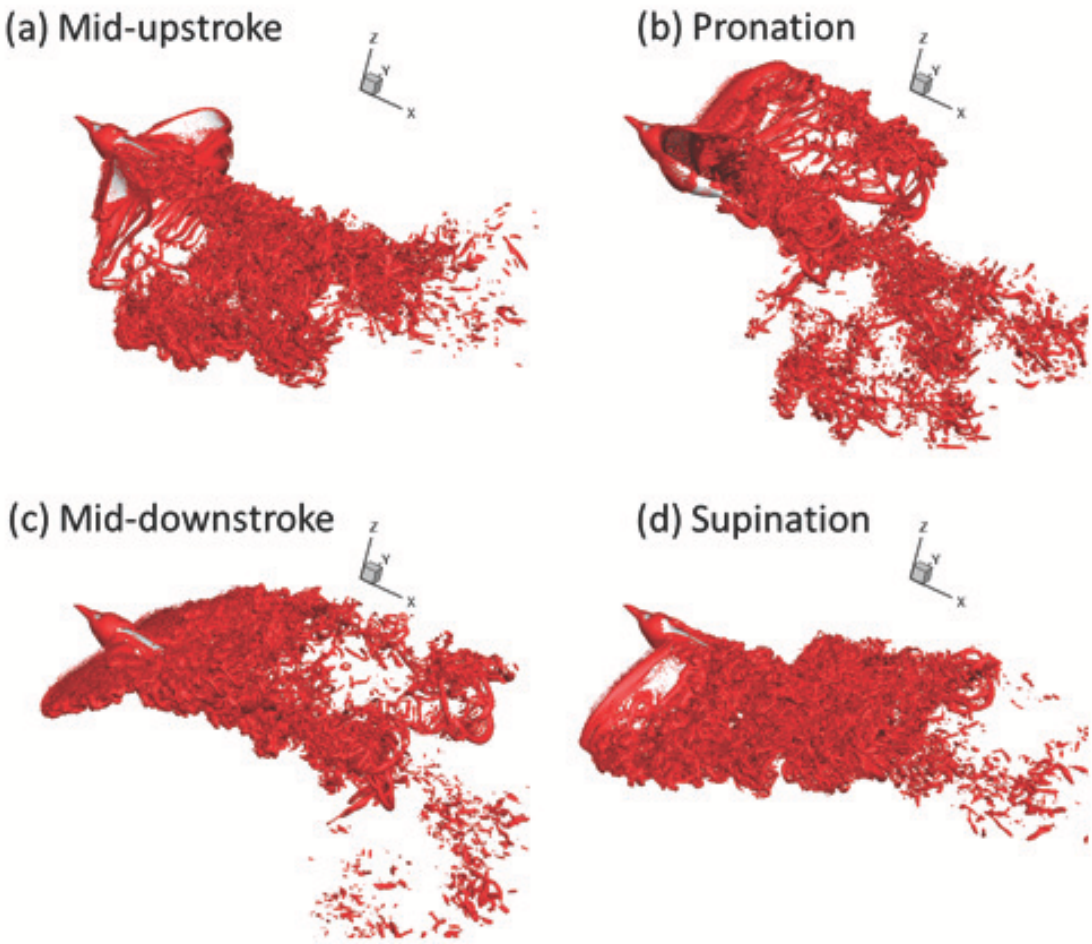

Figure 2.8: Snapshots of flow field within one wingbeat cycle from the hummingbird fast forward flight simulation.

x	y	z	Total	Wall time	Speedup	Efficiency
1	4	16	64	25.0	1.00	100.0%
1	4	32	128	13.2	1.89	95.0%
1	4	64	256	8.3	3.01	75.3%
1	7	64	448	5.0	5.00	71.4%
3	4	16	192	8.5	2.94	98.0%
3	4	32	384	5.0	5.00	83.3%
3	4	64	768	4.0	6.25	52.1%
3	7	64	1344	2.5	10.00	47.6%

Table 2.4: The wall time measured in seconds and parallel performance using domain decomposition on a $450 \times 196 \times 128$ Cartesian mesh for FSI simulation of vocal fold vibration.

2.3.4 Case demo 2: vocal fold vibration

Since this dissertation will focus on vocal fold and heart valve modeling, we apply the parallelization technique to these two problems as well to test its performance. For the vocal fold problem, the background and 3D FSI model setup are described in our work [66] (also Chapter V). The parallel performance is tested by using a stretched $450 \times 196 \times 128$ Cartesian grid (about 11 million mesh points). A 2D domain decomposition is illustrated in Fig. 2.9. The wall time and parallel performance are listed in Table 2.4.

From the results, it can be seen that reasonable efficiency is achieved for near 1000 cores. Note that the mesh size in this case is about 10 times smaller than that in the hummingbird case; thus, lower scaling performance is expected.

2.3.5 Case demo 3: aortic valve

For the aortic valve problem, the background and 3D FSI model setup are described in our works [1, 54] (also Chapters III and IV). The parallel performance is tested for the case where the leaflet thickness is 0.2 mm. A stretched $400 \times 130 \times 130$ Cartesian grid (about 7 million points) is used to discretize the flow domain. A 2D domain decomposition is illustrated in Fig. 2.10. The wall time and parallel performance are listed in Table 2.5.

From the results, it can be seen that reasonable efficiency is achieved for near 700 cores. Note that the mesh size in this case is close to that in the vocal fold case and thus similar scaling performance is expected.

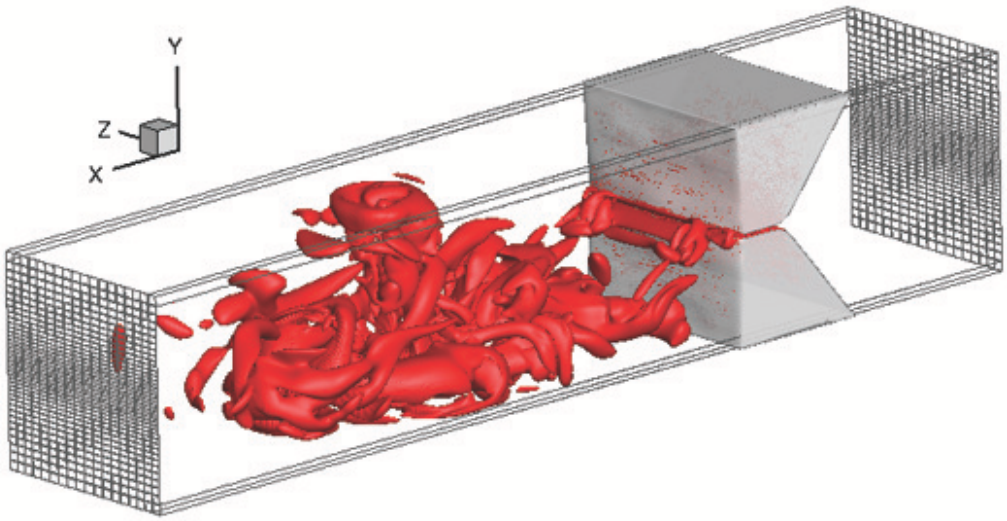

Figure 2.9: Illustration of the flow domain and its 2D decomposition for the vocal fold vibration simulation.

y	z	Total	Wall time	Speedup	Efficiency
5	5	25	11.3	1.00	100.0%
10	5	50	5.7	1.98	99.0%
10	10	100	3.2	3.53	88.3%
13	13	169	2.0	5.65	83.6%
26	26	676	0.6	18.83	69.6%

Table 2.5: The wall time measured in seconds and parallel performance using domain decomposition on a $400 \times 130 \times 130$ Cartesian mesh for FSI simulation of aortic valve.

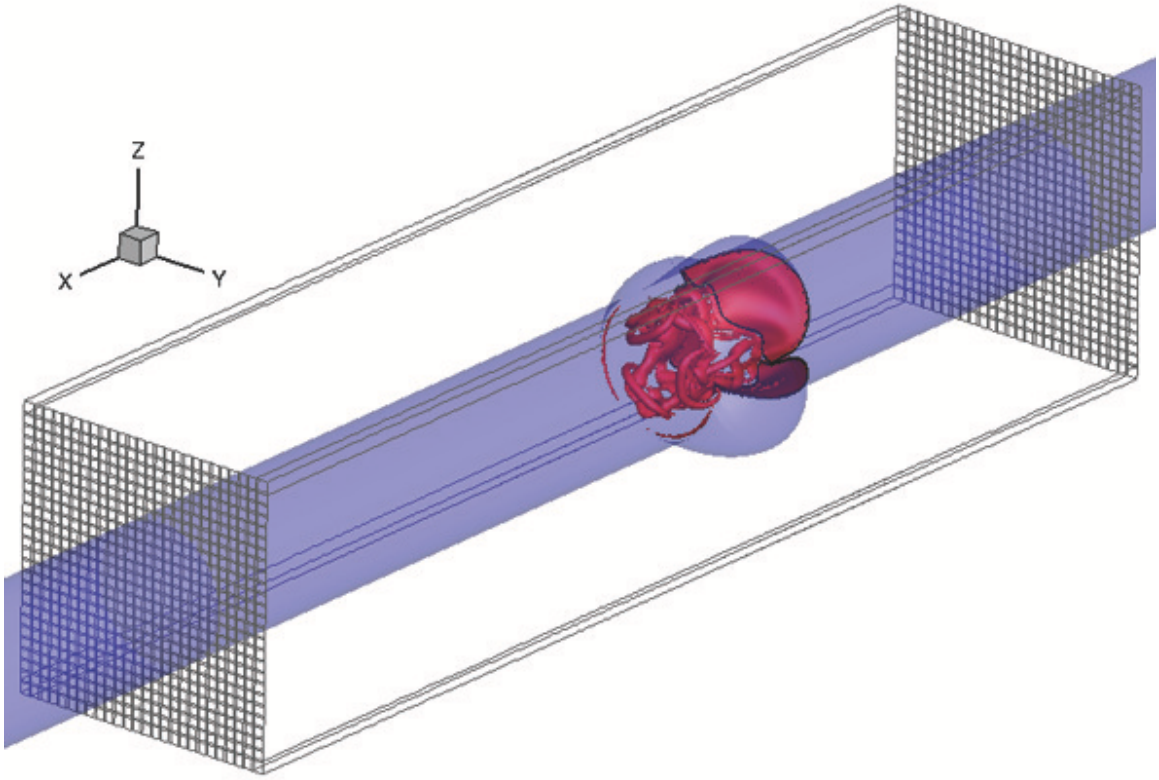

Figure 2.10: Illustration of the flow domain and its 2D decomposition for the aortic valve simulation.

2.4 Conclusion

In this chapter, we described the parallel algorithm for the immersed-boundary method in the flow solver. The parallelization is based on simple domain decomposition, where the flow domain can be divided into multiple subdomains in one, two, or three directions. As a result, thousands of processor cores can be employed to accelerate the costly 3D flow simulation while the total memory usage is not affected significantly.

Chapter III

A computational study of the 3D FSI of aortic valve

3.1 Introduction and significance of the study

In this chapter, we describe a three-dimensional simulation of the fluid–structure interaction (FSI) of the aortic valve using a direct-forcing immersed-boundary method. The geometry of the valve is taken from a bioprosthetic valve, and the computational framework is based on a previous partitioned approach that is versatile for handling a range of biological FSI problems involving large deformations. When applying the approach in the heart valve simulation, we implemented an efficient parallel algorithm based on domain decomposition to handle the costly flow simulation. As compared with previous simulations of the aortic valve, our simulation was able to capture both realistic deformation of the leaflets and vortex structures in the flow, thus providing a balanced modeling approach for the flow and the valve. The results show that the pressure distribution on the leaflet surface is highly nonuniform and the jet flow contains a sequence of vortices during the opening process. After the valve is fully opened, both the three leaflets and the jet still experience significant oscillations due to the high flexibility of the leaflets. The drag resistance of the valve is also characterized, and it is found that the resistance is approximately equivalent to the inertial force of accelerating the fluid column of three diameter length. These details could be potentially used to characterize FSI of the aortic valve.

3.2 Model description and the numerical approach

3.2.1 Model setup

The three-dimensional computational model used is illustrated in Fig. 4.1. The aorta is simplified to a cylindrical tube of diameter $D = 2.1$ cm and length $L = 19$ cm. It has a three-lobed dilation to model the aortic sinuses. These dilation regions were believed to play a significant role in the dynamics of the valve [67–69]. The dimensions of the aortic sinuses in the current model are based on the measurements of the human aortic root [70, 71]. According to the geometric description in Reul *et al.* [71], the cross-section of the aortic sinuses is built with an epitrochoid equation. The aortic valve consists of three flexible semi-lunar leaflets that can independently deform from one another. The overall geometry of the aortic sinuses and leaflets is axisymmetric about the x-axis. Despite of the complexity of anatomy of human aorta, simplified computational domains similar to

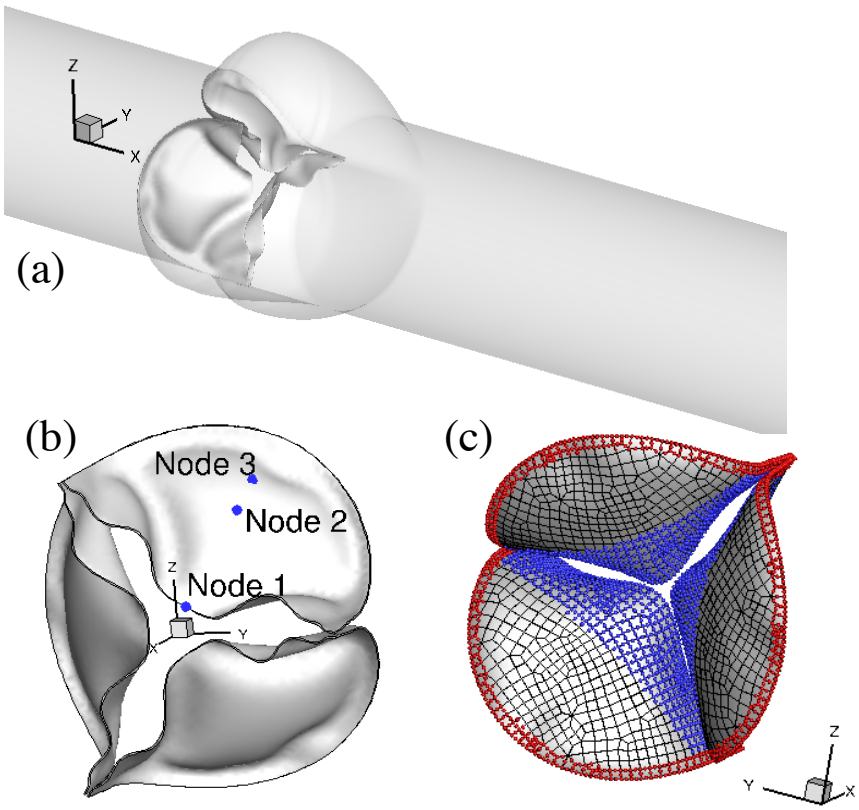

Figure 3.1: (a) Computational model of the aorta root, where the aorta tube and the aortic valve are sutured in the sinus region. (b) A close-up view of the flexible leaflets, where the three markers are used later to plot the displacement history. (c) The fixed nodes (red markers) and prescribed contact detection region (blue markers).

ours are often used for the FSI study of native aortic valve and its prostheses [10–12, 23, 3, 24]. In our study, the geometry of the leaflets (Fig. 4.1(b)) was provided by Prof. Wei Sun's lab at Georgia Tech by courtesy and was extracted from a transcatheter aortic valve (TAV) model [24].

For spatial discretization, the aorta wall is divided into 20,735 triangular elements with refinement in the sinuses region, where the element size is about 0.3 mm. Each leaflet is 0.1 mm thick and consists of a total of 535 finite-element serendipity (20-node Hexahedron) elements and 3,983 nodes. The aorta wall and leaflets are represented by two separate meshes, and they intersect each other without necessarily sharing the nodes. The aorta wall is assumed to be rigid, while the leaflets can undergo free deformations. On each leaflet, 830 nodes located in the commissure region of two neighboring leaflets and also along the base are fixed along with the aorta wall, as shown in Fig. 4.1(c). This type of attachment follows a similar setup for the bioprosthetic valve in Kamensky *et al.* [3] without the stent included. Three nodes in Fig. 4.1(b), one located at the center of the free edge and the other two in the belly region, are used later to show kinematics of the leaflet.

The aortic valve tissue is known to be anisotropic and inhomogenous with leaflet-specific collagen fiber networks [72, 12]. Different constitutive models have been proposed to investigate the mechanical behavior and the failure mechanisms of the aortic valve, e.g., [73, 19, 74]. In our study, the hyperelastic Saint Venant−Kirchhoff model is adopted to represent the tissue behavior of the valvular leaflets. Previous studies have shown that different tissue models produce qualitatively similar deformation patterns for normal valves [3, 23, 24]. The leaflet dynamics is governed by

$$\rho_s \frac{d^2 u_i}{dt^2} + \eta_d \frac{du_i}{dt} = \frac{\partial \sigma_{ij}}{\partial x_j} \tag{3.1}$$

where u_i is the displacement, η_d is the damping coefficient representing structural damping in the tissue, and σ_{ij} is the Cauchy stress tensor. The density of the leaflets is $\rho_s = 1$ g/cm^3, η_d is chosen to be 200 g/cm^3·cs to ensure the reasonable time scale for valve opening and closing in the FSI model. For the elastic properties, we set Young's modulus $E = 1500$ kPa and Poisson's ratio $\nu_s = 0.4$ [3, 23].

The blood is assumed to be Newtonian and incompressible. The governing equation of the flow is the unsteady Navier−Stokes equation

$$\rho \left(\frac{\partial v_i}{\partial t} + \frac{\partial v_i v_j}{\partial x_j} \right) = -\frac{\partial p}{\partial x_i} + \mu \frac{\partial^2 v_i}{\partial x_j \partial x_j}, \qquad \frac{\partial v_i}{\partial x_i} = 0, \tag{3.2}$$

where v_i is the velocity, p is the pressure, ρ is the blood density, and μ is the viscosity. No-slip and no-penetration boundary conditions are imposed at the aorta wall as well as the leaflet surface. the fluid domain is a $19 \times 4.4 \times 4.4$ cm^3 rectangular bounding box and is divided by a $400 \times 130 \times 130$ nonuniform Cartesian grid. Fine resolution with $\Delta_x = 0.025$ cm and $\Delta_y = \Delta_z = 0.034$ cm is used in the region around the aortic valve. The flow is driven by a physiological pressure drop along the aorta. The density and dynamic viscosity of the blood are, respectively, $\rho = 1$ g/cm^3 and $\mu = 0.005$ Pa·s. This blood viscosity is at higher end to reduce the demand for mesh resolution.

To solve the FSI problem, we use a computational framework that was previously developed for simulating biological systems that involve large deformations [53]. In this partitioned framework, the flow is solved using a Cartesian grid based direct-forcing immersed-boundary method, and the solid is solved using a nonlinear finite-element method on unstructured grids. FSI coupling is achieved by iterating the two solvers while communicating boundary conditions at each time step until convergence. The code was verified through various case studies, including both thin-walled and general 3D body problems. In the FSI iteration, the relaxation factors are chosen as $\alpha = 0.7$ for the velocity update, $\alpha = 0.9$ for the force update, and $\alpha = 1.0$ for the displacement update. The convergence criteria are 10^{-5} N, 10^{-2} m/s, and 10^{-3} cm for the nodal force, velocity, and displacement, respectively.

In the simulation, each cardiac cycle has a time duration of $T = 0.86$ sec, which corresponds to a heart rate of 70 beats per minute. For convenience, we will use the centisecond, or cs, as the time unit hereafter. To ensure numerical stability of the FSI coupling, the time step used for the flow solver is $\Delta t = 4.0 \times 10^{-3}$ cs. The time step for the structural simulation is smaller, $\Delta t = 5.0 \times 10^{-5}$

cs, so that each FSI step contains 80 substeps for the solid. Similar to previous models [23, 24], a transient transvalvular pressure load, as shown in Figure 3.2, is applied at the inlet of the aorta tube to drive the flow. The peak pressure during systole is $P_{max} = 2$ kPa, and the lowest pressure during diastole is -8 kPa. The exit pressure is zero. As a complementary study, a uniform pressure load of much lower magnitude is applied directly on the leaflets to open and close the valve without flow. In this structure-only simulation setup, the peak systolic pressure is 0.533 kPa, and the lowest diastolic pressure is -12.67 kPa. These data are consistent with those in previous studies [23, 24].

3.2.2 Parallelization of the FSI simulation

Details of the immersed-boundary method for the flow have been described previously [60, 63]. Some clarifications are needed here as both thin structures (leaflets) and 3D solid bodies (aorta wall) are involved in the present case. Furthermore, a simple domain-decomposition based parallelization has been implemented to accelerate the simulation, and some of the specific issues related to the immersed-boundary treatment should be discussed.

As illustrated in Fig. 3.3(a), all the nodes on the Cartesian grid are divided into four groups [60]: fluid nodes, solid nodes, ghost nodes, and hybrid nodes. The ghost nodes are located within the solid domain and are immediately adjacent to the fluid-solid interface, and the hybrid nodes are located within the fluid domain and are immediately adjacent to the fluid-solid interface. In the current sharp-interface immersed-boundary flow solver, the fluid nodes anchor the standard 2nd-order finite-difference stencil used in the equation discretization, solid nodes are simply dummy nodes, but the ghost nodes and hybrid nodes need special treatment. In particular, each ghost node requires a local extrapolation of the flow field into the solid domain, and each hybrid node requires a combination of the local flow field interpolation and finite-difference discretization of Eq. (3.2). For both types of nodes, the numerical treatment involves a few nearby nodes and the boundary conditions at the fluid-solid interface to support the interpolation, extrapolation, or finite-difference discretization [60].

In Fig. 3.3(a), the aorta tube is treated as a general 3D rigid body containing the region outside of the tube wall. The leaflets are too thin to be resolved by the flow mesh and cannot host ghost nodes inside. Instead, as in the previous work [60], an artificial thickness of 2 to 3 grid intervals is introduced to allow ghost nodes to be defined in the "interior" of the leaflets. For parallel computing, the rectangular box containing the flow domain is divided into a stack of subdomains in the z-direction. Each subdomain only stores the data for its own portion of the flow field but has a full copy of the unstructured mesh of the fluid-solid interface. Since the surface mesh data is much smaller as compared with the volume data of the flow field, this decomposition strategy allows nearly a constant scaling of the total computer memory regardless the number of processor cores being used for the simulation.

Within each subdomain, all four types of nodes are determined independently from other subdomains before solving the flow for the current time step. In addition, the computations related

(a)

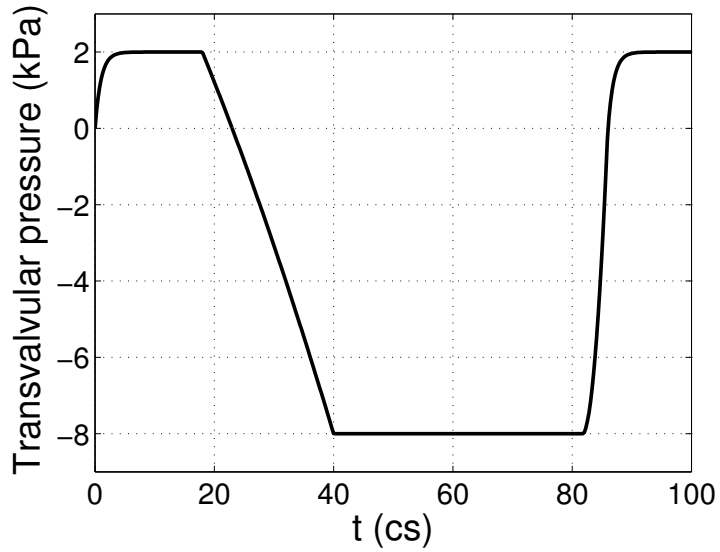

(b)

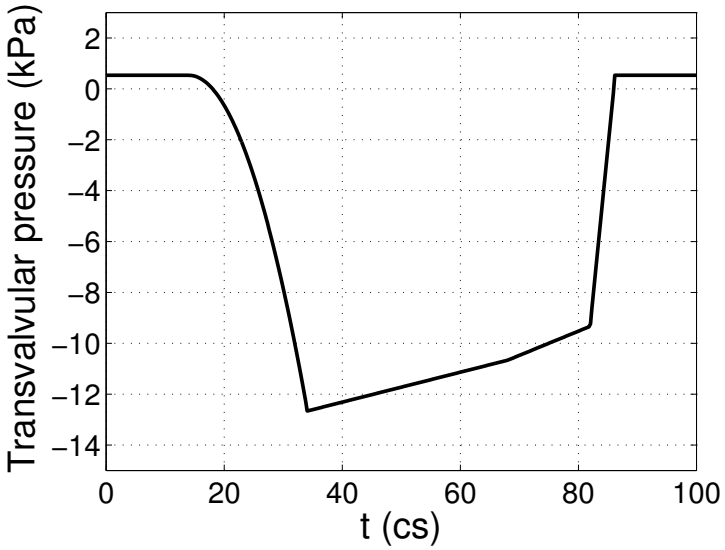

Figure 3.2: Pressure load applied (a) at the inlet of the aorta tube in the FSI simulation and (b) directly on the leaflets in the structure-only simulation, where cs denotes centisecond.

to setting up the interpolation and extrapolation stencils for the ghost and hybrid nodes, and also the computations related to updating these nodes during the solution process, are restricted to the subdomain itself. Therefore, the computational overhead associated with the immersed boundary scales very well with the number of subdomains or with the number of processors. The algorithm of determining whether a node is located inside or outside of a general 3D body was described in Mittal *et al.* [63], and so was the extrapolation algorithm for the ghost nodes. The algorithm for the hybrid nodes was designed to reduce numerical oscillations associated with moving boundaries and was described in Luo *et al.* [60]. These algorithms are directly used here for each processor to compute its own ghost nodes and hybrid nodes while solving the flow within its subdomain. Readers are referred to these references for further detail of the algorithms. Note that some ghost nodes and hybrid nodes could be located near the boundary of the subdomain and their computation may require two slices of flow field to support the interpolation or extrapolation zone as shown in Fig. 3.3(b). Therefore, each subdomain is supplemented with two buffer slices on each side. These slices of data are communicated through the Message Passing Interface (MPI) in the parallel implementation.

In the FSI simulation, a separate processor core handles computation of the solid mechanics so that the fluid and solid partitions can be done in parallel and coordinated through MPI. Furthermore, the finite-element solver of the solid mechanics is parallelized with an OpenMP strategy since the number of solid nodes is much less than that on the flow side and such parallelization provides a balanced cost between the two solvers. For the computing facility, we used the Stampede1 system at the Texas Advanced Computing Center (TACC). Each node contains two Xeon Intel 8-Core 64-bit E5 (Sandy Bridge) Processors with a core frequency of 2.7 GHz. The flow domain is divided into slabs along the z-direction. The speedup of using 2, 8, 32, and 64 CPU cores is 2.1, 6.2, 17.5, and 27.1, respectively, which corresponds to an efficiency of 105%, 78%, 55%, and 42%, respectively. Thanks to the domain decomposition strategy used, the total memory remains nearly constant when the number of cores is varied. Note that the speedup is related to the problem size and the current mesh only has 130 points in the z-direction for decomposition. In a separate test of using $360\times946\times2048$ points, we have achieved the super-linear (i.e., over 100%) performance for up to 1,024 CPU cores; the result was confirmed by the technical staff of the NSF XSEDE through their Extended Collaborative Support Services (ECSS) program.

3.2.3 Contact model

During closing phase and also sometimes in opening as well, the three leaflets can experience significant contact with one another. Similar to previous studies [11, 3], a penalty method is adopted here to prevent the leaflets from penetration. At each time step, potential surface-to-surface contact needs to be checked in order to invoke the contact algorithm. To reduce the computational cost, only the surface nodes within the prescribed contact detection region as shown in Fig. 4.1(c) are checked for contact detection. For each of these nodes, the contact distance is computed by projecting it onto the surface of its neighboring leaflets. The contact force in the

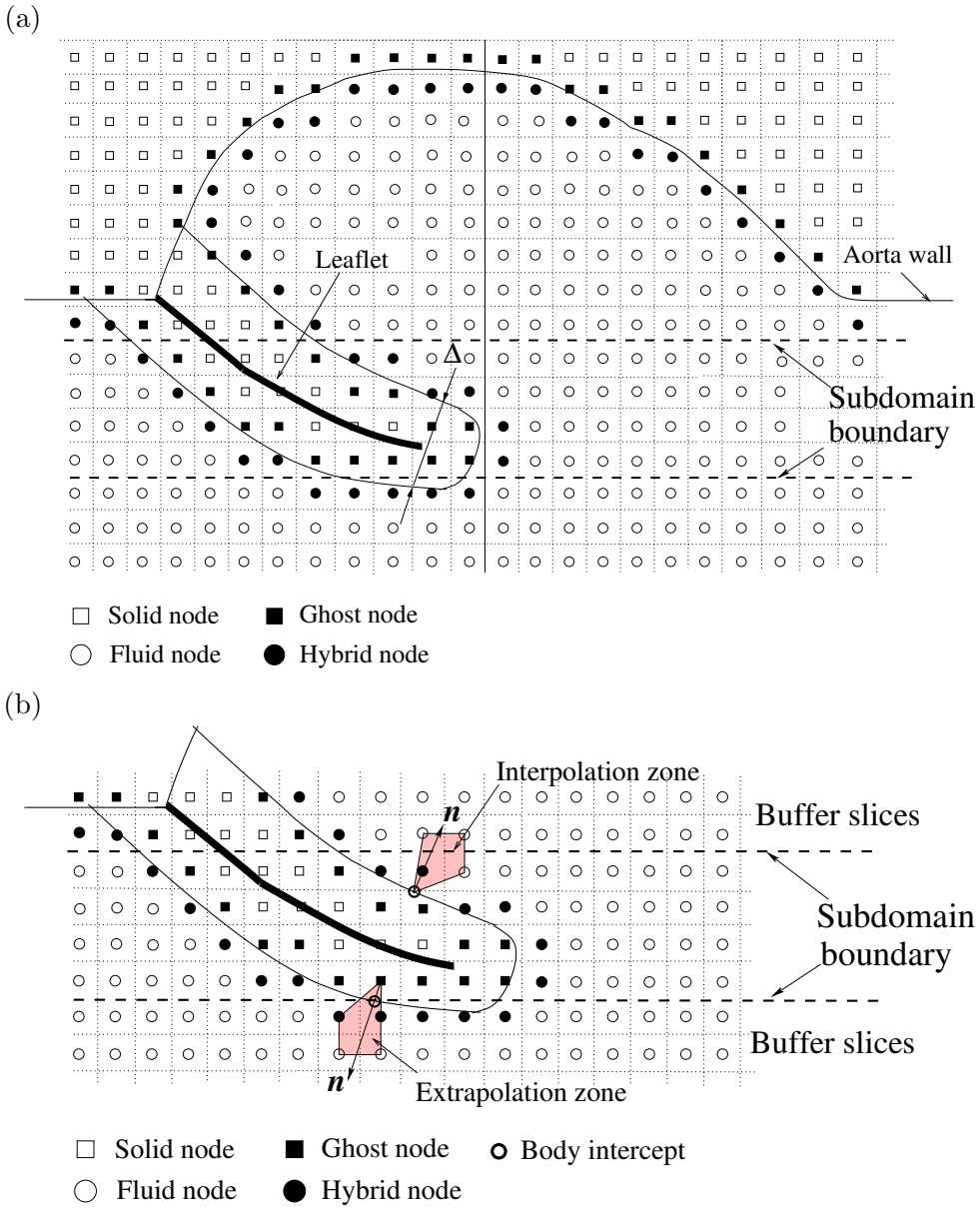

Figure 3.3: (a) Schematic of the immersed-boundary method for the aortic valve simulation, and (b) a subdomain with 2 buffer slices on each side in the parallel implementation. The shaded regions represent the stencil for local interpolation or extrapolation.

direction of the surface normal is then calculated by

$$f_{cnt} = \begin{cases} 0, & \text{if } d - d_0 > 0 \\ -f_{ext} - k(d - d_0), & \text{otherwise} \end{cases} \tag{3.3}$$

where f_{cnt} is the nodal contact force, f_{ext} is the external force (i.e., hydrodynamic force) on the node, d is the contact distance, k is the contact stiffness, and d_0 is a prescribed threshold distance. Within the threshold distance, the external load f_{ext} is canceled out and a net force of magnitude $-k(d-d_0)$ is added to prevent inter-penetration of colliding leaflets. Note that this net force acts on the contact side for both leaflets. The contact force vanishes outside of the contact distance. Here we set $k = 1$ g/cs^2 and $d_0 = 0.08$ cm so that when the leaflets are stopped due to collision, the gap between them is below one cell width on the flow mesh. These parameters may need adjustment if a much finer flow mesh is used. Strictly speaking, when the two leaflets are approaching each other, the lubrication effect may be dominant and the leaflets might never experience solid-to-solid contact [75, 76] due to the presence of a thin liquid film and its high pressure. However, such lubrication effect takes place when the gap is small and the flow is nearly being cut off. Thus, as long as it provides proper kinematic constraints for the leaflets, the exact nature of the contact mechanism should not significantly affect flow or leaflet deformation during the most of the opening and closing phases.

3.2.4 Mesh refinement study

A mesh refinement study is first performed by refining the fluid domain to $500 \times 260 \times 260$ in the x, y, and z, directions, respectively. Around the leaflets, the resolution is doubled in all three directions. In addition, the time step is also halved. The refined FSI simulation is run up to $t = 20$ cs when the valve has already been fully opened and the peak flow is reached. Comparing the results from this simulation and those from the baseline mesh, we obtained a less than 7% error in the peak flow rate. The comparison of the leaftlet deformations is shown in Fig. 3.4 by plotting the transient displacement of the three labeled nodes on one leaflet. The result indicates that dynamic deformations of the valve are well captured using the baseline flow mesh. We also examined the characteristic flow patterns such as the unsteady vortex ring structures in the flow from the baseline mesh, and those results also agree well with the refined simulation.

3.3 Results and discussions

3.3.1 Flow rate and valve opening area

Figure 4.6 presents the transient flow rate in three cardiac cycles for the FSI simulation. The peak flow rate is 431 ml/s for the first cycle and 447 ml/s for the second and third cycles. The difference in the first cycle is caused by the initial condition that sets zero fluid velocity everywhere and a stress-free state for the leaflets. Unless specifically stated, the results presented hereafter are from

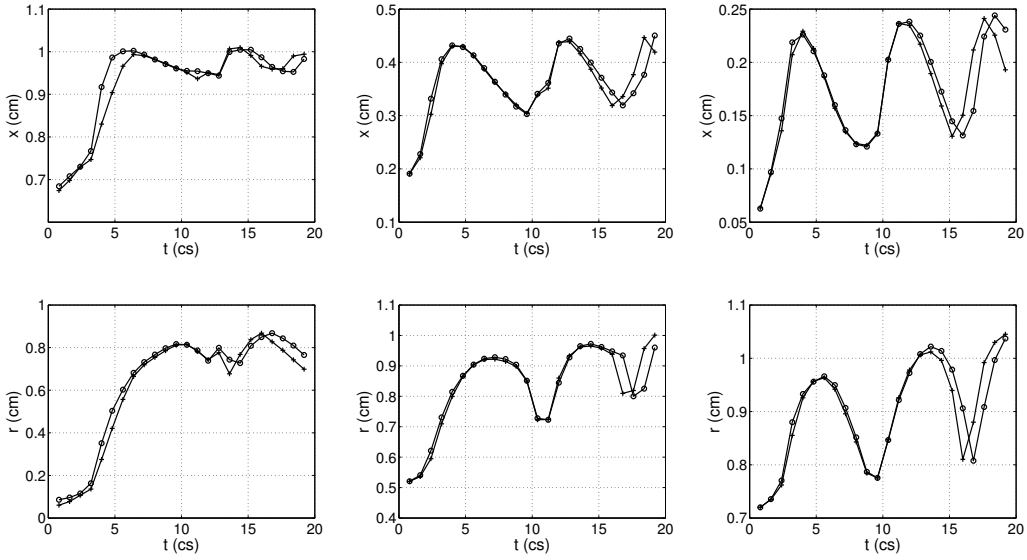

Figure 3.4: Comparison of transient radial and axial displacements of the three labeled nodes on one leaflet (marked in Fig. 4.1(b)) between the baseline mesh (circles) and the refined mesh (pluses). Left: node 1; middle: node 2; right: node 3.

the second and third cycles, where the dynamics of the valve and the flow have reached a periodic state. The peak flow rate obtained in our study is close to previous aortic valve simulations and is within physiological range [10, 23]. Integrating the transient flow rate in time, we obtain a resultant stroke volume that is approximately 89.7 ml per cycle, and the corresponding cardiac output is about 6.3 L/min. Both the stroke volume and cardiac output data are within the physiological range [68, 77]. The effective orifice area (EOA) and dimensionless performance index (DPI) represent a measurement of the valve's resistance characteristics and are often used clinically for the quantification of valve stenosis severity [78, 79]. The EOA in our calculation follows the previous definition [78], $\mathrm{EOA}(cm^2) = Q_{rms}/51.6\sqrt{\Delta p}$, where Q_{rms} is the root mean square systolic flow rate (cm^3/s) and Δp is the mean systolic pressure drop (mmHg). We used the pressure difference between the two ends of the tube to calculate Δp. The present EOA is 1.67 cm^2. The resultant DPI, defined as the ratio between the EOA and the cross section area of the aorta tube, A, is $\mathrm{EOA}/A = 0.49$. Similar results for the EOA and DPI are reported in previous experimental and modeling studies [78, 24]. Regurgitation is the leakage of blood backward through the aortic valve to the left ventricle during diastole. In the current simulation, the regurgitation volume is about 2.6 ml per cycle. This result is also in good agreement with those previous data [78, 24].

The geometric orifice area (GOA) from the FSI simulation is presented in Fig. 3.6 for the three cardiac cycles. This area is calculated by projecting the valve in the axial direction and finding the opening area. From the GOA history, the valve opens rapidly in 5 to 6 cs; the ejection time

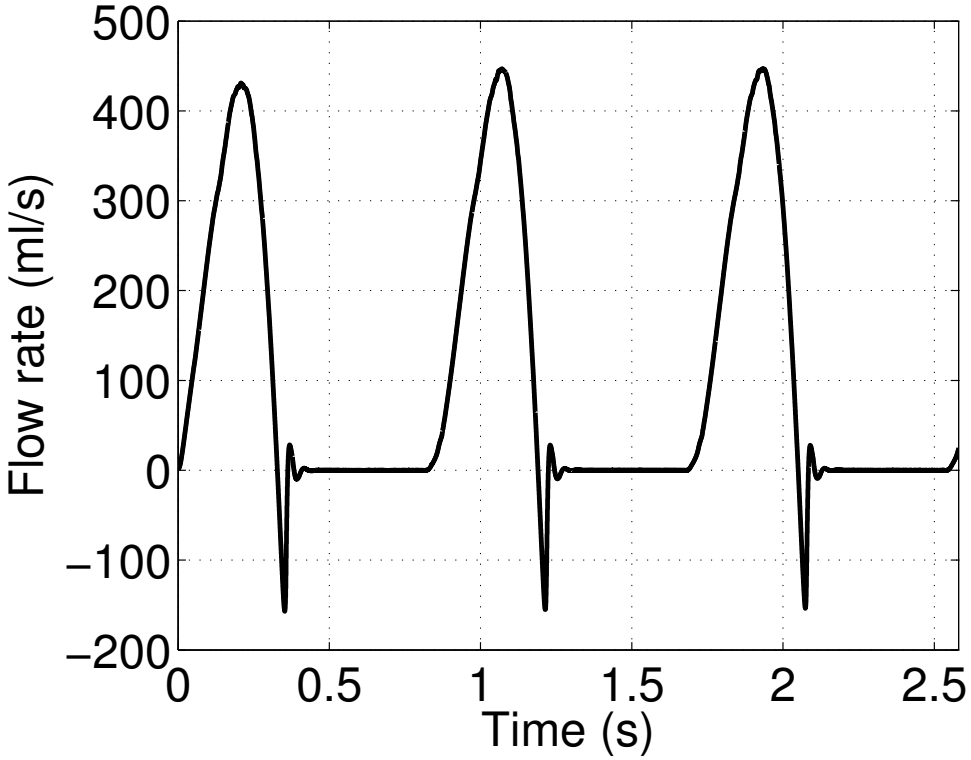

Figure 3.5: Volumetric flow rate, Q, in the first three cycles.

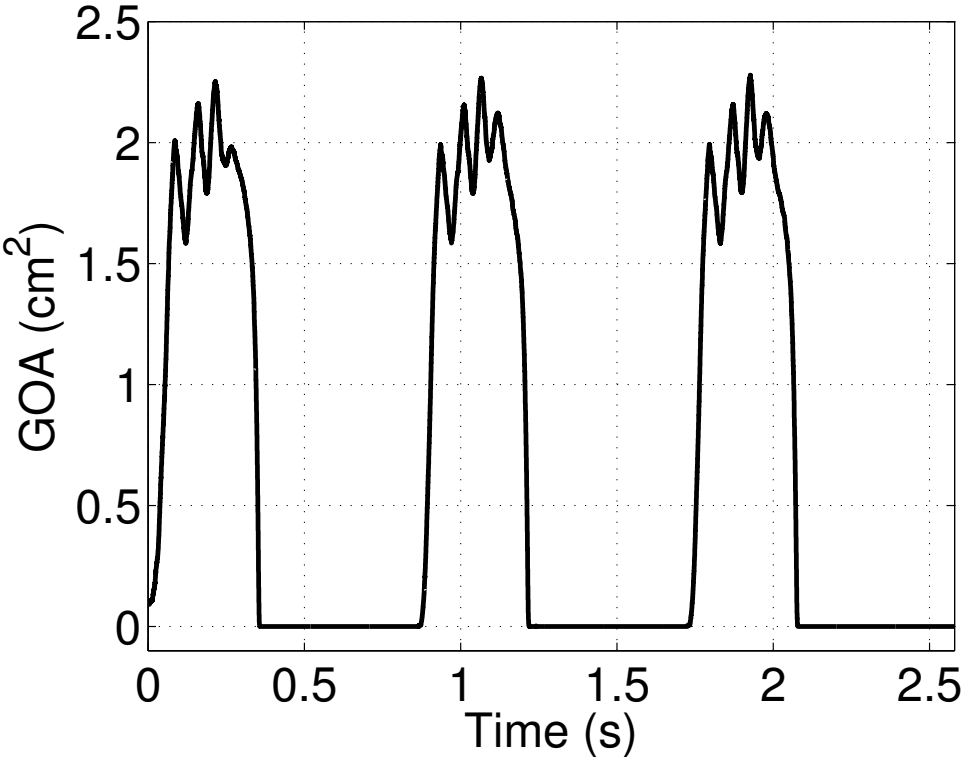

Figure 3.6: History of the geometric orifice area (GOA) in the FSI simulation.

is around 32 cs; and the rapid closure time is from 3 to 4 cs. These results agree well with the previously reported data [68, 24]. The peak GOA is around 2 cm^2. During the opening phase, some oscillations can be seen in the GOA. Such oscillations are also captured by a fiber-reinforced hyperelastic tissue model in Mao *et al.* [24] and in present study is related to the leaflet oscillation that will be discussed later.

3.3.2 Leaflet deformation and pressure distribution

Figure 3.7 shows the opening and closing phases of the aortic valve in both structure-only and FSI simulations. Similarities as well as differences can be found in terms of the leaflet deformation between these two simulations. First, in the opening phase the aortic valve opens faster in the structure-only simulation than in the FSI simulation. The valve in the structure-only simulation becomes fully open at $t = 3$ cs, while it is still not yet fully open until $t = 5$ cs in the FSI simulation. The exact opening time has to do with the magnitude of the pressure load applied, which is different in the two simulations. What is more important in this figure is the comparison of the deformation pattern. In both simulations, the belly region of the leaflets opens in the beginning of the process and arches towards the aortic sinuses. However, because of the uniform pressure load applied in the normal direction of the valve surface, the free edge region of the leaflets in the structure-only

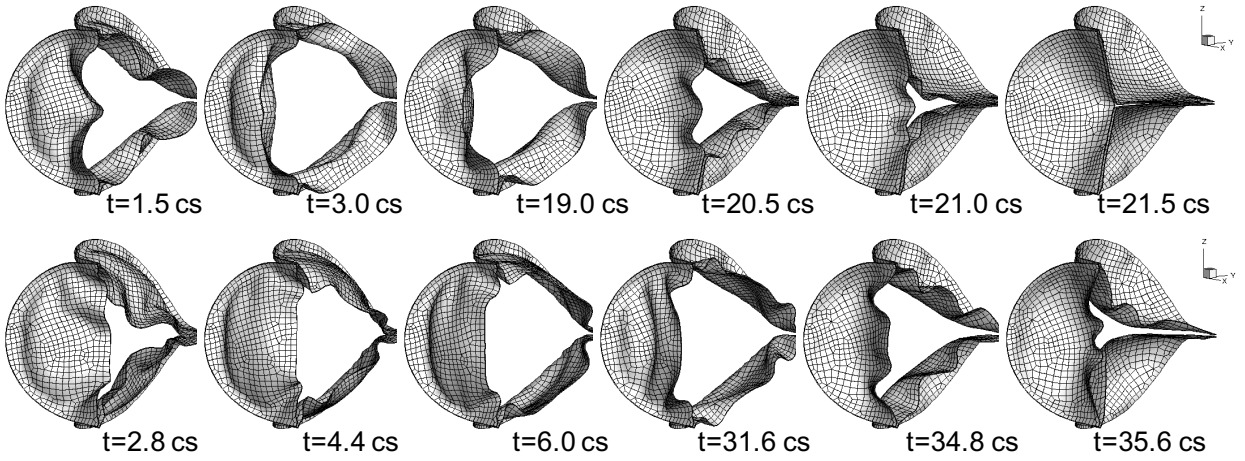

Figure 3.7: Deformation sequence of the valve under (upper row) a uniform pressure loading in the structure-only simulation, or (lower row) the hydrodynamic pressure in the FSI simulation.

simulation moves immediately in the opening phase and is seen to bend outward as in Fig. 3.7(a). In contrast, in the FSI simulation the load acted on the leaflet surfaces is based on the actual transient blood flow field and the free edges do not open immediately. Instead, the belly region of the valve have a faster opening than the free edge region, and as a result, the free edge region bends inward and the entire valve forms roughly a converging nozzle. Such deformation pattern in FSI is consistent with the *in-vivo* observation in [80] and is also reported in previous FSI simulations [23, 24]. To explain this deformation pattern, we visualize the pressure distribution on the leaflet surfaces in Fig. 4.8. The pressure on the leaflet surface is extracted by interpolation from the flow mesh [63]. In this figure, the contours of the pressure on the left ventricle side of the valve are plotted. It can be seen that the pressure in general varies in time according to the boundary pressure applied at the inlet (Fig. 3.2(a)); however, the pressure distribution is highly nonuniform during much of the cardiac cycle as long as the valve is not fully closed and flow can go through the valve. Since the valve is overall a converging nozzle, flow speed is naturally faster near the nozzle exit, where the pressure drops in magnitude. Therefore, the pressure load near the free edges is lower as compared with the pressure load near the belly region, and consequently, the belly region has a faster opening speed.

In the closing phase, Fig. 3.7 shows that the free edge region in the structure-only simulation close nearly uniformly due to the prescribed uniform pressure load, and this region moves faster than the rest of the leaflet. In the FSI simulation, the free edge region remains open at $t = 31.6$ cs. As later closing state, e.g., $t = 34.8$ cs and $t = 35.6$ cs, the free edge region still bends outward so that the valve forms a converging-diverging nozzle. This deformation pattern is consistent with the negative pressure distribution on the ventricle side of the valve in Fig. 4.8. At $t = 34.8$ cs and $t = 35.6$ cs, the negative pressure on the ventricle side is lowest near the belly region, causing this region to move inward earlier than the other regions.

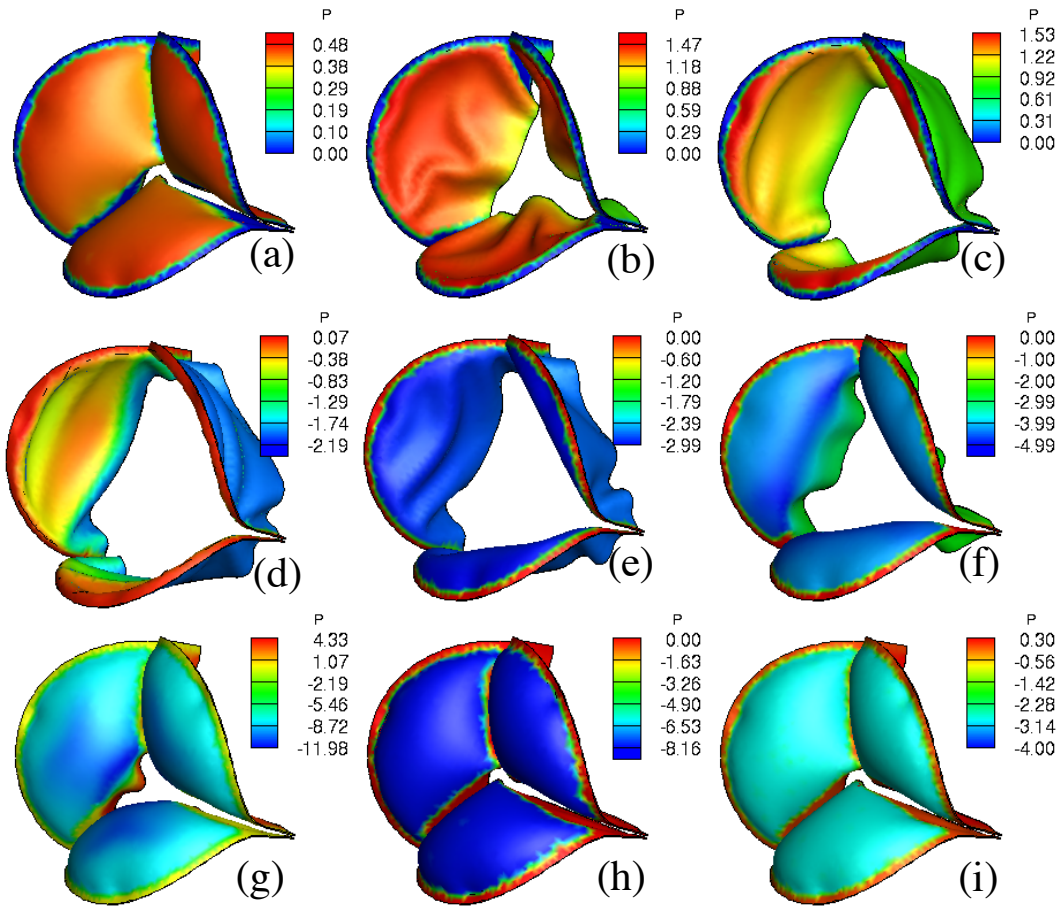

Figure 3.8: Pressure distribution (unit: kPa) on the ventricle side of the valve in FSI simulation at $t = 0.4$, 2.8, 6.0, 23.6, 32.4, 34.8, 35.6, 53.2, 85.2 cs (a-i). Note that the color range is different in each frame. The colors at the fixed leaflet edges and the contact area are not meaningful (because of no fluid contact).

These differences in the leaflet kinematics observed between the structure-only and the FSI simulations were also discussed previously [23, 24]. However, the detail of the pressure distribution was not reported. Given the geometrical symmetry as well as the load symmetry, the valve deformation in the structure-only simulation is symmetric. However, in the current FSI simulation asymmetric opening and closing of the valve are observed (Fig. 3.7(c,d). This asymmetry of the valve deformation is consistent with previous computational [23, 13, 24] and *in vitro* experimental [81] studies, and it is related to the asymmetry in the flow that will be discussed later. We point out that the shear stress can be extracted from the flow simulation as well. Since its magnitude is much smaller as compared with the pressure, we have included it in a supplementary figure without further discussion here.

After the full closure of the valve, the pressure distribution on the ventricle side turns uniform

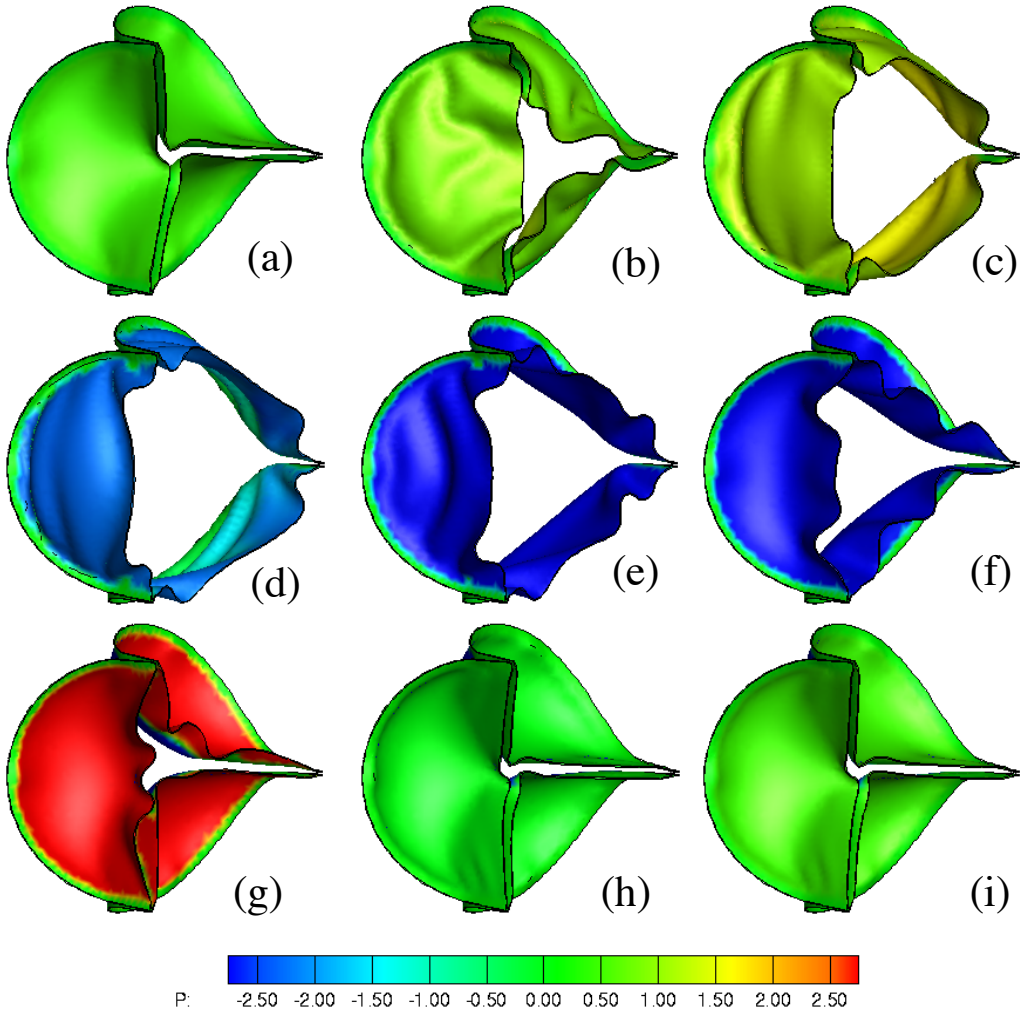

Figure 3.9: Pressure distribution (unit: kPa) on the aortic side of the valve in FSI simulation at $t = 0.4$, 2.8, 6.0, 23.6, 32.4, 34.8, 35.6, 53.2, 85.2 cs (a-i).

(Fig. 4.8(h,i)). Fig. 3.9 shows that throughout the cardiac cycle, the pressure distribution on the aortic side of the valve is quite uniform. On this side, pressure can either positive or negative, depending on the phase in a cycle. During initial opening in first few centiseconds (Fig. 4.8(a-c)), the pressure on the aortic side is positive because of leaflet acceleration. Later after the valve is fully opened, the pressure becomes negative (Fig. 4.8(d-f)) due to the high flow speed through the valve. Before the full closure and immediately after, the pressure turned positive again and its magnitude becomes high (Fig. 4.8(g,h)). This high pressure impact is caused by the fast closure of the aortic valve and is well-known as the "water hammer effect".

3.3.3 Leaflet dynamics

The opening and closing dynamics of the valve are better seen in position tracking of the three labeled markers. Fig. 3.10 shows both the radial and axial positions of the three markers. As a reference, detail of the waveform of the the flow rate is also plotted here. From the marker-tracking plots, it can be seen that the valve opening-closing has generally four stages: (1) rapid opening with large displacement, (2) maintenance of maximum excursion with small-amplitude oscillations, (3) slow initial closing, and (4) rapid closing. Among these stages, the rapid opening only takes about 5 to 6 cs, the maximum excursion about 19 cs; the slow closing about 7 cs, and the fast closing about 3 cs. These dynamic characteristics are consistent with previous high-speed recording of the actual leaflet motion [80, 82].

At the maximum excursion stage, the three leaflets continue to oscillate like flapping flags immersed in an incidental flow, whose traveling-wave motion is induced by instability of the coupled fluid-structure system. Note that such oscillation is not observed in the structure-only simulation. Fig. 3.10(a) shows that the magnitude of the oscillation is about 2 mm at the belly and 1.4 mm at the free edge, and the frequency is 14.7 Hz (thus, the period is 6.8 cs). An animation of the leaflet motion is provided in supplementary materials. From the phase delay of the oscillation among the three nodes, we can calculate the phase speed of the traveling wave, which is about 0.25 m/s. This flapping oscillation of the leaflets has to do with the jet oscillation and vortex dynamics in the flow, which will be discussed later.

3.3.4 Momentum balance

Analyzing the flow resistance of the valve could be useful for the study of the transvalvular pressure difference and also for the resistance performance of prosthetic valves [78]. Consider the interior of the aortic wall as a control volume, we may analyze the momentum balance of the flow and the overall force on the valve. First, the momentum conservation of the flow in the axial direction is

$$\frac{\partial}{\partial t}\int \rho u \,\mathrm{d}V + \int \rho u^2 \,\mathrm{d}A = (P_1 - P_2)A - F_{val} - F_{sin} - F_{tub}, \tag{3.1}$$

where u is the axial velocity, $A = \pi D^2/4$ is the area of the cross section, P_1 and P_2 are the inlet and outlet pressure, respectively, F_{val} is the total axial hydrodynamic force on the leaflet surfaces

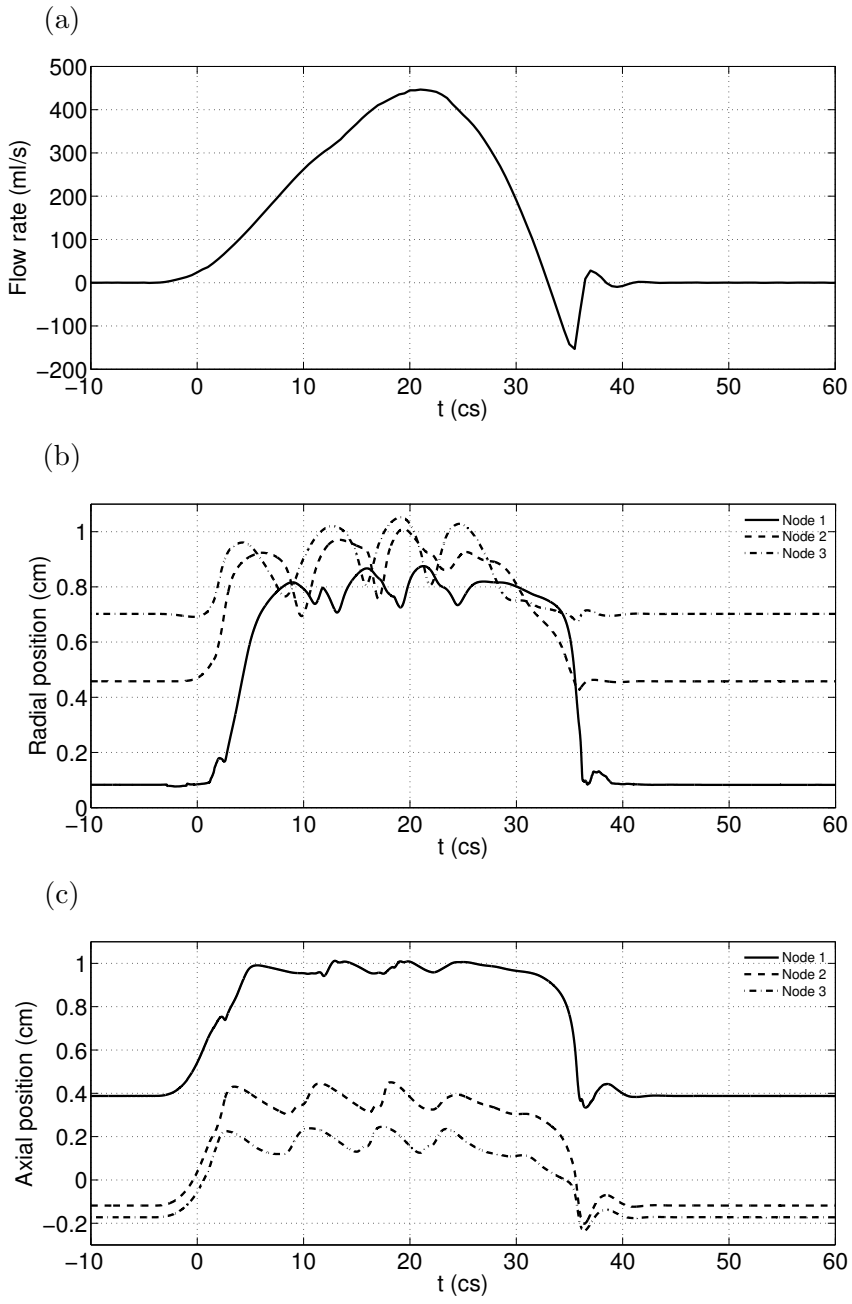

Figure 3.10: Flow rate (a), radial (b) and axial (c) positions of three labeled markers in a cardiac cycle of FSI simulation.

(both aortic and ventricle sides included), F_{sin} is the axial force on the sinus section of the wall, and F_{tub} is the axial force on the remaining tube wall. Introducing the flow rate, Eq. (4.1) can be written as

$$(P_1 - P_2)A = \rho L\dot{Q} + \int_{\text{out}} \rho u^2 \, \mathrm{d}A - \int_{\text{in}} \rho u^2 \, \mathrm{d}A + F_{val} + F_{sin} + F_{tub}, \tag{3.2}$$

where $\dot{Q} = \frac{\mathrm{d}Q}{\mathrm{d}t}$ is the time derivative of the flow rate.

The right-hand side terms in Eq. (4.2) are directly evaluated from the simulation and are plotted in Fig. 3.11 for comparison along with the pressure loading at the inlet. In the figure, it can be seen that the momentum flux at the outlet is almost equal to the momentum flux at the inlet. Therefore, these two terms nearly cancel each other in Eq. (4.2). Among the rest of the terms, the inertial force of the fluid, $\rho L\dot{Q}$, is the highest during initial opening as well as most of the systole before the inlet pressure starts to drop at $t = 18$ cs. This result means that most of the boundary pressure loading is used for acceleration of the fluid column in the tube. However, the net force on the valve leaflets is also quite significant. During valve opening at $0 < t < 5$ cs, the normalized valve force $F_{val}/(P_{max}A)$ can reach as high as 0.3. At $t = 7$ cs when the valve has been fully open, $F_{val}/(P_{max}A)$ drops to 0.13. Then as the flow rate continues to rise, $F_{val}/(P_{max}A)$ is increased and oscillates between 0.24 and 0.54 due to the flapping motion of the leaflets.

Since the inertial force of the fluid is proportional to the total mass of the fluid column and depends on the choice of the fluid domain length, another way of assessing F_{val} is to compare it with the equivalent length of the fluid column being accelerated in terms of the valve diameter, i.e., $F_{val}/(\rho D\dot{Q})$, where D is the tube diameter. From the results in Fig. 3.11, $F_{val}/(\rho\dot{Q}) = 3.95D$ at $t = 2$ cs, which means that F_{val} is equivalent to the inertial force of accelerating approximately four diameters ($4D$) of fluid column at the time. During rapid opening from 1 to 6 cs, the average result is $3.1D$. At $t = 7$ cs when the flow rate has the maximum acceleration, $F_{val}/(\rho\dot{Q})$ drops to $1.5D$. During the entire acceleration time (0 to 21 cs), the ratio between the average F_{val} and the average $\rho\dot{Q}$ is $4.4D$.

When the boundary pressure becomes negative and the flow is decelerating between $t = 21$ and 33 cs, F_{val} remains positive. When the valve is fast closing after $t = 35$ cs, the flow is reversed, and the force on the valve quickly becomes negative. The reversal flow is immediately stopped by the full closure of the valve. However, the impact force of the fluid on the leaflet becomes very high as a result of the water hammer effect. The spike in Fig. 3.11 indicates that $F_{val}/(P_{max}A)$ reaches nearly 10.

In comparison with F_{val}, the total shear on the present segment of the tube wall, F_{tub}, is small. The force on the sinus wall, F_{sin}, is much smaller than F_{val}. Therefore, it is reasonable to use F_{val} alone to calculate the drag coefficient of the aortic valve and ignore F_{sin}. We may use the peak momentum flux at the inlet, $I_{max} = \int \rho u^2 \, \mathrm{d}A = 13.3$ N to define the drag coefficient, so that $C_D = 2F_{val}/I_{max}$. From Fig. 3.11, the maximum drag coefficient is 1.04 near $t = 18$ cs. Note that at that moment, even though the valve is open, the flow rate is high and the valve still undergoes flapping motion, which causes the force on the valve to be large. During the entire period of systole

(a)

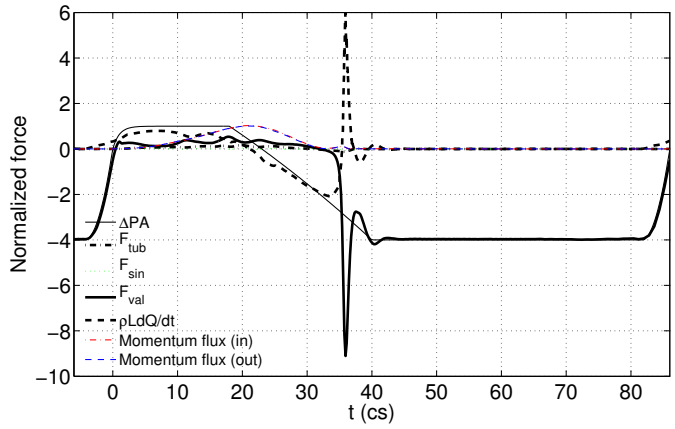

(b)

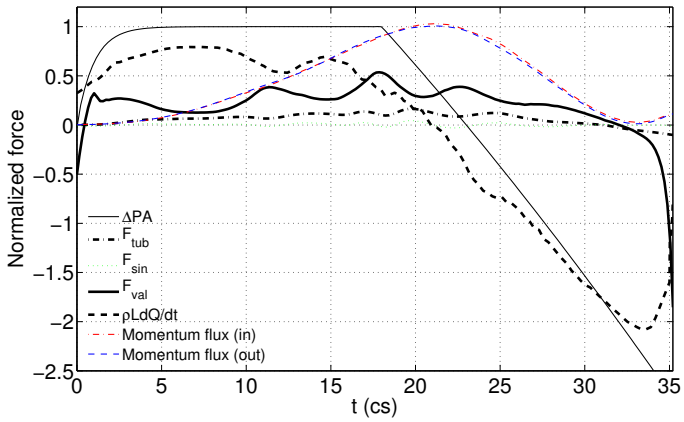

Figure 3.11: Momentum balance within a cycle, where the force terms have been normalized by $P_{max}A$. (b) is a zoom-in view of (a).

from $t = 0$ to 33 cs, the average C_D is 0.47.

3.3.5 Velocity field

Fig. 3.12 shows a few snapshots of the flow field by plotting the contours of the u-velocity in the yz-planes at several axial locations. These contours indicate how the shape of the pulsatile jet changes with time and location. Note that the shape of the nozzle formed by the leaflets may change from roughly a star to a triangle and to a hexagon during opening and closing, as seen in Fig. 3.9. Such shape changes have a direct impact on the jet. In Fig. 3.12(a) where $t = 6$ cs, the jet immediately after the valve exit has a similar shape to the hexagon nozzle formed by the valve at the moment. The profiles in the downstream slices may reflect the nozzle shape in earlier moments but could also have been changed by the inertial effect of the fluid. For example, the jet profiles in slices 2 and 3 have a triangular shape but are opposite in orientation. This jet flipping phenomenon

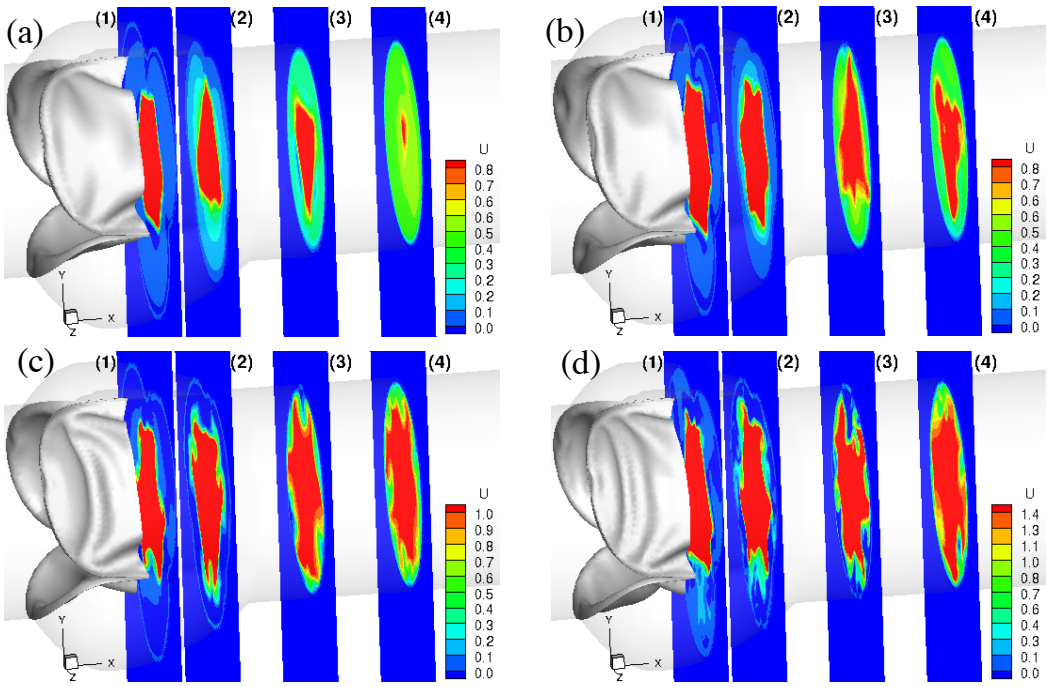

Figure 3.12: Contours of u-velocity at time $t = 6$ cs (a), 7.6 cs (b), 10.8 (c), and 23.6 (d). The four slices are located at $x/D = 0.1$, 0.4, 0.9, 1.4 from the exit of the valve.

was studied previously in the context of a stationary noncircular nozzle/steady jet [83, 84], where jet flipping happens at axial locations between $x/D = 0.1$ and 1.0. The jet profile in slice 4 of Fig. 3.12(a) has lost its original shape since leaving the nozzle and has become more circular.

In Fig. 3.12(b) where $t = 7.6$ cs, both slice 1 and slice 2 maintain the hexagon shape of the jet, and the triangular shapes of opposite orientations have moved downstream and showed up in slice 3 and 4. In Fig. 3.12(c,d) where $t = 10.8$ and 23.6 cs, respectively, the valve is fully open, and flow continues to accelerate ($t = 10.8$) or is reaching its maximum speed ($t = 23.6$). In those two frames, the jet no longer has a well-defined shape due to substantial unsteady motion of the flow. Even at slice 1, the jet profile may be significantly different from the shape of the nozzle because of the effect of the oscillatory motion of the leaflets on the jet. Jet flipping is still visible between some of the slices, e.g., slices 2 and 3 in Fig. 3.12(c,d).

Fig. 3.13 shows the velocity field in the slice at $y = 0$ that cuts through two leaflets and the domain axis for $t = 5.2$, 14, 21.2, and 23.6 cs (see Fig. 4.1(a,b) for the slice location). In Fig. 3.13(a,b), the flow field is symmetric at the early opening stage. Furthermore, Fig. 3.13(a) shows that the pulsatile jet is led by two vortex rings near its front; behind these two vortex rings, the diameter of the jet follows opening of the valve, i.e., increasing as it is closer to the valve exit. Later in Fig. 3.13(b) when the valve is completely open, the jet is characterized by several vortex rings along the axial direction. These vortex rings are formed because the shear layer instability that takes place between the jet and the surround fluid in the sinuses or near the aorta wall.

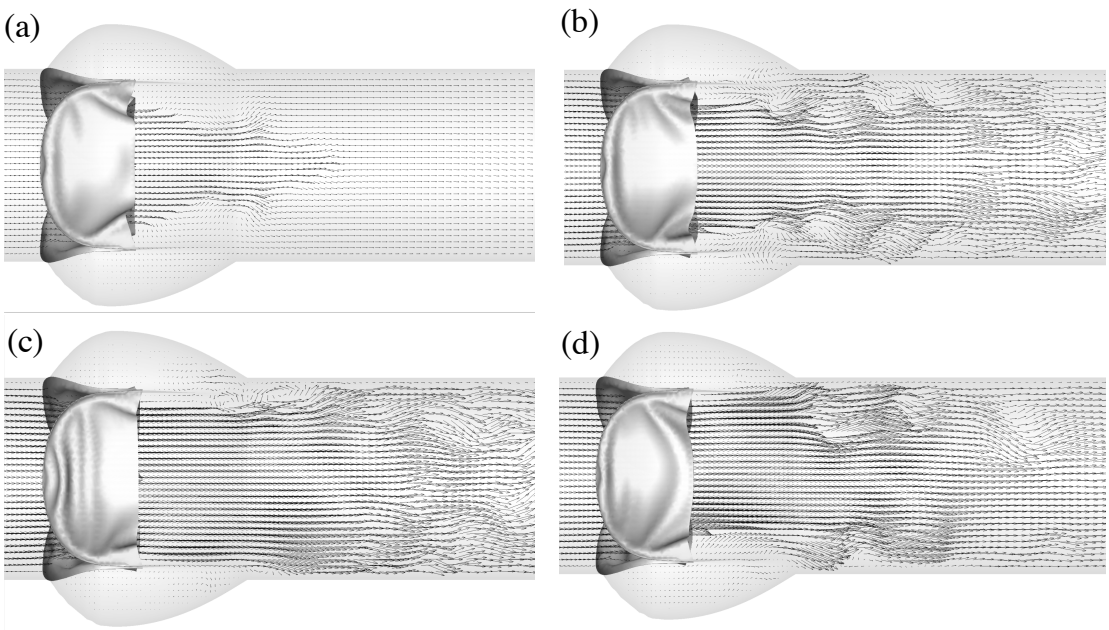

Figure 3.13: Velocity vectors in the $y = 0$ plane at $t = 5.2$, 14, 21.2, 23.6 cs. Only every one out of two points is shown in each direction.

These vortices interact with the wall, and their growth is confined by the presence of the wall, as opposed to a free jet whose shear layer vortices are unconfined. As flow continues to accelerate, symmetry breaking takes place due the inertial effect at high Reynolds numbers. In Fig. 3.13(c), the jet immediately next to the valve exit is skewed toward the lower side of the sinus wall, while in Fig. 3.13(d), the jet moves toward the opposite sinus wall immediately after leaving the valve. Therefore, the entire jet appears to be oscillating continuously, instead of going straightforward, after the valve is fully opened. We point out that this oscillatory jet motion was also observed in a recent *in vitro* experiment study of the aortic valve [85].

The vortices and flow recirculation in the sinus region are also of interest due to their possible role in the leaflet dynamics [67–69]. In Fig. 3.13, the flow pattern in the sinuses is not clear because of low fluid velocity. We have visualized the streamlines in a supplementary figure, where the 3D recirculation in the sinus region bears certain similarity with images from in vivo experiment (e.g., Figure 4 in Markl *et al.* [86]). Since these vortices highly depend on the geometry of the sinuses and available experimental data is limited, further comparison is not straightforward and is deferred to future study along with examination of the role of the vortices.

Fig. 3.14 shows the velocity field for $t = 16.4$ to 20.4 cs in the slice at $z = 0$ that cuts through only one leaflet and divides the domain symmetrically (see Fig. 4.1(a,b) for the slice location). This slice provides a better view of the leaflet oscillation as well as the interaction with the jet. From Fig. 3.14(a) to (f), the two leaflets in the view clearly display a wave traveling from their base to the free edge, which leads to a secondary flapping oscillation of the leaflets beyond their

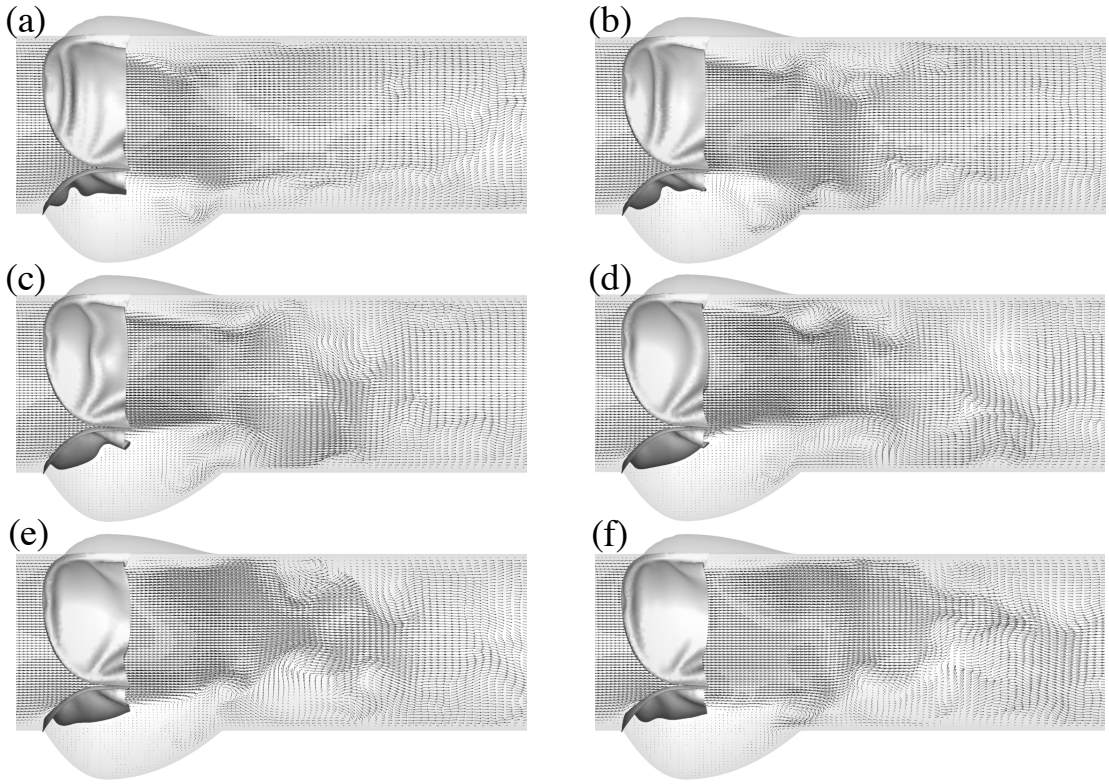

Figure 3.14: Velocity vectors in the $z = 0$ plane at $t = 16.4$, 17.2, 18.0, 18.8, 19.6, and 20.4 cs. Only every one out of two points is shown in the axial direction.

initial displacement during opening. This oscillation was also shown by the tracing of the markers in Fig. 3.10. Even though the magnitude of this flapping motion is smaller as compared with the overall opening/closing motion of the leaflets, it has a direct impact on the jet near the valve exit. From this figure, the leaflet at the bottom can either lift up the jet away from (Fig. 3.14(d,e)) or direct it toward (Fig. 3.14(a,b)) the nearby wall through its flapping motion. Therefore, the frequency of the jet oscillation corresponds to the flapping frequency of the leaflets. The jet skewness changes the location where the jet reattaches to the aorta wall and thus causes significant dynamic interactions between the jet and the wall (an animation of the velocity field is provided in supplementary materials). In addition, large vortices can be generated at the shear layer between the jet and the opposite side of the wall, leading to rich vortex dynamics as discussed next. We should point out that the traveling-wave motion of the leaflets is likely associated with the thin thickness adopted in the present study, and this type of motion is not observed in some of the recent experiments where thicker leaflets were used [87]. In a separate study, we have doubled the thickness and still clearly see a similar wave motion. Since the thickness of the native and prosthetic leaflets can vary from 0.16 mm to 1 mm [13, 88], this traveling-wave result may be only applicable to very thin leaflets. On the other hand, it may be worthwhile to study in the future that how this behavior varies with the leaflet thickness and stiffness.

3.3.6 Vortex dynamics

Fig. 3.15 shows a sequence of the vortex structures in the flow by plotting the isosurface of the imaginary part of the complex eigenvalue of the velocity gradient tensor. When the valve is opening from complete closure, distinct vortex rings are formed around the starting jet. There have been many studies about vortex ring formation for pulsatile jets, including discussions of optimal vortex ring formation in the applications of propulsion as well as heart valves [89]. However, details of these vortices in the native aortic valve have been scarcely studied. In the present study, we visualize the 3D shape of these vortices and their evolution with the hope that it can lead to future in-depth study on the vortex dynamics of the aortic valve. Fig. 3.15(a) shows the leading vortex ring at the front of the jet and the following second ring. As the jet is further advancing, more vortex rings are formed due to roll-up of the unstable shear layer around the jet. In Fig. 3.15(b,c), a third vortex ring can be seen behind the second ring. These rings sometimes are loosely connected to form roughly a closed loop. In addition, these rings are not completely separated but are interconnected through vortex filaments.

In Fig. 3.16, we plot the time-dependent locations of the first three vortex rings during valve opening. It can be seen that the distances between these rings gradually increase, which is due to increase of the flow speed. We also examined the shape of these vortex rings. The first ring maintains roughly a circular shape. However, the second ring changes significantly during evolution, and this is shown in Fig. 3.17. Initially, this ring has three lobes that move faster downstream than the rest part of the ring (Fig. 3.17(a)). Then the ring becomes more rounded, and rear part catches up the three lobes so that the entire ring is less stretched in the axial direction (Fig. 3.17(b,c)). Later this ring becomes triangular (Fig. 3.17(d,e)) and then tortuous with three different lobes formed and stretched backward in the axial direction (Fig. 3.17(f)). The third ring also experiences dynamic shape change, but since it is short-lived as compared with the first two rings, its shape is not discussed in detail here.

In Fig. 3.15(d) where $t = 10.8$ cs, another ring is visibly formed, but at this point the earlier vortex rings start to break down and become less identifiable. Later as the flow rate continues to increase (Fig. 3.15(e)) and then reaches its peak (Fig. 3.15(f)), the vortex rings are no longer formed. Instead, the vortices quickly break up and form longitudinal filaments that do not have a clear organization. An animation of the vortices is provided in supplementary materials. Such vortex breakup has to do with the increased Reynolds number as the flow rate is growing during diastole, but the breakup process could have been accelerated due to the oscillations of the jet and interactions of the vortices and the aorta wall that were discussed in the previous section. Further study will be done in the future to investigate how the vortex dynamics observed here is affected by the choice of the nondimensional parameter in the FSI model. Since the current study is limited to a straight tube, one particular focus may be how the curvature of the aorta arch affects the vortex dynamics [22, 16].

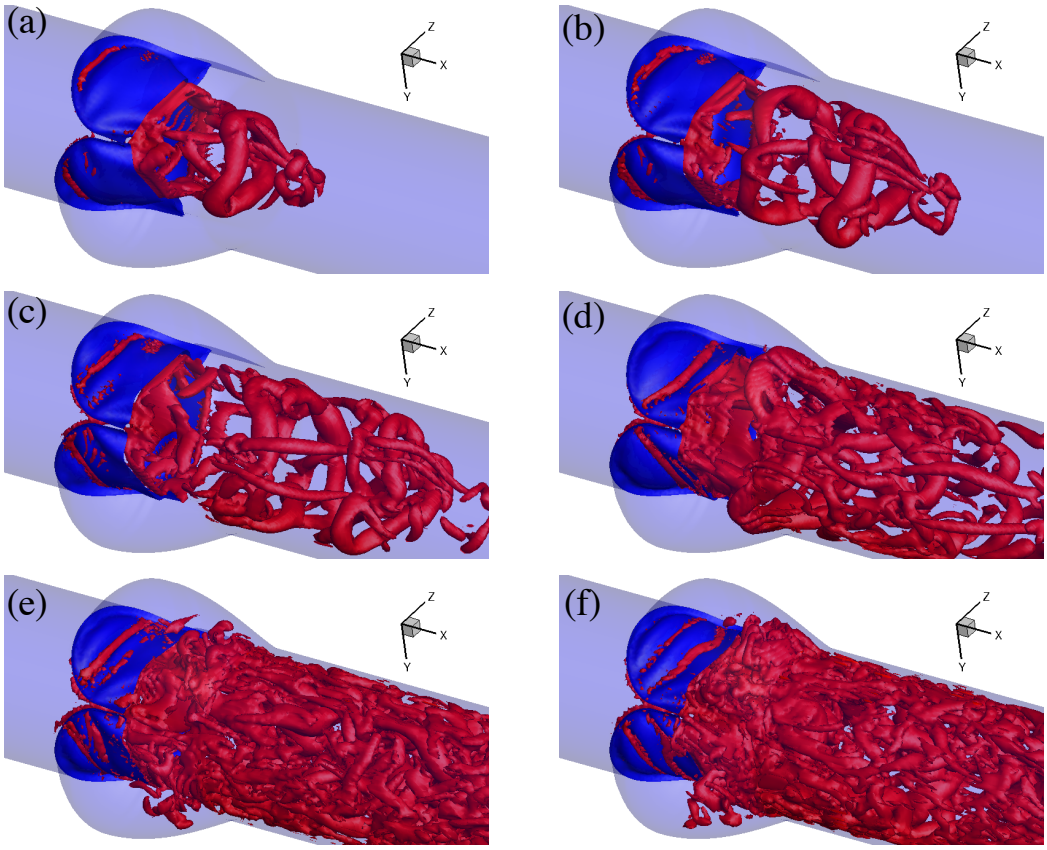

Figure 3.15: Vortices in the flow at $t = 5.2$, 6.8, 8.4, 10.8, 16.4, and 22.8 cs.

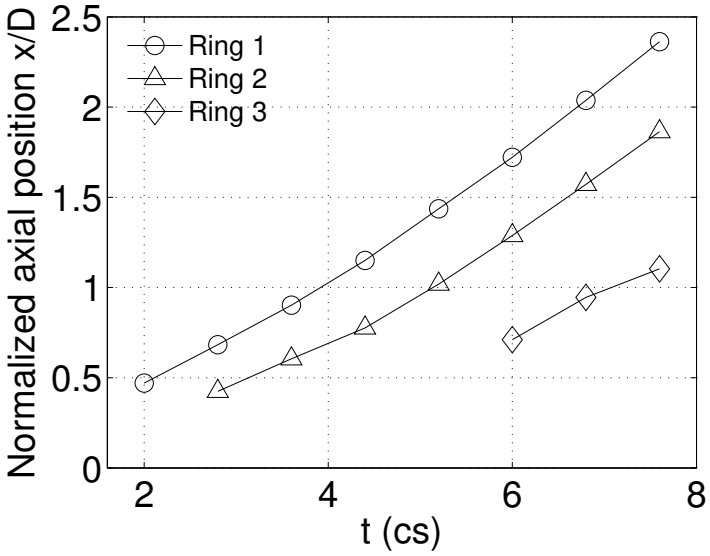

Figure 3.16: Location of the 1st and 2nd vortex rings during start of valve opening.

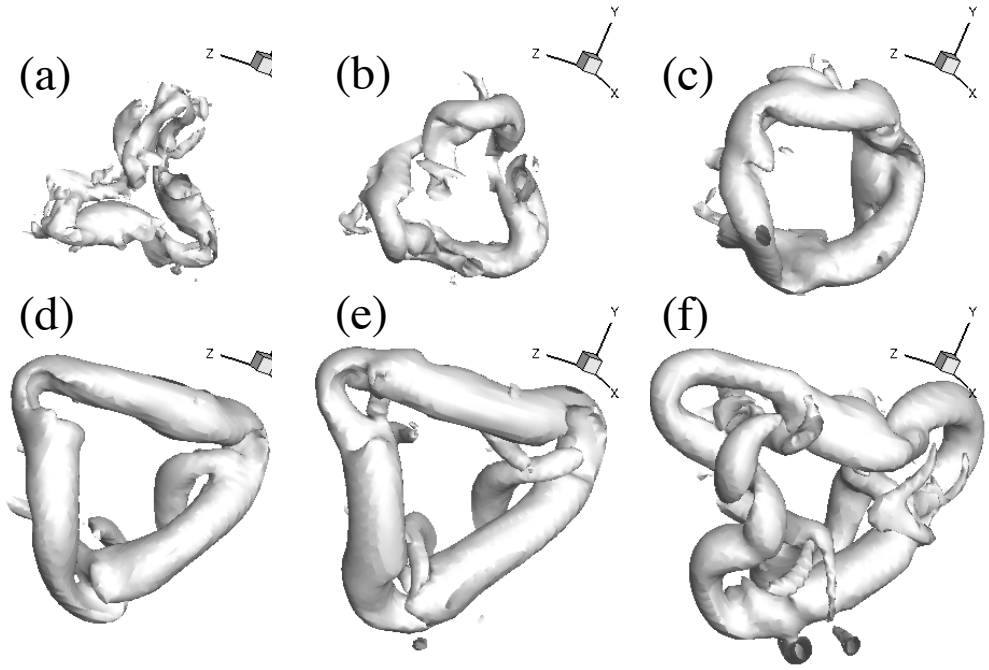

Figure 3.17: Evolution of the 2nd vortex ring at $t = 2.8$, 3.6, 4.4, 5.2, 6.0, and 7.6 cs.

3.4 Chapter conclusion

We have performed a three-dimensional study of the fluid–structure interaction of the aortic valve using a direct-forcing immersed-boundary method and parallel computing. In comparison with previous computational models, in this study both the flow and the valvular leaflets are treated with high fidelity approaches. The flow involves high-resolution simulation of a pulsatile jet, and the tissue mechanics incorporates bending and stretching behaviors of the elastic leaflets. Thus, the present model provides a tool to study details of the flow field and the valve deformation simultaneously. Different from previous studies that mainly focused on the leaflet kinematics, we have additionally studied the details of the pressure distribution over the leaflet surfaces, the momentum balance of the flow, the flapping motion of the leaflets, and the three-dimensional patterns of the vortex structures in the flow. Following are the main conclusions from this study:

1. The pressure on the ventricle side of the leaflets are highly nonuniform, and this pressure distribution causes the leaflets to open and close with their belly region leading the free-edge region. This deformation pattern affects the instantaneous nozzle shape of the valve and consequently the jet flow.

2. The total fluid force on the valve during opening is approximately equivalent to the inertial force of simultaneously accelerating three diameters of the fluid column. The drag coefficient of the valve based on the peak momentum flux is close to 0.5 during systole but its instantaneous peak can reach 1.

3. The flapping motion of the leaflets causes significant asymmetry of the jet and also unsteady oscillation of the jet.

4. The jet flow during initial opening is characterized by a sequence of vortex rings formed near the jet front and at the shear layer between the jet and the aorta wall. These vortices have distinct features in shape, and their formation is reasonably organized. When the valve is fully open and the flow rate is high, the jet contains disorganized vortices mostly aligned in the streamwise direction.

Chapter IV

Pressure distribution over the leaflets and effect of bending stiffness on fluid–structure interaction of the aortic valve

4.1 Introduction and significance of the study

Heart valves (i.e., mitral, tricuspid, aortic and pulmonic valves) consist of flexible thin leaflet structures that respond to dynamic pressure loads within a cardiac cycle to open and close in precise sequence for regulation of the blood flow direction in the heart. Normally, these thin leaflets have low flexural rigidity so that they can rapidly open and close in just a few centiseconds, thus requiring little work from the heart; on the other hand, they have high tensile strength to resist a transvalvular pressure of 80 mmHg or even greater [90, 91]. Under certain disease conditions, e.g., valvular stenosis, heart valves may thicken and stiffen, causing more difficulty for the leaflets to open. The study of the fluid–structure interaction between blood flow and heart valves is useful for diagnosis of the heart valve disease, surgical planning of the valve repair and replacement, as well as engineering design of prosthetic valves [78, 92].

There have been quite a few computational efforts in modelling the fluid–structure interaction (FSI) of heart valves that incorporate the three-dimensional characteristics of the valve geometry and blood flow. Due to the numerical challenges involved in handling the large leaflet deformation and topological change of the flow domain, many of these efforts have been focused on the development of the numerical methods or modelling approaches. The discussion of detailed flow characteristics and parameter study are far from extensive. To handle the complex geometry, the numerical methods for solving the FSI problem typically utilize non-boundary conformal grids and a form of immersed-boundary method to discretize and solve the Navier−Stokes equation [51, 19, 8, 20, 11, 21, 3, 23, 24]. The underlying flow mesh could be Cartesian [51, 20], or curvilinear [8, 11, 21], or unstructured [19, 3, 23], but in general it does not follow the movement of the leaflets. The leaflet deformation pattern has often been discussed by these simulation studies. The flexible leaflets were modelled using a finite-element approach either as elastic membranes without bending stiffness, or as plate and shell elements that permit bending loads. The latter provides a more natural deformation pattern in the leaflets. Furthermore, several studies have shown that FSI simulations provides more reasonable deformation pattern than solid-only simulations where only the tissue mechanics is solved and a uniform hemodynamic pressure distribution is assumed over the leaflet surface as the loading condition [23, 24, 81]. This conclusion suggests

that nonuniform spatial distribution should be incorporated for the pressure load when analysing the leaflet dynamics. Other than the most basic FSI process, some computational studies also included additional effects such as the surrounding tissue (e.g., aortic root) compliance [19, 93] and fiber-reinforcement in the leaflet tissue [94].

Several previous computational studies also have included discussion on characteristics of the flow field. For example, De Tullio [95] used direct numerical simulation (known as DNS) to simulate FSI of a rigid aortic bileaflet mechanical valve and to investigate the turbulence shear stress. Borazjani [11] studied the differences in the flow between a bileaflet mechanical valve and a bioprosthetic aortic valve. Gilmanov and Sotiropoulos [22] compared the vortex rings in the aorta generated by bicuspid and trileaflet aortic valves during the opening phase; they also compared the shear stress on the two types of valves. From these studies, it is clear that the flow is dominated by unsteady vortices and the morphology of the valve, e.g., bicuspid v.s. trileaflet, rigid v.s. flexible, has a significant impact on the three-dimensional (3D) flow characteristics. In a more recent simulation of ours [1], we also examined the aortic flow behavior including jet oscillation, 3D profile of the jet in cross-sections, and formation of a train of vortex rings during initial opening. In addition to the aortic valve, there have been a few studies on the flow of the other heart valves as well. For example, Seo *et al.* [96] simulated the effect of the mitral valve on flow in the left ventricle and suggested that a normal physiological mitral valve promotes the formation of a circulatory flow pattern in the ventricle.

On the experimental side, laser Doppler velocimetry (LDV) and particle imaging velocimetry (PIV) have been used in many cases to study the FSI of heart valves through in vitro set-ups [97–99]. In these studies, flow measurement was mainly focused on the region immediately around the valve exit in order to quantify the wall shear stress on the leaflets. There has also been significant interest in optimality of the vortex rings formed by the heart valves as it might be an indicator for health condition of the heart [100, 89]. More recently, PIV measurement has been done for the flow further downstream the valves to study more details of the flow behavior such as the velocity, vorticity and turbulent characteristics including the Reynolds shear stress and turbulent kinetic energy [85]. With advance of medical imaging technologies such as magnetic resonance imaging (MRI) and echocardiography, there have been quite a few studies that provide direct measurement of the flow characteristics in the body, including vortices produced by the aortic or mitral valves [86, 101–103], helical flow pattern in the aorta [104], and quantification of wall shear stress [105].

Despite these experimental and computational studies of the heart valve FSI, the hemodynamic pressure and the total force on the valve surface have not been well discussed. Studies in the past were mostly focused on shear stress caused by the turbulent blood flow due to its connection with hemolysis and platelet activation [78], and in contrast, pressure distribution on the leaflets has received much less attention despite the fact it is the primary driving mechanism for the leaflet deformation. Although the transvalvular pressure has been previously measured and studied in many cases, this pressure is not equal to the pressure on the leaflet surface, as a large portion of the transvalvular pressure is working directly on the blood for its acceleration rather than being

transmitted onto the valve; as a result, the transvalvular pressure measurement does not provide much information about the spatial distribution of the pressure on the leaflet surface. In a recent study [1], we quantified surface pressure characteristics for a thin (0.1 mm) aortic valve using 3D FSI simulation. However, the issue deserves further exploration since the pressure on the leaflets is closely associated with the leaflet dynamics as well as the flow behavior and is thus influenced by many factors. One of them is the leaflets' elastic property that directly affects their own deformation and subsequently the aortic jet. In general, there has been limited study about the effect of the bending stiffness of the leaflets and how it affects the FSI of heart valves. One exception is a recent computational study [106], in which the authors performed FSI simulations of a patient-specific aortic model with varying leaflet thickness and studied the effect of the bending rigidity on the valve's opening area, flow speed and kinetic energy. However, the pressure distribution and valve force were not discussed. Although a qualitative understanding of the stiffness effect may be straightforward (e.g., a stiffer valve requires more pressure load to open), a detailed quantitative study is necessary to better understand a few important questions: 1) What would be a proper ratio of the transvalvular pressure to the bending rigidity of the leaflets to open and close the valve? 2) As the leaflets stiffen and slow down in opening, how much tansvalvular pressure is used to accelerate the flow and how much is acting on the valve as the resistance to the flow? 3) How would the pressure distribution change on the valve as the leaflet deformation is modified due to an increase in the bending stiffness? 4) How are the spatial and temporal characteristics of the vortex rings affected in this process? Taking advantage of the fine-resolution model and parallel computation developed in our previous study, it is possible to investigate these questions by performing a series of numerical simulations.

Other than 3D computational FSI models of heart valves, simpler models with much lower computational cost also have useful applications in clinics, e.g., non-invasive measurement of the ventricle pressure. In the procedure of echocardiography, flow velocity data is used to derive the ventricle pressure based on the unsteady Bernoulli equation and the assumption that aortic valve is merely a stationary round nozzle [107, 108]. Such models are easy to use in practice but may lead to significant errors. An improved reduced-order flow model could offer more accurate information without demanding substantial computational resources. Other than clinical measurement of the ventricular pressure, the reduced-order flow model may also find applications in the multiscale modelling of the cardiovascular network in which an individual blood vessel may be treated as one-dimensional (1D) flow path [109]. To develop a reduced-order flow model, one should bear in mind that the pressure distribution over the leaflet surface is nonuniform. Furthermore, the effect of the fast leaflets movement during opening and closing on the flow should also be considered. The leaflets normally are very flexible and nearly massless, but they do not really follow the flow due to attachment to the aorta root. Therefore, their effect on the flow is not necessarily straightforward to incorporate.

In our study, we will use the same 3D FSI approach as described in our previous work [1], i.e., a Cartesian grid based sharp-interface immersed-boundary method combined with a finite-

element method, to investigate the effect of the bending stiffness of the leaflets on the FSI process of the aortic valve. We will study the leaflet deformation, pressure distribution and total force on the valve, and 3D flow field. Furthermore, we will present a new 1D flow model based on the momentum and mass conservation equations and will couple it with the 3D valve model to perform FSI simulations. We will assess the performance of the 1D flow model by comparing the leaflet deformation and flow rate with those obtained from the corresponding 3D FSI model. Limitations and the future direction of this model will be discussed at the end.

4.2 Model description and the numerical approach

4.2.1 Model set-up

A trileaflet aortic valve model similar to that in Chen and Luo [2018] is adopted and shown in Fig. 4.1. The aorta is simplified as a rigid cylindrical tube with a diameter, $D = 2.1$ cm, and a length, $L = 19$ cm. The three protruded lobes on the tube represent the aortic sinuses and their dimensions are based on physiological measurements of human aortic root [70, 71]. The geometry of the leaflets was based on a transcatheter aortic valve (TAV) [24] and was originally provided by Professor Wei Sun's lab at Georgia Institute of Technology. The thickness of the human aortic valve, h, can range from 0.26 mm to 1.3 mm for normal hearts [88] but could be thinner for transcatheter valves, e.g., 0.16 mm for a polyurethane valve [13] and 0.18 mm for a pericardial bioprosthetic valve [110]. The native aortic valve is typically asymmetric and also nonuniform in thickness [88], but we assume a symmetric model and uniform thickness for simplicity. To vary the leaflet thickness, we extrude the mesh of the leaflets along the surface normal direction in the ANSYS ICEM package to obtain eight different valve models, whose thickness is $h = 0.05$, 0.08, 0.1, 0.2, 0.3, 0.5, 0.6 and 0.8 mm, respectively. The small-thickness cases with $h \leq 0.1$ mm are included as theoretical exploration of this study. The model with $h = 0.1$ mm was constructed in our previous study [1], and we will include some of results from that study in the present work for comparison.

For spatial discretization, the rigid aortic wall is divided into 20,735 triangular elements with mesh refinement in the sinus region (approximately 0.3 mm in size). The valve tissue has a separate mesh, where each leaflet is discretized using 539 to 806 20-node hexahedron elements. These elements use quadratic basis functions and have higher-order accuracy than the 4-node tetrahedral elements that use linear basis functions. The valve is then attached to the aorta with fixed element nodes in the commissure region and also along the base, as shown in Fig. 4.1(a). A slightly open valve is used as the initial condition. A contact detection region shown in Fig. 4.1(c) is prescribed on the left-ventricle side of the surface for each leaflet, within which all the surface nodes will be checked in the simulation to determine whether or not to invoke the contact algorithm. Three nodes in Fig. 4.1(b), one located at the center of the free edge and the other two in the belly region, are traced to show kinematics of the leaflets.

Constitutive models of the valve tissue have been advanced to include fiber orientation and

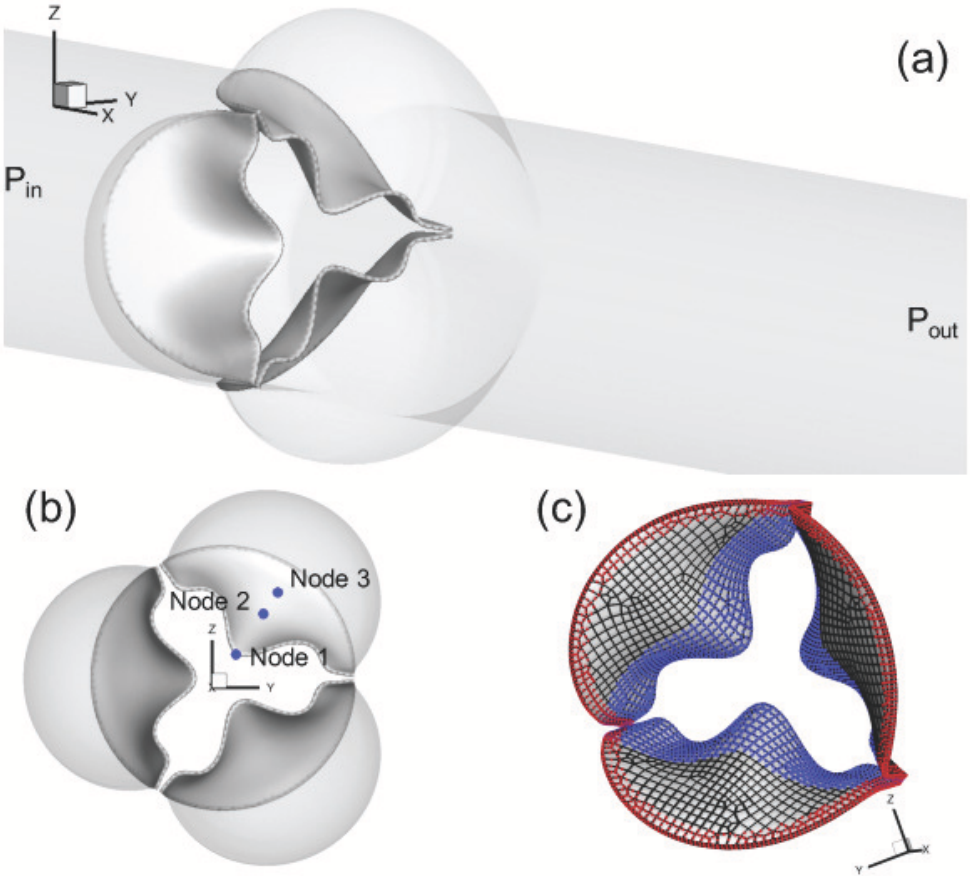

Figure 4.1: (a) Computational model of the aorta root, where the aorta tube and the aortic valve are affixed together. (b) Axial view of the valve and three sinuses, where the three markers on a leaflet are used later to plot the displacement history. (c) The fixed nodes (red markers) and contact detection region (blue markers).

anisotropic effects [111]. However, a simple isotropic neo-Hookean model should be sufficient for simulation of flexural deformation [112]. Thus, we assume that the leaflet tissue is isotropic and homogeneous, and we adopt the Saint Venant−Kirchhoff model for the hyperelastic tissue behavior in which the nonlinear strains are incorporated. The density of the leaflets is $\rho_s = 1$ g/cm^3. The mass damping coefficient, η_d, is chosen so that $\eta_d h = 1$ g/cm^2·cs^{-1} is constant for all valve models (cs or centisecond is the time unit in the present study unless otherwise specified). This structural damping is much smaller in comparison with the damping effect provided by the fluid and is added to be consistent with the previous case of $h = 0.1$ mm. For the material properties, we set Young's modulus $E = 1500$ kPa and Poisson's ratio $\nu_s = 0.4$ [3, 23].

The blood is assumed to be Newtonian and incompressible. No-slip and no-penetration boundary conditions are imposed at the aorta wall as well as the leaflet surface. The fluid domain is a $19 \times 4.4 \times 4.4$ cm^3 rectangular bounding box and is discretized by a $400 \times 130 \times 130$ nonuniform Cartesian grid. Finer resolution with $\Delta x = 0.025$ cm and $\Delta y = \Delta z = 0.034$ cm is used in the region surrounding the valve. The flow is driven by a physiological pressure drop along the aorta. The density and dynamic viscosity of the blood are $\rho = 1$ g/cm^3 and $\mu = 0.005$ Pa·s, respectively. Each cardiac cycle has a time duration of $T = 0.86$ sec, or 86 cs, which corresponds to a heart rate of 70 beats per minute. Similar to previous aortic valve models [23, 24], a transient transvalvular pressure load as shown in Fig. 4.2 is applied at the inlet of the aorta tube to drive the flow. The peak pressure during systole is $P_{max} = 2$ kPa, and the lowest pressure during diastole is -8 kPa. The exit pressure at the outlet is $P_{out} = 0$ kPa.

To solve the governing equations, we use a computational framework that was previously developed for simulating biological systems that involve large deformations [53]. In this partitioned FSI framework, the flow is solved using a Cartesian grid based direct-forcing immersed-boundary method, and the solid is solved using a nonlinear finite-element method on an unstructured Lagrangian mesh [113, 114]. Fluid–structure interaction coupling is achieved by iterating the two solvers while communicating boundary conditions at each time step until convergence. The code was verified through various case studies, including both thin-walled and general 3D body problems [53]. In the current FSI iteration, the relaxation factors are chosen as $\alpha = 0.7$ for the velocity update, $\alpha = 0.9$ for the force update and $\alpha = 1.0$ for the displacement update. To ensure numerical stability of the FSI coupling, the time step used for the flow solver is $\Delta t = 8.0 \times 10^{-3}$ cs. The time step for the structural simulation is smaller, $\Delta t = 5.0 \times 10^{-5}$ cs, so that each FSI step contains 160 substeps for the structural simulation.

For parallel computing, the rectangular box containing the flow domain is divided into 26×26 subdomains in the y- and z-directions using domain decomposition. Each subdomain only stores its own flow field data but has a full copy of the unstructured mesh of the fluid–solid interface. Since the surface mesh data for the solid is much smaller as compared with the volume data of the flow field, this decomposition strategy allows nearly a constant scaling of the total computer memory regardless the number of processor cores being used for the simulation. In the present study, a total number of 692 processor cores (676 for flow and 16 for solid) are used for the FSI

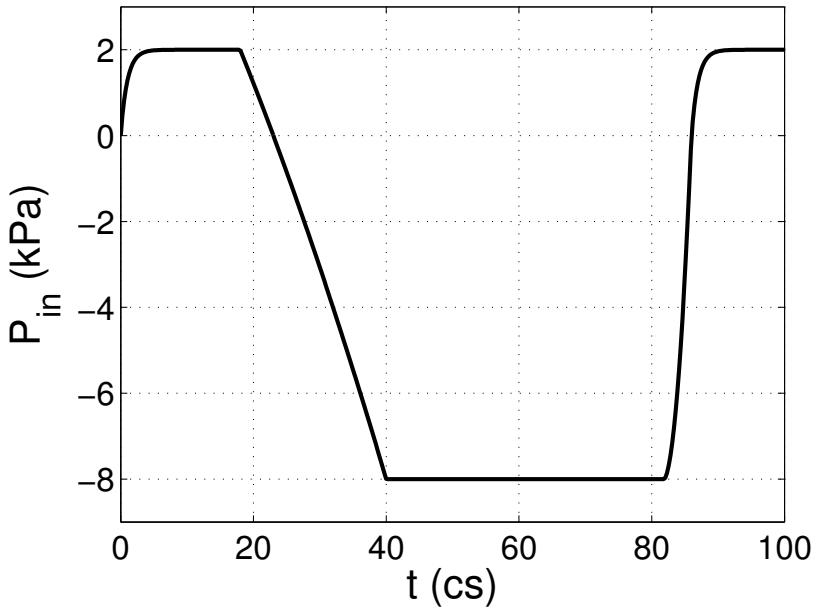

Figure 4.2: Pressure load applied at the inlet of the aorta tube in the FSI simulation, where cs denotes centisecond.

simulation, which takes about 50 hours for one cardiac cycle on Stampede 2 at the Texas Advanced Computing Center (TACC).

4.2.2 Contact model

During the closing phase and also sometimes in the opening as well, the three leaflets experience significant contact with one another. Similar to previous studies [11, 3], a penalty method is adopted here to model collision and prevent the leaflets from penetration. At each time step, the node-to-surface distance is calculated to determine whether the contact algorithm is invoked or not. That is, for each of the nodes in the contact region shown in Fig. 4.1(c), the distance is computed by projecting it onto the surface of its neighboring leaflets. The contact force in the direction of the surface normal is then calculated by

$$f_{cnt} = \begin{cases} 0, & \text{if } d - d_0 > 0 \\ -f_{ext} - k(d - d_0), & \text{otherwise} \end{cases} \tag{4.1}$$

where f_{cnt} is the nodal contact force, f_{ext} is the external force (i.e., the hydrodynamic force) on the node, d is the distance, k is the contact stiffness and d_0 is a prescribed threshold distance. Within the threshold distance, the external load f_{ext} is cancelled out and a net force of magnitude $-k(d - d_0)$ is added to prevent inter-penetration of colliding leaflets. The contact force vanishes outside of the threshold distance. Here we set $k = 1$ g/cs^2 and $d_0 = 0.08$ cm so that when the

leaflets are stopped by the contact force, the gap between them is below one cell width on the flow mesh (thus, the flow is cut off completely). We ignore the possible lubrication effect for the thin gap between two leaflets, as the exact nature of the contact mechanism should not significantly affect flow or leaflet deformation during the most of the opening and closing phases.

4.2.3 Mesh refinement study

A mesh refinement study is performed for the case of thickness $h = 0.3$ mm, where the flow domain is divided by a $500 \times 260 \times 260$ nonuniform Cartesian grid and the resolution around the leaflets is $\Delta x = 0.015$ cm and $\Delta y = \Delta z = 0.017$ cm. The time step size is $\Delta t = 4.0 \times 10^{-3}$ cs and the refined FSI simulation is run up to 36 cs for the entire systole until the valve already reaches full closure. The results are shown in Fig. 4.3 for comparison. Fig. 4.3(a) and (b) show the transient axial and radial displacements of the traced markers located on the leaflets (i.e., node 1 and node 2 in Fig. 4.1). Fig. 4.3(c) and (d) show the total axial force on the three leaflets, F_{val}, and the flow rate, respectively. From these results, we see that the valve dynamics and the total force on the valve are accurately captured by the baseline mesh, while the flow rate exhibits a less than 7% error during the peak rate. We then examined the pressure distribution on the leaflet surface using the refined mesh, as shown in Figure 4.4. The results indicate that the baseline mesh is sufficient in capturing the nonuniform pressure on the surface of the leaflets. We have also examined the vortex structures from the refined-mesh simulation, and they are consistent with the baseline-mesh results. Based on these comparisons, the baseline flow mesh is deemed satisfactory for the current study. We also did a separate mesh refinement study for the finite-element model of the valve, in which the number of hex-20 elements is increased by approximately 5 times in the refined mesh. Comparison of the leaflet dynamics shows that the results are in excellent agreement with the baseline valve mesh.

4.3 Results and discussions for 3D simulation

4.3.1 Leaflet deformation

Fig. 4.5 shows the valve deformation sequence for thickness $h = 0.2$ to 0.8 mm. From these plots, it is evident that the bending rigidity has a significant effect on the dynamic shape of the valve and the extent of valve opening. For the thinner leaflets with $h = 0.2$ and 0.3 mm, the valve opens up quickly, first bulging out from its belly and then moves its free edges to their full extent. During the closing phase, the leaflets start contract inward, again first from the belly area and then the free edges follow up. Because the mid-edge moves ahead of rest of the free edge, each leaflet forms an inward fold at the mid-edge. During diastole, the leaflets are stretched inward with clear extension by the negative ventricle pressure. For $h = 0.1$ mm, the deformation pattern is similar to that is described here, but the leaflets are so flexible in that case that they also form a travelling wave from the base to the free edge, causing the leaflets to flap like immersed flags after the valve is fully opened [1]. The two thinnest cases, $h = 0.05$ and 0.08 mm, have similar flapping motion to the case of $h = 0.1$ mm (see a supplementary figure for leaflet deformation in these cases). Such

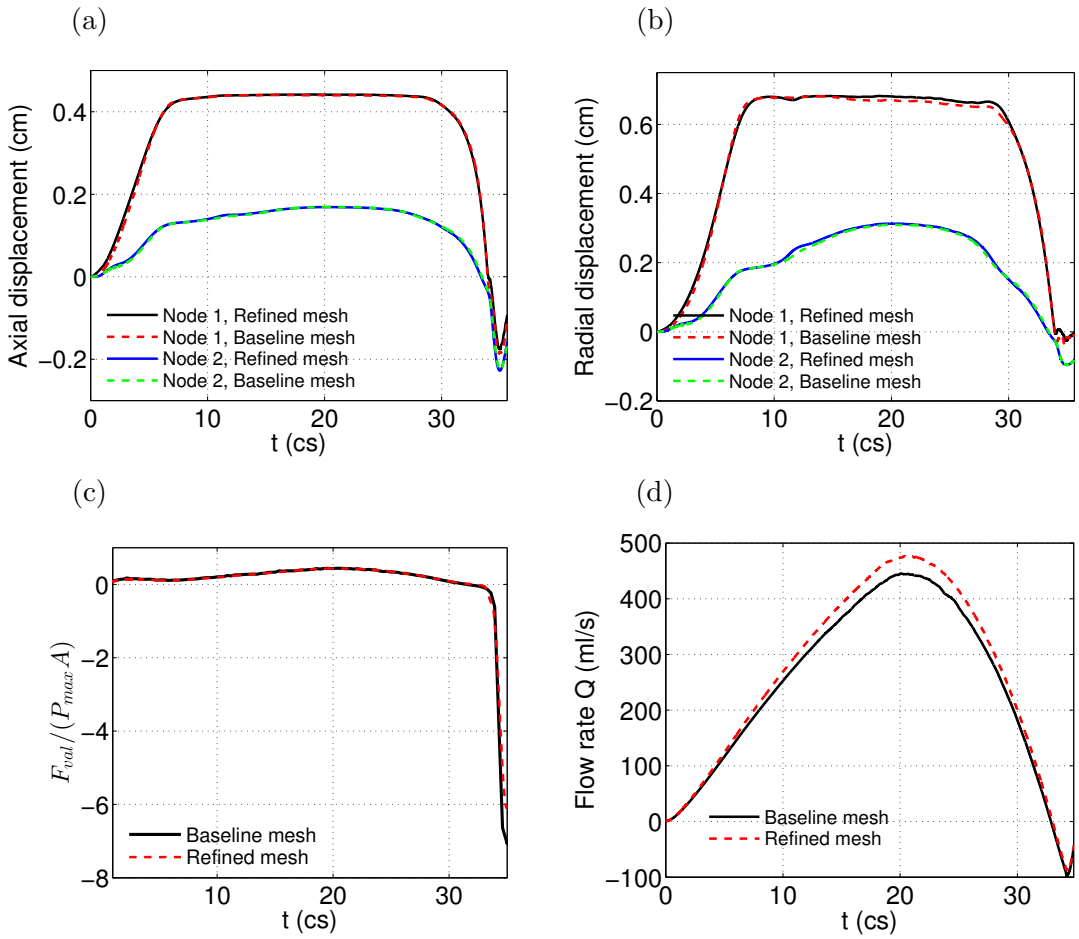

Figure 4.3: Comparison between the baseline flow mesh and refined flow mesh for (a) axial and (b) radial displacements of the nodes 1 and 2 on the leaflet, (c) the total force on the valve normalized by the pressure load, and (d) the flow rate during entire systole.

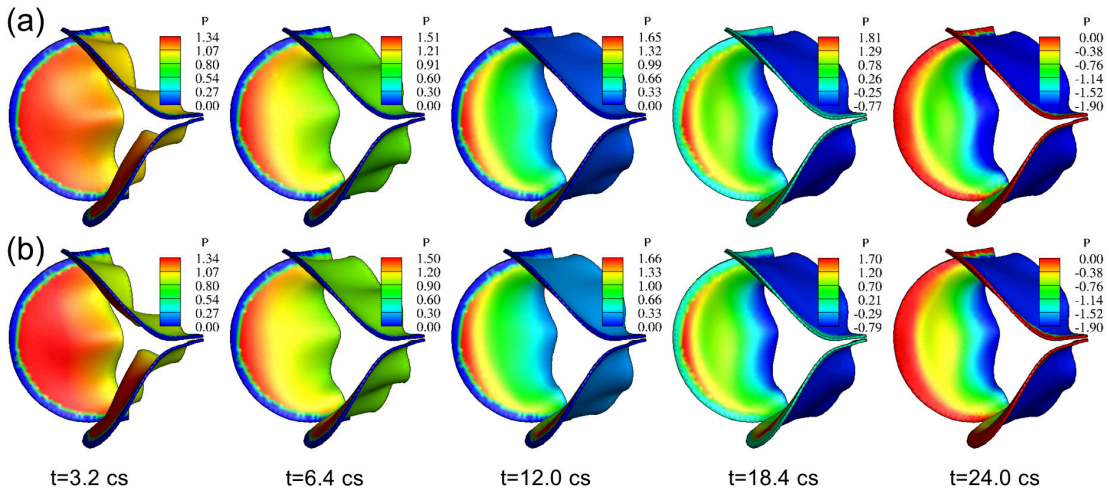

Figure 4.4: Pressure distribution (unit: kPa) on the valve from the 3D FSI simulation for $h = 0.3$ mm; (a) baseline mesh, and (b) refined mesh.

flapping motion was confirmed in our previous study [1] using mesh and time step refinement.

For the intermediate thickness of $h = 0.5$ and 0.6 mm, the valve opening is clearly slowed down. The leaflet bellies do not bulge out very much, and the free edges are not fully extended out, thus creating a smaller opening area for the flow to go through. During the closing phase, the free edges move in first, and then the belly regions follow. The curvature of the mid edges is not as high as that of the thinner leaflets. For the thickest case of $h = 0.8$ mm, the valve opening is substantially reduced, and the leaflet displacement is less than halfway through.

For all the cases in Fig. 4.5, the free edges of the leaflets form an opening with a three-lobe propeller configuration that is consistent with observations in several previous experimental studies of aortic valve [115–117] as well as FSI simulations [9, 3, 24, 118, 1]. This particular shape is caused by the inward fold at the mid edge of the leaflets that has higher stiffness and has to snap through in order to extend out to form an opposite curvature. For the thinner cases of $h = 0.2$ and 0.3 mm, snap through is easier and can happen later at full opening of the valve. For thicker cases of $h = 0.5$ and 0.6 mm, snap through becomes more difficult. For $h = 0.8$ mm, snap through becomes impossible with the given ventricle pressure load, and therefore, the propeller configuration is maintained during the whole systole in this case. For $h = 0.1$ mm and less, the valve opens from the middle due to its low bending rigidity and thus, the valve forms a three-lobe star shape instead during initial opening phase (see a supplementary figure for leaflet deformation in these cases).

4.3.2 Flow rate and valve opening area

Figure 4.6(a,b) presents the transient flow rate, $Q = \int u \mathrm{d}A$, and geometric orifice area (GOA) from an entire cardiac cycle for all five different cases. The GOA is calculated by finding the projected

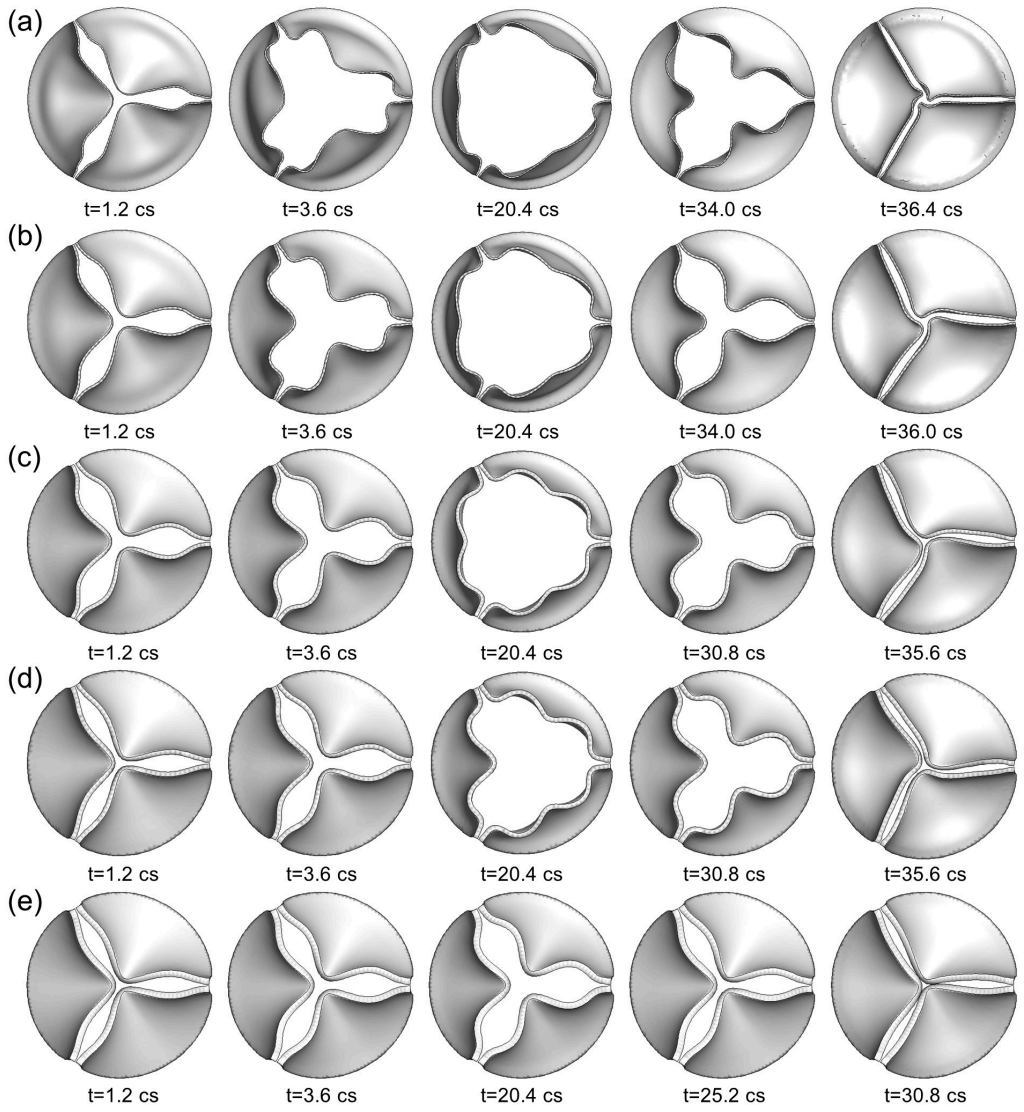

Figure 4.5: Deformation of the valve in 3D FSI simulation for thickness (a) $h = 0.2$ mm, (b) 0.3 mm, (c) 0.5 mm, (d) 0.6 mm, and (e) 0.8 mm.

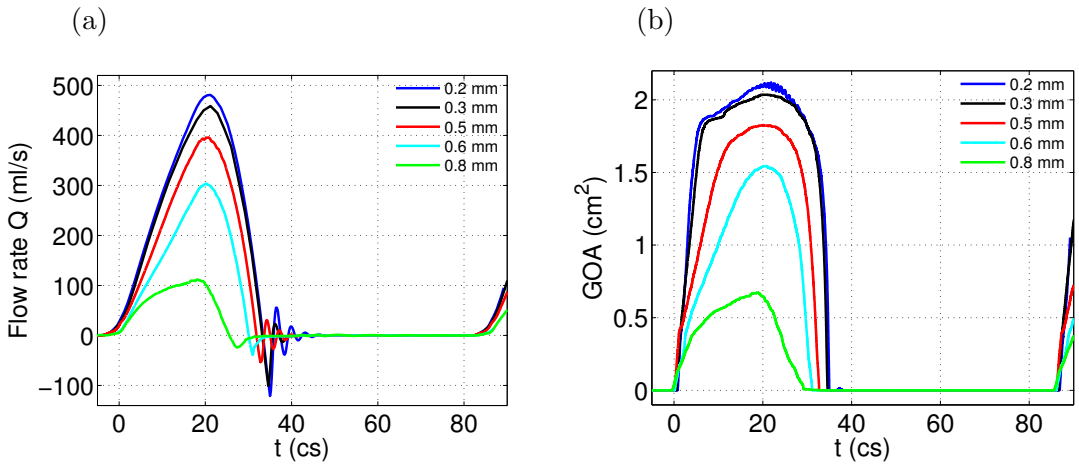

Figure 4.6: Volumetric flow rate, Q, and geometric orifice area (GOA) in a full cardiac cycle for $h = 0.2$ to 0.8 mm.

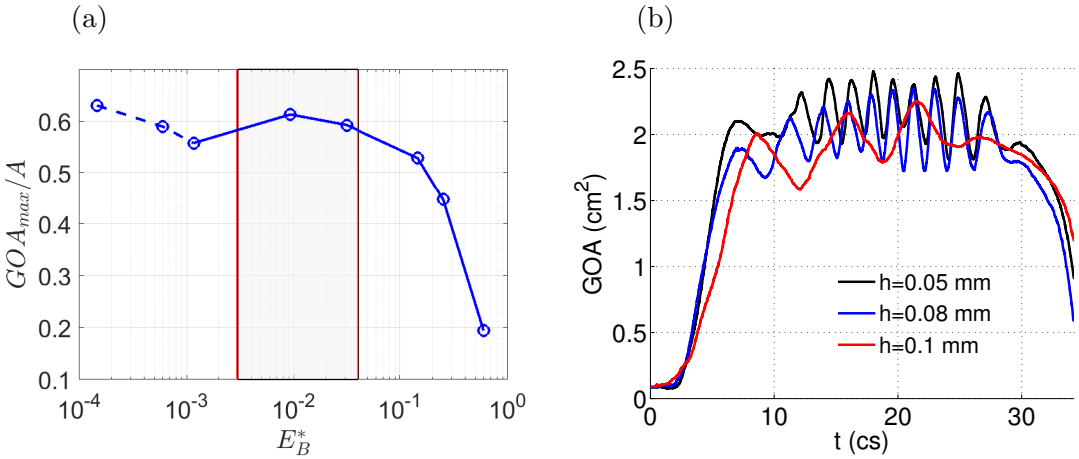

Figure 4.7: (a) Effect of the normalized bending rigidity on the normalized maximum GOA. The case of $h = 0.1$ mm from Chen and Luo [2018] has been included. The dashed part indicates that the leaflets undergo significant flapping oscillations. The shaded area represents approximately the optimal region. (b) Transient GOA for the three thinnest valve cases showing large oscillations.

area of the valve on a plane perpendicular to the aorta axis. The effect of the bending rigidity is evident from this figure. As the thickness increases, the flow rate and the opening area during the systole drop significantly, especially for the cases of $h = 0.6$ and 0.8 mm. Note that from the specified pressure waveform in Fig. 4.2, the driving ventricle pressure at the inlet starts to drop at $t = 18$ cs. However, the forward flow continues to accelerate under the positive pressure load until around $t = 20$ cs when both the flow and GOA reach a peak. The peak flow rate is 483, 459, 396, 304 and 112 ml/s for the case of $h = 0.2$, 0.3, 0.5, 0.6 and 0.8 mm, respectively.

During the closing phase, the thinner valves have a faster moving speed as seen from the time derivative of the GOA. However, the thicker valves close earlier from both the flow rate and GOA plots, which is due to the low flow rate and smaller GOA at the opening phase in these cases. A negative dip in the flow rate is observed for all the cases, indicating a temporary flow reversal that takes place along with closing motion of the leaflets. By integrating the transient flow rate in time, we obtain the stroke volume for each valve model, which is 98.5, 99.6, 75.3, 52.0 and 20.3 ml per beat for thickness of $h = 0.2$, 0.3, 0.5, 0.6 and 0.8 mm, respectively. The corresponding cardiac output (or averaged flow rate) is 6.9, 7.0, 5.3, 3.6 and 1.4 l/min. The peak flow rate, stroke volume and cardiac out in the cases of $h = 0.2$, 0.3 and 0.5 mm are all within the physiological range for normal adult aortic valves [68, 77], while in the cases of 0.6 and 0.8 mm these variables are below the normal range due to reduced valve opening.

The effective orifice area (EOA) represents a measurement of the valve's characteristic resistance and is often used clinically for the quantification of valve stenosis severity [78, 79]. The EOA in our calculation follows the previous definition [78], $\mathrm{EOA}(\mathrm{cm}^2) = Q_{rms}/(51.6\sqrt{\Delta p})$, where Q_{rms} is the root mean square systolic flow rate in ml/s and Δp is the mean systolic pressure drop in mmHg. We used the time period when the pressure difference $P_{in} - P_{out}$ is positive to compute the average as Δp. According to this formula, the EOA is 1.81, 1.72, 1.46, 1.11 and 0.49 cm^2 for thickness of $h = 0.2$, 0.3, 0.5, 0.6 and 0.8 mm, respectively. For thinner leaflets (e.g., $h = 0.2$ and 0.3 mm), the EOAs are in agreement with earlier reported results for normal adult valves [78, 24]. As the thickness increases, the leaflets behave like calcified or stenotic valves and the EOA drops significantly. Regurgitation is the leakage of blood backward through the aortic valve to the left ventricle during diastole. In current simulation, the regurgitation volume in all the cases is less than 1.3 ml per cycle and is also in good agreement with previous reports [78, 24]. The performance index of the valve, defined as EOA/A and used in clinical contexts as a criterion to evaluate severity of valve stenosis, is 0.53 for $h = 0.2$ mm but drops to only 0.14 for $h = 0.8$ mm. This index is listed later in Tab. 4.1 along with the normalized valve force for all the cases.

In general, the valve opening-closing process can be divided into four stages: (I) rapid valve opening, (II) maintenance of maximum excursion, (III) slow valve closing, and (IV) fast valve closing [80, 68]. For the cases of $h = 0.2$ and 0.3 mm, these four stages can be clearly observed from the GOA plot. In these cases, the rapid valve opening takes approximately 5 to 6 cs, the maximum excursion approximately 19 cs, the slow closing approximately 7 cs, and the fast closing approximately 3 to 4 cs. These time scales agree well with the previously reported data for healthy

aortic valves [78, 24]. As the thickness further increases from 0.5 to 0.8 mm, the maximum excursion stage (represented by a plateau in the transient GOA history) vanishes gradually.

In the three cases of $h = 0.1$ mm and less, the time scales of the four stages are similar to those in the cases of $h = 0.2$ and 0.3 mm. However, in those cases, the thin leaflets exhibit a flag-like flapping motion after the valve is fully opened [1], which leads to significant oscillations in the GOA (Fig. 4.7b). The magnitude and frequency of flapping in those cases are different and may have to do with the bending stiffness, tension in the leaflets, as well as the curvature of the leaflet surface once the valve is opened. For thicker valves, only the case of $h = 0.2$ mm has such high-frequency oscillations in the GOA and the magnitude is very small as seen in Fig. 4.6(b); in the other cases, no evident flapping motion is observed. As a result of the leaflet flapping, the jet in the cases of $h \leq 0.1$ mm also becomes more oscillatory. For $h = 0.05$, 0.08 and 0.1 mm, the flow rate is 504, 479, 447 ml/s, respectively, and the EOA is 1.89, 1.79 and 1.67 cm^2, respectively. Note that the case of 0.1 mm, whose $E_B^* = 0.0012$, has reduced flow rate, EOA and GOA when compared with the case of 0.2 mm (Fig. 4.7a and Tab. 4.1). Thus, the changes of valve opening and flow rate are not monotonic as the thickness is reduced from 0.2 mm.

We further present the effect of the bending rigidity on the valve opening in terms of non-dimensional parameters. Fig. 4.7 shows the normalized maximum GOA by the cross-sectional area of the aorta tube, A, against the bending rigidity normalized by the overall pressure gradient $\Delta P/L$, i.e., $E_B^* = E_B/(\Delta P R^4/L)$, where $\Delta P = P_{max} - P_{out}$ is the pressure drop during valve opening, $E_B = Eh^3/12(1-\nu^2)$ is the flexural rigidity, L is the tube length, and R is the radius of the aorta tube. From Fig. 4.7(a), there exists an optimal range of normalized bending rigidity of the valve that is roughly between E_B^* =0.003 and 0.04. It is worth noting that most of previous studies of normal aortic valves, including native and prosthetic, fall within this optimal range [88, 119, 24]. Above the range, the valve may become too stiff with the valve opening reduced. In reality the heart would have to do extra work through physiological control mechanisms in the body to maintain sufficient cardiac output; in that case, the normalized bending rigidity E_B^* is effectively reduced due to higher pressure load. On the other hand, below this range the leaflets are too flexible and may form travelling waves and flapping motions, which is typically seen in immersed flags [120] and could cause the valve performance to drop as in the case of $h = 0.1$ mm. In the design of transcatheter valves, the leaflet thickness is sometimes reduced to accommodate the valve to miniaturized catheters [121]. The present finding of the hydrodynamic consequence for very thin leaflets may serve as a design consideration for such valves. Even if sufficient valve opening could still be achieved (as in the cases of $h = 0.05$ and 0.08 mm), frequent oscillation of the leaflets due to flapping may become a concern for the cyclic flexural fatigue of bioprosthetic valves [122].

The definition of the dimensionless parameter E_B^* involves the use of the average pressure gradient along the tube during valve opening, where the tube length has been included in the scaling. To confirm that the results are relatively independent of the tube length and the pressure gradient is a reasonable reference for scaling, we have doubled the tube length, with the tube segments upstream and downstream the valve both lengthened and the driving pressure at the inlet

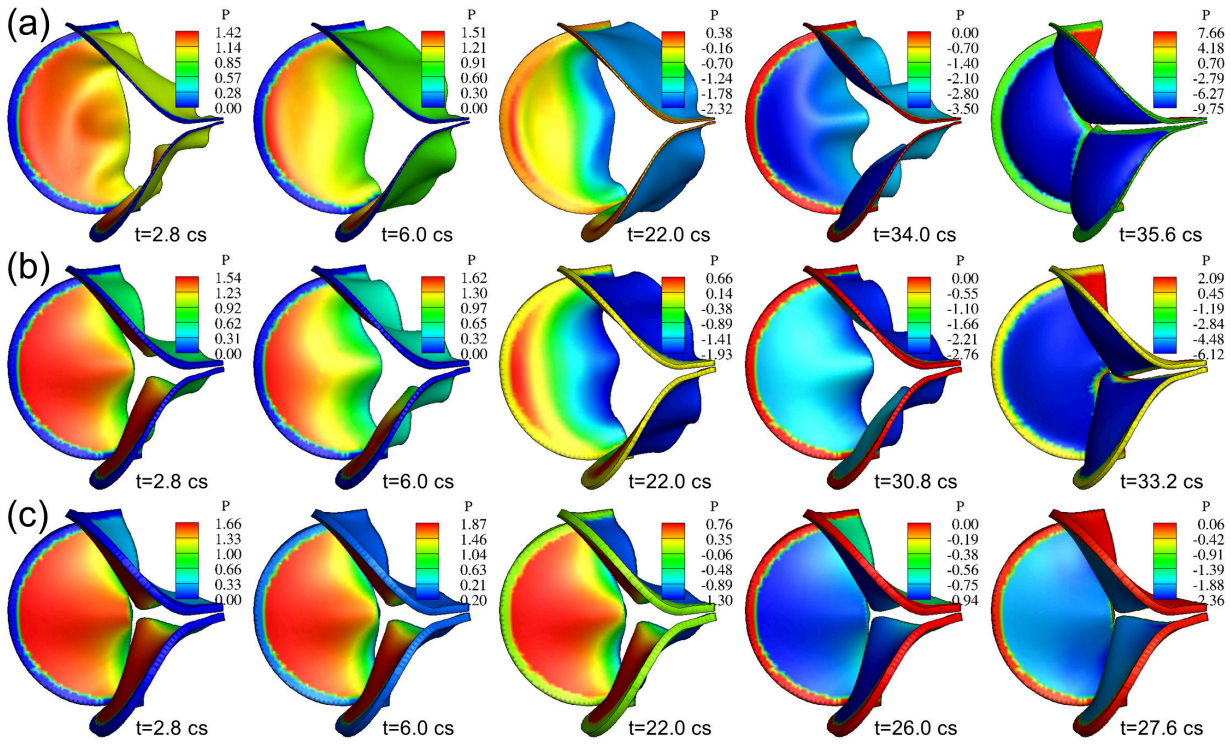

Figure 4.8: Pressure distribution (unit: kPa) on the valve in 3D FSI simulation for thickness (a) $h = 0.2$ mm, (b) 0.5 mm, and (c) 0.8 mm. Note that the color range is different in each frame and colors at the fixed edges are not meaningful.

also doubled. The transient GOA for $h = 0.3$ mm from this additional FSI simulation is provided as a supplementary figure. The result is consistent with that from the baseline simulation, despite small differences are observed (such differences are expected since the pressure drop should not be strictly proportional to the tube length due to the presence of the valve).

4.3.3 Pressure distribution

Pressure distribution on the valve surface is a result of two-way interaction between the flow and the leaflets. Thus, not only the instantaneous shape of the valve but also the motion of the leaflets affect the magnitude and spatial characteristics of the surface pressure. Fig. 4.8 shows the pressure on the ventricle side of the valve for $h = 0.2$, 0.5 and 0.8 mm at selected systolic moments. It can be seen that at most of these time frames, the surface pressure varies from the base to the free edge of the leaflets. Overall, the pressure drops along the axial direction from the fixed base to the free edge since the valve forms a converging nozzle while opening and the fluid velocity is highest at the exit of the valve. However, the effect of the leaflet movement can be seen as well. For example, comparing the frame of $h = 0.2$ mm and $t = 2.8$ cs and the frame of $h = 0.5$ mm and $t = 6.0$ cs, the amount of valve opening is similar in these two frames, but the pressure is significantly different.

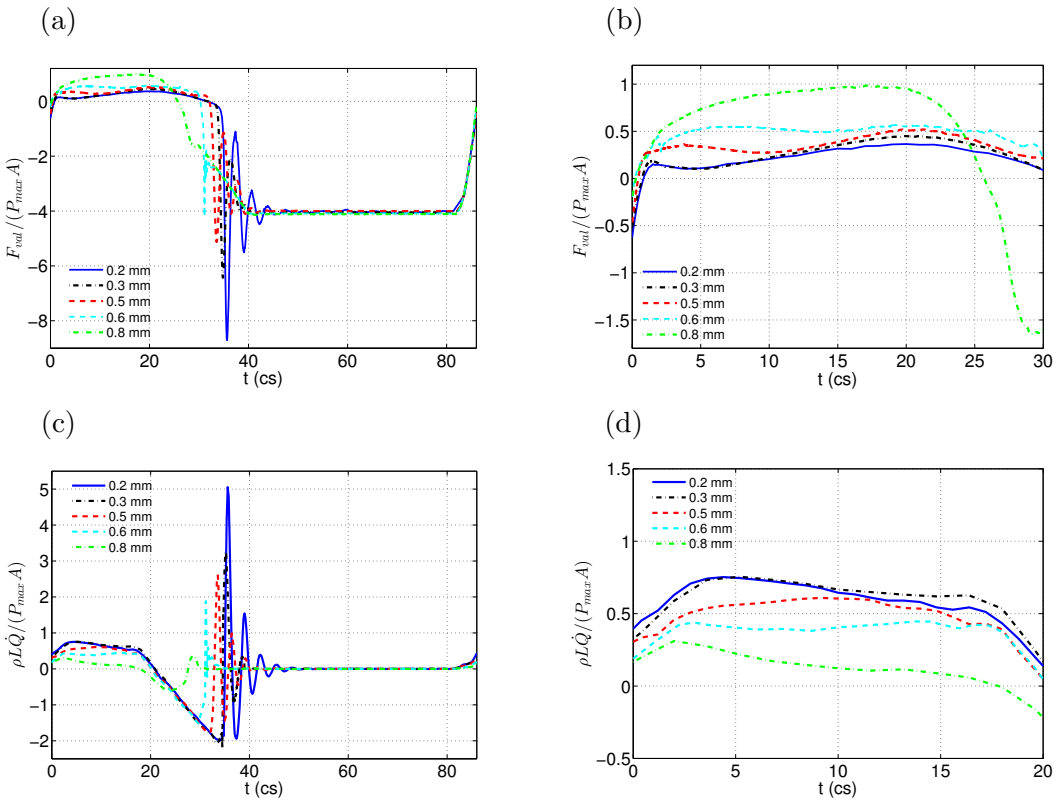

Figure 4.9: History of normalized (a) F_{val} and (c) $\rho L\dot{Q}$ for each valve in a full cycle. (b,d) Zoom-in view of (a,b) for systolic acceleration.

In particular, the pressure near the base of the valve in the former frame has lower magnitude than the pressure at the same region in the latter frame; furthermore, the pressure in the former frame has less variation and is more uniform from the base to the free edge. This result has to do with the fast valve opening in the case of $h = 0.2$ mm, where the thin leaflets yield to the accelerating flow more quickly and thus incur less impact from the flow.

For the thickest valve of $h = 0.8$ mm, the characteristics of pressure distribution do not change substantially in time during opening due to slow motion of the leaflets, even though the overall magnitude of the pressure still varies temporally according to the pressure waveform specified at the inlet. In all the cases, the pressure on the ventricle side of the valve becomes nearly uniform when the valve is fully closed as seen in the last column in Fig. 4.8. In addition, the pressure on the aortic side of the valve is always nearly uniform, though its magnitude depends on the overall shape and movement of the valve.

4.3.4 Momentum balance and total force on the valve

In order to better understand the total hemodynamic force on the valve, or valve's resistance to the flow, we consider the interior of the aortic wall as a control volume and analyse the momentum

balance of the flow. The momentum conservation of the flow in the axial direction is

$$\frac{\partial}{\partial t}\int \rho u \,\mathrm{d}V + \int \rho u^2 \,\mathrm{d}A = (P_{in} - P_{out})A - F_{val} - F_{sin} - F_{tub}, \tag{4.1}$$

where u is the axial velocity, $A = \pi D^2/4$ is the area of the cross-section, P_{in} and P_{out} are the inlet and outlet pressure, respectively, F_{val} is the total axial hemodynamic force on the leaflet surfaces (both aortic and ventricle sides included) or the valve resistance, F_{sin} is the axial force on the sinus section of the wall, and F_{tub} is the axial force on the remaining tube wall. Introducing the flow rate, Eq. (4.1) can be written as

$$(P_{in} - P_{out})A = \rho L\dot{Q} + \int_{\text{out}} \rho u^2 \,\mathrm{d}A - \int_{\text{in}} \rho u^2 \,\mathrm{d}A + F_{val} + F_{sin} + F_{tub}, \tag{4.2}$$

where $\dot{Q}$ is the time derivative of the flow rate and L is the length of the flow domain. This equation represents how the transvalvular pressure load is split among different factors that include the inertial acceleration of the fluid column in the aorta, momentum fluxes, and the forces on the valve, sinuses, and tube wall. As shown in our previous study [1], the momentum fluxes at the inlet and outlet nearly cancel each other; furthermore, F_{sin} and F_{tub} are small. Thus, the overall pressure load is mostly shared between flow acceleration and the force on the valve, i.e., $(P_{in} - P_{out})A \approx \rho L\dot{Q} + F_{val}$, at any time moment.

The transient valve force F_{val} and fluid inertial force $\rho L\dot{Q}$ normalized by $P_{max}A$ are both plotted in Fig. 4.9 for an entire cycle. The most distinct feature in the valve force as shown in Fig. 4.9(a) is the negative spike that immediately follows full closure of the valve for all the cases except $h = 0.8$ mm. This force is generated when the reversal flow is initiated during the closing phase but is quickly shut off. Due to its momentum, the reversal flow impinges on the aortic side of the valve, leading to a "water hammer" effect and a large resultant force. If the valve is thin and more elastic, the leaflets may be stretched toward the left ventricle by the reversal flow and then bounce back, thus causing several following-up spikes of lower magnitude. An animation of the valve force for $h = 0.3$ mm is provided as supplementary material. As the valve thickness is increased, the magnitude of the force spike becomes lower, and the spike has completely gone for $h = 0.8$ mm. From the inertial force shown in Fig. 4.9(b), we see that there are corresponding spikes in $\rho L\dot{Q}$ that are similar in magnitude but opposite in sign to the valve force.

From the zoom-in plots in Fig. 4.9(c,d), it can be seen that for thin leaflets of $h = 0.2$ and 0.3 mm, the valve force is much smaller as compared with the fluid inertial force during the acceleration phase of $t = 0$ to 20 cs. For the thick leaflets of $h = 0.6$ and 0.8 mm, the valve force becomes greater than the fluid inertial force. The effect is further quantified in Tab. 4.1 using $F_{val}/(P_{max}A)$ and $F_{val}/(\rho D\dot{Q})$ averaged from the systole. To compute the average, only the time period of positive F_{val} is considered, and the same for $\dot{Q}$. The former represents percentage of the valve resistance in the total transvalvular pressure load, and the latter represents the equivalent length of the fluid column, in terms of tube diameter, being accelerated. At $h = 0.2$ mm, the valve resistance is 22% of the transvalvular pressure and is equivalent to accelerating $3.4D$ of fluid column; at $h = 0.8$ mm,

h (mm)	E_B^*	$\frac{\text{EOA}}{A}$	$\frac{I_{max}}{P_{max}A}$	$\frac{F_{val}}{P_{max}A}$	$\frac{F_{val}}{\rho D \dot{Q}_{avg}}$	C_D
0.05	1.5E-4	0.55	1.09	15%	2.2	0.28
0.08	6.0E-4	0.52	1.01	18%	2.7	0.36
0.1	1.2E-3	0.49	1.00	24%	3.9	0.48
0.2	9.3E-3	0.53	1.10	22%	3.4	0.40
0.3	3.1E-2	0.51	1.10	28%	3.8	0.50
0.5	1.5E-1	0.43	0.75	35%	6.2	0.94
0.6	2.5E-1	0.33	0.42	48%	10.3	2.28
0.8	6.0E-1	0.14	0.07	80%	40.5	22.80

Table 4.1: Normalized bending rigidity E_B^*, performance index EOA$/A$, average maximum momentum flux I_{max}, average valve force F_{val}, and average drag coefficient C_D for each case. The case of $h = 0.1$ mm is from Chen and Luo [2018].

the valve resistance reaches 80% of the transvalvular pressure and is equivalent to accelerating $40.5D$ of fluid column, which would add significant load to the cardiovascular network.

We may use the peak momentum flux at the inlet, $I_{max} = \max \int \rho u^2 \, \mathrm{d}A$ to define the drag coefficient of the valve, so that $C_D = 2F_{val}/I_{max}$. For thinner valves of $h = 0.2$ and 0.3 mm, I_{max} is 1.52 N. For thicker valves, I_{max} drops quickly and is 1.03, 0.58 and 0.10 N for $h = 0.5$, 0.6 and 0.8 mm, respectively. The corresponding drag coefficient is listed in Tab. 4.1. For $h = 0.2$ mm, C_D is 0.40, and for $h = 0.8$ mm, C_D reaches a high level of 22.8. In all the resistance measures listed in the table, the case of $h = 0.1$ mm has higher resistance than the case of $h = 0.2$ mm due to its flapping motion in the leaflets. The two thinnest cases, $h = 0.05$ and 0.08 mm, have lower drag resistance measures as compared to other cases such as $h = 0.1$ and 0.2 mm because these extremely thin leaflets have low stretching stiffness in addition to low bending stiffness, thus having a larger opening area.

4.3.5 Flow field

Fig. 4.10 shows a sequence of the vortex structures, plotted using the Q-criteria, for selected cases with thickness $h = 0.2$, 0.5 and 0.8 mm. For comparison, we also included the case of $h = 0.1$ mm from our earlier work [1]. It can be seen that the bending rigidity of the valve has a significant effect on the vortex development. For the case of $h = 0.1$ mm, the flow field is featured by a leading vortex ring first emitting from the central hole of the leaflets and also the second and the third vortex rings that follow the first ring. The first ring is more circular. The second vortex ring initially has a similar 3-lobe star shape to the shape of the initial valve exit, then the ring evolves to a triangular shape before final breakdown (see Fig. 17 in Chen and Luo [2018] for more detail). The cases of $h = 0.05$ and 0.08 mm have similar vortex patterns.

For all the other five thicker cases considered here, the jet initially forms three separate vortex rings, which originate from the three gaps between any two adjacent leaflets. This behaviour is

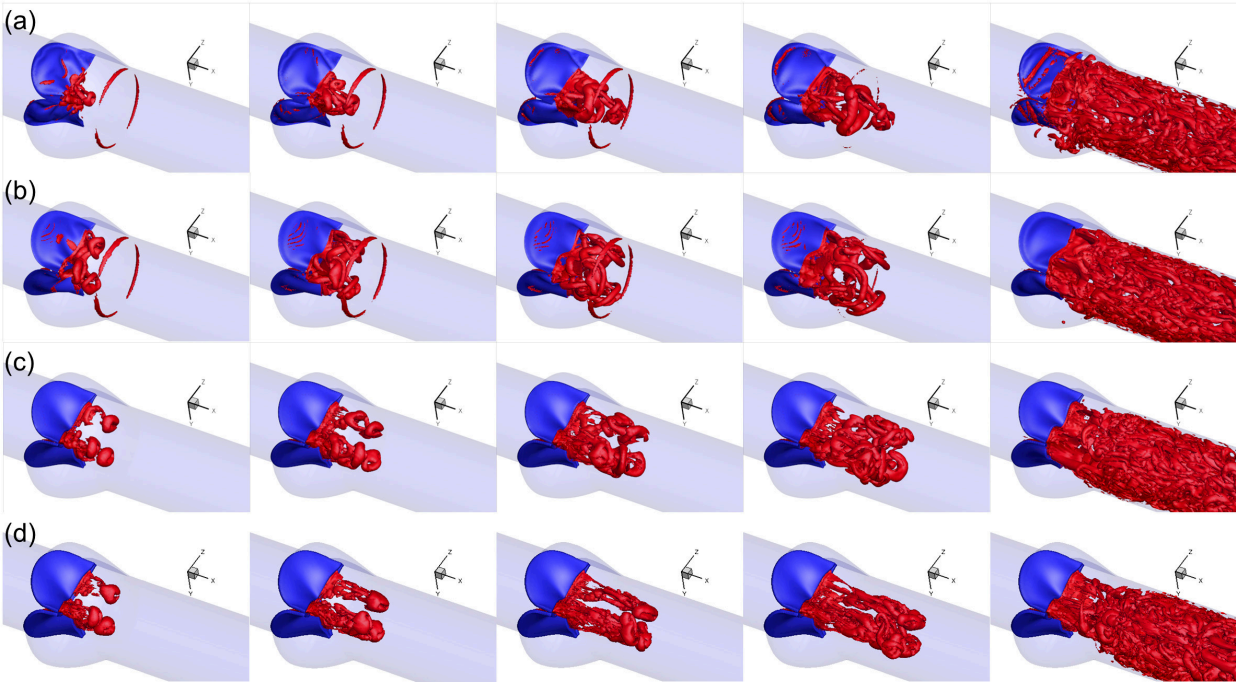

Figure 4.10: Vortex development during valve opening for (a) $h = 0.1$, (b) 0.2, (c) 0.5, and (d) 0.8 mm at $t = 2.8$, 3.6, 4.4, 5.2, and 16.4 cs.

associated with the propeller shape of valve opening and is caused by the slow opening at the mid-edge of the leaflets where the leaflets fold inward and the effective stiffness is much higher than the rest of the area. In the case of $h = 0.2$ mm, the three vortex rings are interconnected through vortex filaments shedding from the free edge. As the valve continues to open, the axial velocity increases in the central core region, causing the vortex rings to deform. The vortex filaments earlier connecting the three vortex rings penetrate the rings, causing more vortex-vortex interactions, and they travel downstream along with the rings ($t = 3.6$ and 4.4 cs) untill later breakdown after $t = 6$ cs.

In the cases of $h = 0.5$ and 0.8 mm, the three leading vortex rings are more rounded in shape and have less deformation in the first 4 cs. Also, these vortex rings are more independent of each other without evident interconnecting vortex filaments. As the thickness increases, the jet is more confined near the central core region and has a higher velocity due to limited opening area. For instance, the axial velocity at $t = 2$ cs is 0.98 m/s for $h = 0.3$ mm, while it is 1.47 m/s for $h = 0.6$ mm at the same moment, in which case the vortex rings are advected downstream more quickly. In all cases, the vortices become less identifiable later after 16 cs as the flow rate continues to rise. An animation of the vortex structures for $h = 0.3$ mm is provided as supplementary material.

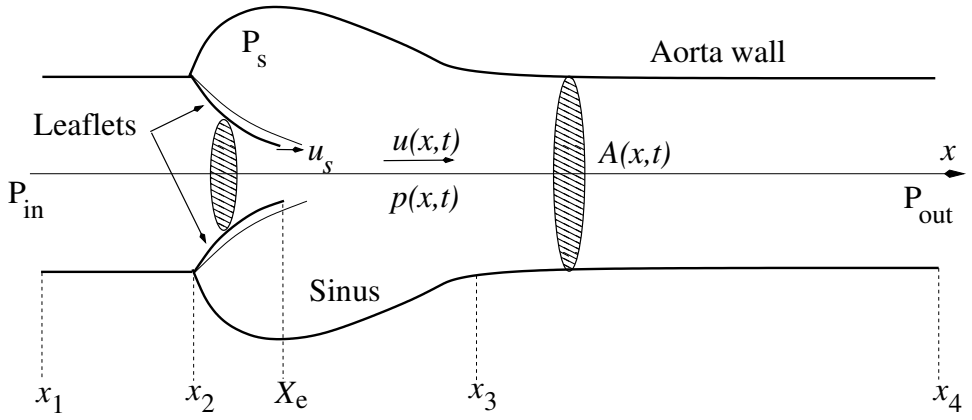

Figure 4.11: Schematic of the axisymmetric domain for the 1D flow model.

4.4 One-dimensional flow model and FSI simulation

4.4.1 Model description

Having better understood the pressure distribution on the valve surface, we proceed to develop a 1D transient flow model to represent the hemodynamics through the aortic valve. We will combine this flow model with the 3D finite-element model of the valve to repeat the FSI simulation. Such a hybrid 1D/3D FSI model could be useful when high-fidelity representation of the tissue mechanics is needed, e.g., for surgical planning, but simplification of the flow is desired for efficient simulations. To construct the 1D flow model, we make a few drastic simplifying assumptions to the flow and its geometrical domain. First, we assume that the flow is described only by the axial velocity component, $u(x,t)$, and the pressure has the form of $p(x,t)$. Second, the entire domain is axisymmetric, including the aorta tube and the sinus region, and the trileaflet valve is treated as a nozzle with circular cross-sections but a flexible wall. The schematic of the domain is shown in Fig. 4.11 for illustration. The cross-section area of the domain at any location is denoted by $A(x,t)$ and is calculated from the actual 3D geometry of the domain shown in Fig. 4.1. At a cross-section that intersects the three leaflets, A is computed by finding the area within an x-plane enclosed by the ventricle side of the leaflet surface. Since the free edges of the actual leaflets are not located in the same cross-section before the valve is fully open, an x-plane may cut through the free edges and thus the enclosed area is not well defined. In that case, the shape of the free edges upstream the x-plane is projected onto the plane, and the total area A is the combination of this projected area and the area formed by the intersection between the x-plane and the rest of the valve. This treatment allows the effective cross section of the jet to be taken into account and A to be continuous from the base to the exit of the valve in the 1D model. The valve exit is denoted by a Lagrangian point, X_e, in Fig. 4.11. The mass conservation equation of the flow can be written as

$$\frac{\partial A}{\partial t} + \frac{\partial Au}{\partial x} - u_s \frac{\partial A}{\partial x} = 0, \tag{4.1}$$

where $u_s(x)$ is the axial velocity of the leaflets. This equation takes into account the fact that the leaflets are moving in the radial direction as well as in the axial direction, both types of displacement having an effect on the local mass conservation. We calculate the axial velocity u_s at each x-location by comparing and computing shift of A in the axial direction from two consecutive time steps.

Following the 1D flow model developed by Cancelli and Pedley [1985] for a collapsible tube with variable cross-sectional area and later modified by Anderson *et al.* [2013] to simulate the airflow in the human upper airway, we simplify the x-momentum equation of the flow in the entire domain to the following form,

$$\begin{aligned} \rho\frac{\partial u}{\partial t} + \rho u\frac{\partial u}{\partial x} &= -\frac{\partial p}{\partial x} + \tau\frac{s}{A} \\ \tau &= \tau_{fric} + \tau_{\chi}, \end{aligned} \tag{4.2}$$

where τ is shear stress including the frictional loss, τ_{fric}, and additional pressure loss in a diverging channel, τ_{χ}, and s is the perimeter of the cross-section. The friction loss, τ_{fric}, is estimated based on the fully developed laminar flow in a tube with constant cross-section, i.e., $\tau_{fric} = -2\mu(\,s/A)\,u$; and τ_{χ} is usually associated with loss of kinetic energy due to flow separation and is calculated according to

$$\tau_{\chi} = \frac{A}{s}(\,1-\chi)\,\rho u\frac{\partial u}{\partial x}, \tag{4.3}$$

where $0 \le \chi \le 1$ is a constant representing the amount of pressure recovery in the diverging channel. If $\chi = 1$, then $\tau_{\chi} = 0$ and the pressure can be fully recovered (except for the loss due to τ_{fric}, which is small for the short domain in the present study); and if $\chi = 0$, then no pressure is recovered. In the present study, we tested this constant empirically through several simulations. It was found that the following choices work well: in the opening phase, $\chi = 0.6$ is set in the region between the valve exit X_e and the sinus-tubular junction downstream (i.e., the interval $[X_e, x_3]$ in Fig. 4.11), while $\chi = 1.0$ elsewhere; after the flow is reversed during the closing phase, $\chi = 0$ in the region of $[x_2, X_e]$, $\chi = 0.8$ in $[X_e, x_3]$, and $\chi = 1.0$ elsewhere.

In the FSI simulation, the fluid pressure from the 1D flow model is applied axisymmetrically on the left-ventricle side of the 3D valve so that the surface pressure on this side only depends on x and t. On the aortic side, the surface pressure is nearly uniform and is close to the pressure near the valve exit, as we learned from the 3D FSI simulation. Thus, we assume a uniform sinus pressure, P_s, on the aortic side of the valve and assume that it is related to the pressure at X_e, P_e, by the inertial displacement of the fluid in the entire sinus region,

$$P_s - P_e = -c\frac{\rho\ddot{V}}{R}, \tag{4.4}$$

where V is the instantaneous volume of the sinus region calculated from the actual domain, $\ddot{V}$ is the second-order time derivative of V, R is the tube radius, and c is an arbitrary constant and is set equal to $c = 0.2$ through several trials.

The 1D flow is driven by the pressure at the inlet, $p = P_{in}$ at x_1, which is time dependent and is the same as in the 3D FSI model. At the outlet x_4, $p = P_{out} = 0$. Eq. (4.1) and Eq. (4.2) form a

boundary value problem that can be solved straightforwardly using a shooting method. Specifically, at a time step where the inlet pressure P_{in} is specified and A is first calculated from the current valve configuration, we assume an inlet velocity $u(x_1)$ and solve Eq. (4.1) using a finite-difference method for $u(x)$ within the entire domain. From this temporary solution of $u(x)$, we then solve Eq. (4.2) for temporary pressure $p(x)$, again using a finite-difference method. The pressure solution at the outlet, $p(x_4)$, is compared with the outlet pressure condition $p = P_{out}$ for convergence check of this time step. The Newton–Raphson method is adopted for the iterative solution process at each time step. That is, after temporary solutions of $u(x)$ and $p(x)$ are obtained, $u(x_1)$ is perturbed and the solution process for Eqns. (4.1) and (4.2) is repeated for a different output of $p(x_4)$. Then, the numerical derivative $\mathrm{d}p(x_4)/\mathrm{d}u(x_1)$ is calculated and used in the Newton's iteration until $p(x_4)$ matches P_{out}. Finally, a similar FSI iteration procedure as in the full 3D simulation is employed here for the hybrid FSI model.

4.4.2 Results from the hybrid FSI simulation

Fig. 4.12 shows the deformation sequence of the aortic valve at $h = 0.2$ to 0.8 mm from FSI simulation using the 1D flow model. In general, the characteristic deformation pattern agrees well with that from the 3D FSI simulation. This result is in contrast with the solid-only simulation with a uniform pressure assumption, which leads to overly large displacement and outward bending of the leaflets [23, 22, 1]. For thinner leaflets of $h = 0.2$ and 0.3 mm, the 1D flow model produces correct deformation sequence where the belly of the valve bulges out first and is followed by the free edge opening, and in the other cases, the free edges move ahead of the rest of the valve. Furthermore, the 3-lobe propeller shape of the free edges is preserved for all cases during both the opening and closing phases. The major discrepancy with the 3D result is that for thicker leaflets of $h = 0.6$ and 0.8 mm, the opening of the valve is smaller than the opening from the 3D FSI result. A detailed comparison is further shown in Fig. 4.13 for history of the GOA during the entire systole. For thinner leaflets of $h = 0.2$ and 0.3 mm, the 1D flow model also produces fairly accurate dynamics of the leaflets, i.e., fast opening, maximum excursion, slow closing, and then fast closing of the valve, even though the maximum valve opening in the hybrid simulation is slightly smaller than that in the 3D simulation. For thicker leaflets of $h = 0.6$ and 0.8 mm, there is significant discrepancy between the two models, and the hybrid simulation produces slower opening and closing than the 3D simulation; however, the overall characteristics are still in qualitative agreement.

The hybrid FSI simulation is stopped once the valve becomes fully closed. Thus, the diastole phase is not included in the simulation. In practice, the 1D flow model can simply be replaced by a lumped-parameter piston-like model to continue the simulation after valve closure and to capture the subsequent 'water hammer' effect.

Pressure distribution on the valve surface from the hybrid FSI simulation is shown in Fig. 4.14 for all five cases. Comparing the pressure contours with those in the corresponding 3D simulation as shown in Fig. 4.8, we see that the overall nonuniform characteristics are captured by the 1D

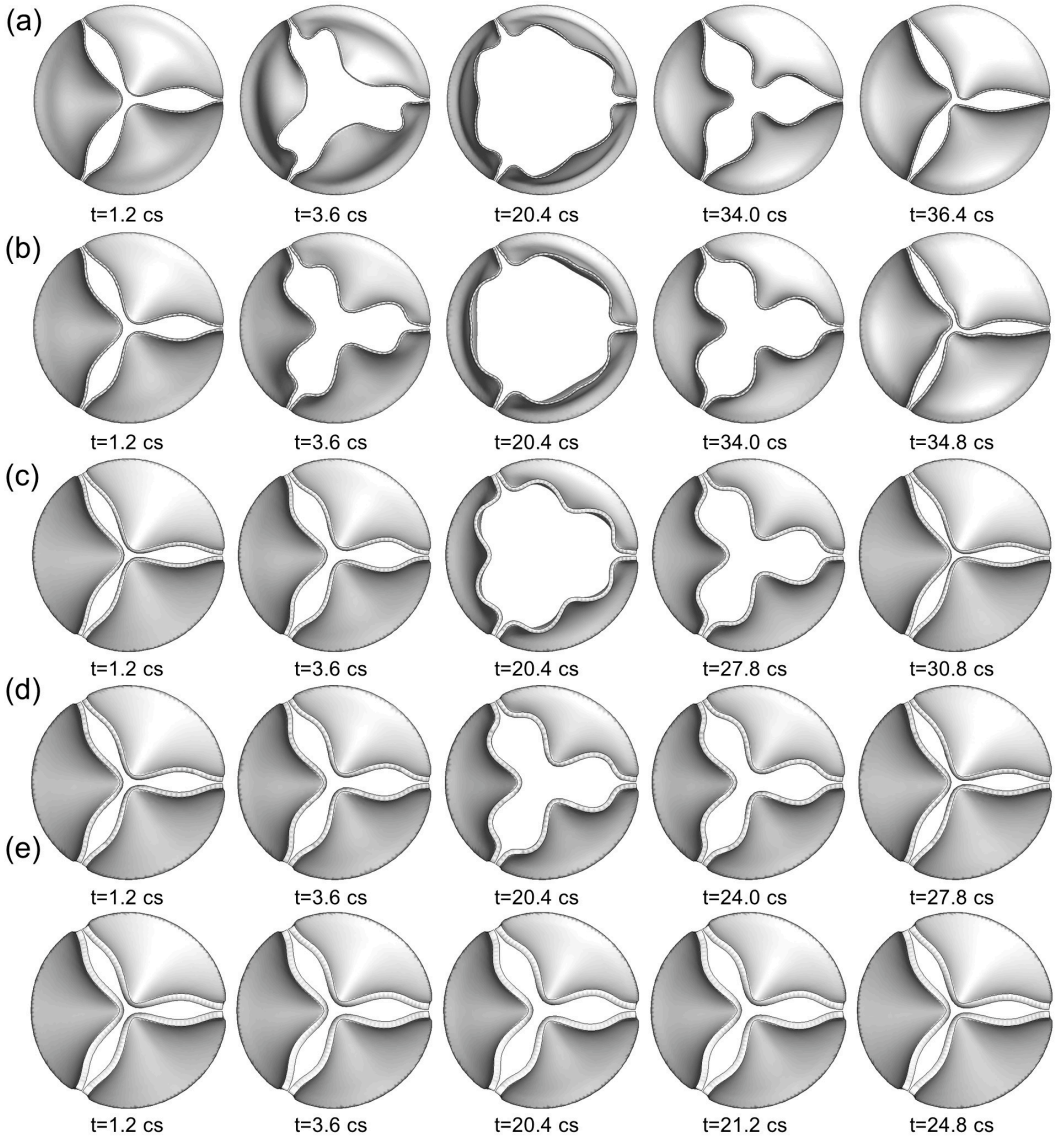

Figure 4.12: Sequence of valve deformation from hybrid 1D/3D FSI simulation for thickness (a) $h = 0.2$ mm, (b) 0.3 mm, (c) 0.5 mm, (d) 0.6 mm, and (e) 0.8 mm.

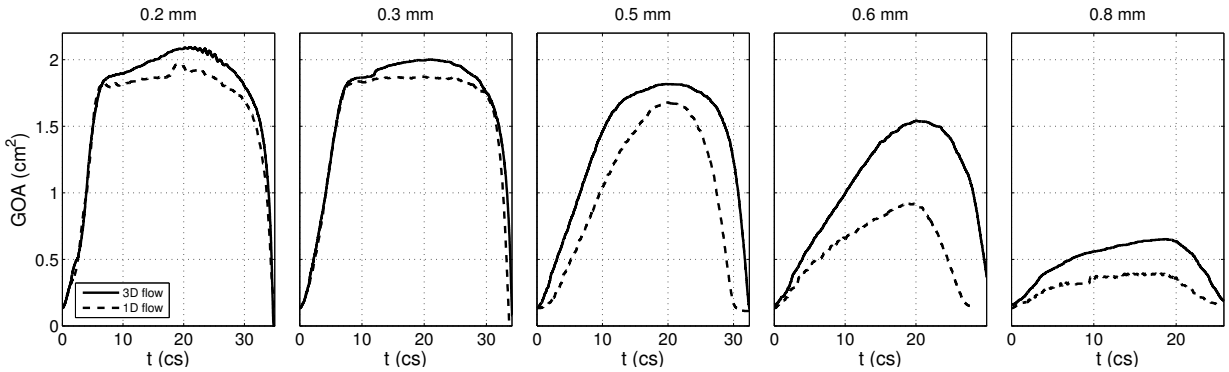

Figure 4.13: Comparison of the GOA history between the 1D flow and 3D flow in the FSI simulation.

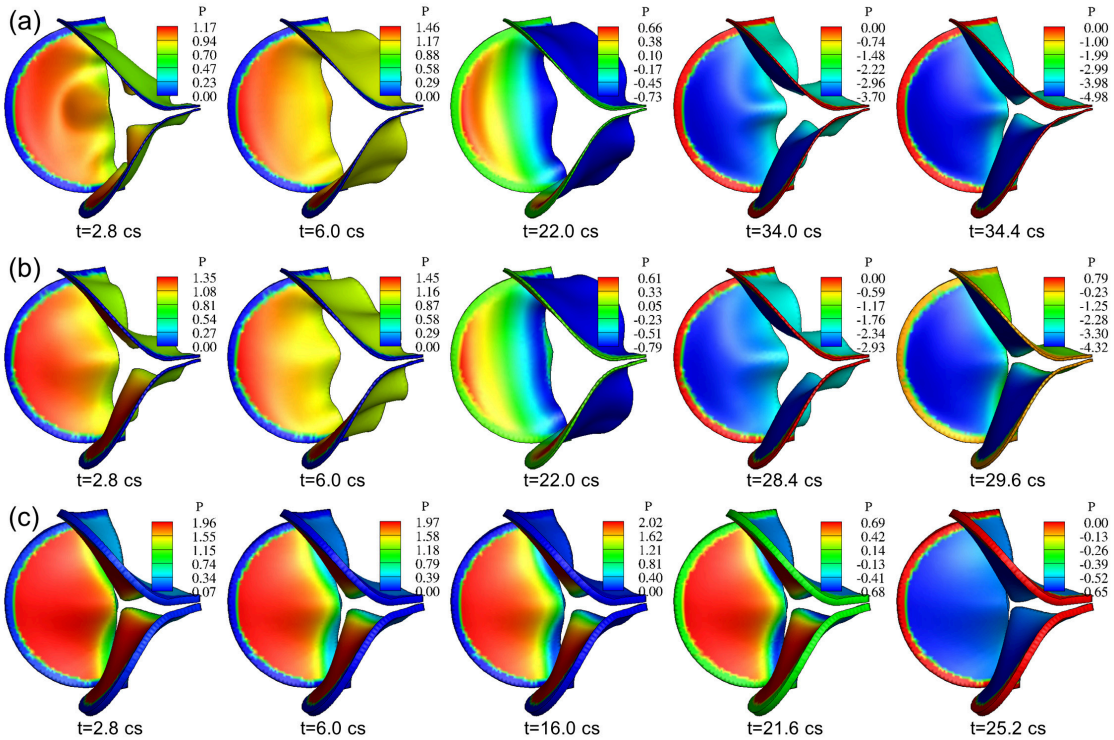

Figure 4.14: Pressure distribution (unit: kPa) on the valve in hybrid FSI simulation for thickness (a) $h = 0.2$ mm, (b) 0.5 mm, and (c) 0.8 mm.

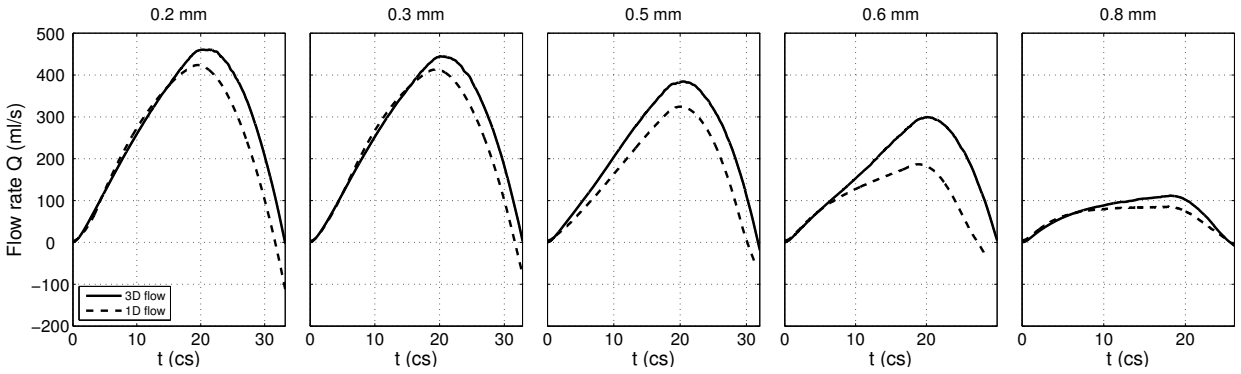

Figure 4.15: Comparison of the flow rate between the 1D flow and 3D flow in the FSI simulation.

flow model: the pressure on the ventricle side drops from the base to the free edge during opening phase, and during closure the pressure on the ventricle side becomes more uniform in the cases $h = 0.2$ to 0.6 mm. Furthermore, the pressure on the aortic side varies in time in response to the valve opening in a correct fashion as in the 3D simulation. Even though the specific magnitude of the pressure may be somewhat different from that in the 3D simulation, in general the pressure difference between two sides of the valve is still reasonably close to that in the 3D simulation. Further inspection shows that in the cases of $h = 0.6$ and 0.8 mm, the pressure on the ventricle side near the mid point of the free edges is lower than that in the 3D simulation. This discrepancy has led to reduced opening of the valve by the 1D flow in these two cases.

Fig. 4.15 shows the history of the flow rate from the hybrid FSI simulation. Again, the major characteristics of the flow are captured reasonably well. For thinner valves of $h = 0.2$ and 0.3 mm, the flow rate matches the 3D result quite well, including rise and drop of the flow rate in the systole and even the temporary negative flow rate right before the full closure. For thicker valves $h = 0.5$ and 0.6 mm, there is significant discrepancy between the two models, and the 1D flow model produces a lower flow rate that is associated with reduced valve opening in the simulation.

Fig. 4.16 shows a comparison of the leaflet kinematics between the hybrid and full 3D FSI simulations. In the figure, the radial position of the three selected points on the valve is traced out during systole. These points are marked in Fig. 4.1: node 1 on the free edge, node 2 at the belly and node 3 near the base. It can be seen that the hybrid FSI results generally agree with the full 3D FSI results, indicating that the transient deformation is, overall, consistent between the two simulations. However, there are also notable differences. For example, in the case of $h = 0.2$ mm, the free edge of leaflets first bends more outward in the hybrid FSI simulation before returning to the same position as in 3D FSI. Since the leaflets are very flexible in this thin case, the valve deformation is more sensitive to the errors in the pressure prediction. In the cases of $h = 0.6$ and 0.8 mm, the hybrid simulation clearly under-predicts the valve deformation, and this result has to do with the simplified interpolation of 1D pressure onto the leaflet surface as discussed earlier.

In summary, the present 1D flow model produces reasonable results when combined with the

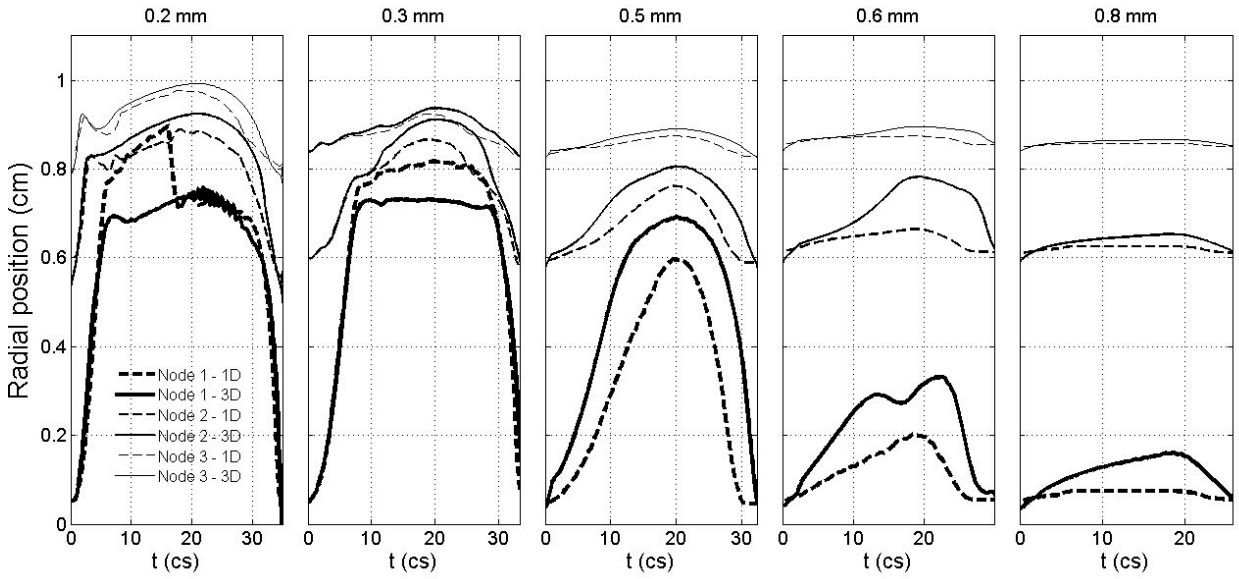

Figure 4.16: Comparison of the radial position for the three marked points on the valve between the 1D and 3D flow models in the FSI simulation.

3D tissue model, and it requires drastically less computation as compared with the 3D flow model. In some of the cases, e.g., valves with high bending rigidity, this 1D flow model could be further improved by considering interpolating the fluid pressure onto the leaflet surface in an empirical fashion that better matches the pressure contours from the 3D simulation. Finally, there are several limitations in the present study. We have ignored the anisotropic effects of the tissue and greatly simplified the geometry of the aortic root as well as the inlet/outlet flow conditions. Our models are also limited to a symmetric configuration of the valve, and its possible application to asymmetric and abnormal valves (e.g., bicuspid valves) will need further investigation.

4.5 Chapter conclusion

In this work, we presented a numerical study of the transient and nonuniform pressure distribution on the aortic valve as well as the effect of the bending stiffness on the fluid–structure interaction of the valve. To complement the full 3D FSI simulation, we developed a new one-dimensional flow model and coupled it with the 3D valve model to perform hybrid FSI simulation. By varying the thickness of the leaflets and thus the bending rigidity of the valve, we simulated both the normal flexible valve and the stiffened valve with high rigidity. The simulation results show that once the flexural rigidity normalized by the transvalvular pressure gradient exceeds $E_B^* = 0.2$, the bending stiffness of the valve has a major detrimental effect on the valve function. As the bending stiffness is further increased beyond this value, the valve opening is largely reduced and the valve resistance becomes substantially higher. On the other hand, as shown previously, if the bending

stiffness is overly low (e.g., E_B^* =1.2E-3), the leaflets could have flapping oscillations and may lead to undesirable effects on the valve mechanics. Therefore, optimal bending stiffness between these extreme cases should be desirable for best valve performance. This result might provide a useful guideline for the design of prosthetic valves. Our 1D flow model and hybrid FSI simulation show that the new reduced-order flow model is able to capture the pulsatile aortic flow and the pressure distribution on the valve reasonably well. This model may be useful for situations where costly 3D flow simulations are not desirable, e.g., design optimization of the prosthetic valves.

Chapter V

A reduced-order flow model for fluid–structure interaction simulation of vocal fold vibration

5.1 Introduction and significance of the study

Vocal fold virbation during phonation involves aerodynamic interaction of a pulsatile glottal jet and the soft vocal fold tissue stretched between the laryngeal cartilages. The unsteady airflow is responsible for activating and sustaining the vocal fold vibration, and the oscillation pattern of the vocal fold in turn modulates the airflow. This dynamic interaction determines many basic characteristics of voice [25]. An advanced computational model of the fluid–structure interaction (FSI) for the vocal fold will find useful applications in the understanding, diagnosis, and treatment of voice disorders. Many FSI models have been developed in the past with various levels of complexity. In terms of spatial setup, these models can be generally categorized depending on whether the airflow and the tissue respectively assume a zero-, one-, two-, or three-dimensional configuration. Within each configuration, the models can still differ significantly from one another depending on how to treat various details such as the structural tissue layers, elastic properties of the tissue, and anatomical features of the larynx. In early stages, discrete or lumped-mass systems were created to understand onset of phonation [28–30]. In these models, the vocal fold was simplified to two or more mass blocks connected to elastic springs, and the Bernoulli equation or other simplified flow equations were used to model the airflow. Despite its simplicity, such models can capture self-induced oscillations and have been used extensively to understand basic effects of governing parameters, e.g., the subglottal pressure and tissue stiffness, and also to investigate characteristic behavior of normal and abnormal phonation, e.g., chaotic vibration and vocal fold polyps [29]. With the development of high-performance computing hardware and software, continuum-mechanics based computational models have been increasingly used for vocal fold modeling. For example, both two-dimensional (2D) and 3D finite-element models have been developed to simulate the vocal fold deformation [31–35]. More recently, high-resolution simulations have been more frequently used in the FSI modeling of the vocal fold. Examples of previous works include Thomson et al. [36], Luo et al. [37, 38], Zheng et al. [39]. Using the intensive, typically parallelized computations, many of these studies have reported the unsteady vortex structures in the airflow and their interaction with the vocal fold.

As modern medical imaging technology is being advanced, internal anatomy of human bodies

can be viewed with unprecedented details using noninvasive approaches such as computed tomography (CT) and magnetic resonance imaging (MRI). Such imaging modalities may provide 3D geometry of the larynx as well as the interior structure of the tissues [40, 41, 2]. The images generated by these techniques could be used to develop more sophisticated computational models that have much realistic representation of the laryngeal anatomy. Compared with the previous computational models that are based on greatly simplified geometries (even for continuum-based models), the anatomical models are a significant step closer to patient-specific and high-fidelity modeling of phonation, which is eventually needed for clinical care of voices of individual patients. Some recently work, e.g., Xue et al. [42] and Mittal et al. [43], provide insights into the development towards such medical imaging based models of the vocal fold. More details about the development and improvement of vocal fold modeling can be found in review papers of Alipour et al. [44] and Mittal et al. [26]. Only a brief summary of literature is provided here to set up the context for the present study.

One issue related to patient-specific modeling is that even if a patient's anatomy could be reconstructed with high fidelity, there are still a few other modeling parameters whose values cannot be specified with accuracy, for example, the elastic properties of the tissue material that may vary from patient to patient. Even for the same patient, the effective stiffness of the tissue highly depends on neurological control of various muscle groups and consequently the adduction state of the vocal fold [45]. These uncertain parameters are important to capture the patient-specific vibration features [46]. Therefore, either ad hoc assumptions have to be made, or some parameter identification approach must be used to estimate those parameters. It will be too expensive to perform parameter identification using 3D FSI models due to their high computational cost. One possible method is thus to use a reduced-order model to determine those unknown material properties, which could then be used to enhance fidelity of the 3D models.

To construct a reduced-order FSI model for vocal fold vibration, it may be appropriate to simplify the description of the flow rather than the description of the tissue mechanics, especially when accurate capture of the vibration characteristics is desirable. This is because the vocal fold deformation is three-dimensional and can be complicated, requiring at least a 3D model representation; furthermore, 3D simulation of the turbulent glottal flow is typically much more expensive than 3D simulation of the tissue deformation, and reducing flow simulation can largely lower the overall computational cost. For such a purpose, the Bernoulli equation has been most widely used in the past to describe the pressure and velocity of the glottal flow. A comparison of the Bernoulli equation with the Navier−Stokes equation was studied by Decker and Thomson [47], who used a 2D setup, assuming either steady flow or FSI, to assess the accuracy of the Bernoulli principle. Their comparison showed that all Bernoulli based models result in similar predictions of the mean intraglottal pressure, maximum orifice area, and vibration frequency; however, those predictions rely on the heuristic specification of flow separation location in the Bernoulli models, and the location is quite different from that obtained from the simulation baed on the Navier−Stokes equation.

In a previous work [48], the authors coupled an anatomical vocal fold model that was based

on the MRI scan of the rabbit larynx with a Bernoulli based flow model to perform fast FSI simulations. Their flow model was calibrated a priori using 3D flow simulation of the same larynx, in which the 3D flow data were used to set up the curved flow path along the airway for the 1D model and also to specify the proper location of flow separation. Using a hybrid FSI model of the 1D flow and the 3D tissue and trying to match the model prediction with the experimental measurement of the vibration, they estimated the elastic constants of the vocal fold of each subject. Next, with the material properties identified for individual samples, the updated 3D FSI simulations were able to capture the specific vibration characteristics for each subject used in the study. In a later study, the same authors compared the hybrid FSI model with 3D FSI by using a simplified vocal fold geometry to more thoroughly assess the performance of such Bernoulli based 1D flow models [48]. They found that that model prediction can be sensitive to the subjective specification of the separation location; in some case where the medial thickness of the vocal fold is small, the hybrid FSI model leads to a significantly different vibration mode of the vocal fold than the 3D FSI model.

From these previous studies, it is clear that the Bernoulli equation has serious limitation in its capability to satisfactorily compute the pressure in the flow for a given geometrical configuration of the glottis. To address this limitation, in the present study we adopt a 1D momentum equation based flow model that was originally developed to solve separated flow in the collapsible tube [123, 124]. This model has been recently introduced for vocal fold modeling [125]. It includes the viscous effect as well as the pressure loss associated with flow separation that is typically encountered in a divergent channel. A recent review [126] discussed more applications of this model as well as its advantages and limitations. One particular limitation has to do with the significant viscous dissipation upstream the narrowest section of the channel that is not accounted for by the model [127, 126]. In the present study, we incorporate an empirical function in the 1D flow model to account for the entrance effect that takes place as the flow enters the glottal gap. By introducing a correction coefficient to the cross-section area, we exclude the boundary layer at the glottal entrance and limit the momentum equation to the core of the flow. Thus, our model is less affected by the viscous dissipation upstream the narrowest section that was discussed previously [127]. The objective of the present study is to describe this new flow model and assess its effectiveness in predicting vocal fold vibration when coupled with 3D tissue mechanics in a hybrid FSI model. To do so, we use an idealized yet 3D vocal fold geometry and perform 3D FSI simulations as the benchmark results for this setup. In order to test its robustness, we vary the medial thickness of the vocal fold (and thus the shape of the glottis during vibration), the subglottal pressure, as well as the material model of the tissue, and we also include the Bernoulli based models as supplementary references. In Section 2, we will first describe this 1D flow model and then introduce the validation setup. The results and discussions will be given in Section 3. Finally, we will provide concluding remarks in Section 4.

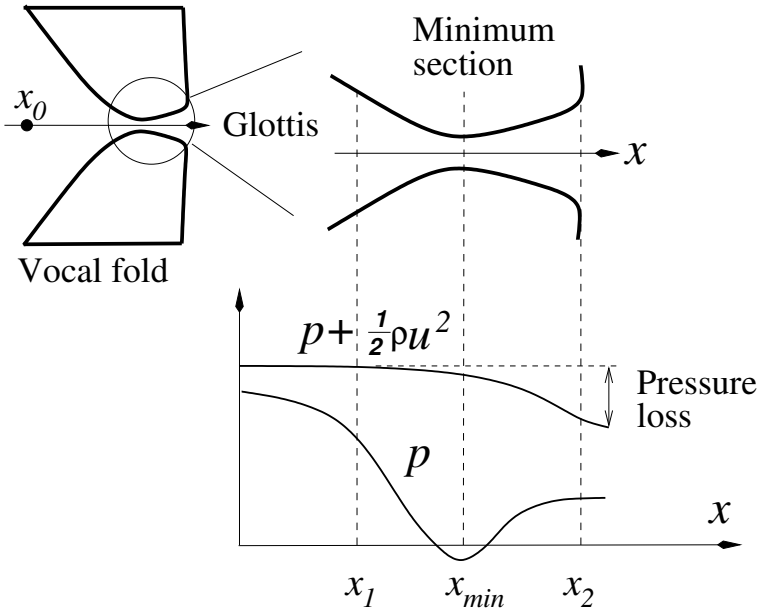

Figure 5.1: Illustration of pressure and total pressure along the center of the flow through a glottis-like gap.

5.2 Method

5.2.1 The one-dimensional viscous flow model

Figure 5.1 illustrates generally how an incompressible flow behaves while going through a glottis-like gap. Along the flow, the pressure first decreases to a minimal level at the narrowest section and then increases in the divergent section. However, due to the momentum losses to viscous resistance and velocity fluctuations, especially the losses associated with flow separation, the pressure at the exit does not recover to its full level at an entrance location with the same cross sectional area as the exit (i.e., x_1 and x_2 in Fig. 5.1), and the corresponding total pressure experiences significant loss after the minimum section as illustrated in Fig. 5.1. The amount of loss in the form of pressure decrease depends on the specific geometry as well as the Reynolds number. To describe the flow without resorting to the 3D Navier−Stokes equation, we use the 1D model developed by Cancelli and Pedley for flow in a collapsible tube [123]. In this model, the authors considered energy loss in a tube with increasing cross section, where the flow may experience significant viscous resistance as well as separation. The model consists of the unsteady continuity and momentum equations as below,

$$\frac{\partial A}{\partial t} + \frac{\partial Au}{\partial x} = 0 \tag{5.1}$$

$$\rho\frac{\partial u}{\partial t} + \rho u\frac{\partial u}{\partial x} + \frac{\partial p}{\partial x} - \tau\frac{s}{A} = 0 \tag{5.2}$$

$$\tau = \tau_{fric} + \tau_{\chi} \tag{5.3}$$

where ρ, u and p are respectively the density, velocity, and pressure, s is the perimeter around the cross-sectional area, A, and τ is the total stress that combines the viscous stress, τ_{fric}, and an additional stress, τ_χ, that causes loss of kinetic energy due to separation. The viscous term can be estimated based on fully-developed flow in a tube of constant cross section, i.e., $\tau_{fric} = -2\mu(\, s/A)\, u$. The loss of kinetic energy term can be modeled according to

$$\tau_\chi = \frac{A}{s}(\, 1 - \chi)\, \rho u \frac{\partial u}{\partial x}, \tag{5.4}$$

where $0 \leq \chi \leq 1$ is a constant representing pressure recovery. Plugging Eq. (6.2) into Eq. (6.1), one obtains a term like $(\, 1 - \chi)\, \rho u(\, \partial u/\partial x)$, which cancels part of the advection term and leaves only $\chi\, \rho u(\, \partial u/\partial x)$ in the momentum equation. Thus, $\chi = 1$ means there is no separation loss, and $\chi = 0$ means all kinetic energy is lost and there would be no pressure recovery. In Cancelli and Pedley [123], the sign of the production of the velocity and pressure gradient is used to determine the choice of χ. Here we simply set χ according to converging or diverging section, i.e.,

$$\chi = \begin{cases} 1, & \text{before the minimum section} \\ \chi_{min}, & \text{after the minimum section} \end{cases} \tag{5.5}$$

where χ_{min} is the minimum value of χ. With this definition of χ, the pressure in the converging section can be fully converted to kinetic energy – that is, the Bernoulli equation is satisfied (or, the unsteady Bernoulli equation is satisfied if the unsteady term is significant); in addition, the pressure loss in the diverging section is accounted for.

Given a specific geometrical configuration of the glottis, Eqns. (5.1) to (5.3) can be solved straightforwardly using a numerical method such as the finite-difference method. Similar to the 3D flow, the boundary conditions of the 1D model includes $p = P_{sub}$ at an upstream location $x = x_0$, $p = P_e$ at the glottal exit $x = x_2$, and the velocity u has zero derivative at $x = x_0$. Here we set x_0 to be the location where the cross section of the flow domain starts to change. P_e is generally close to the domain outlet pressure, P_{out}, but it may vary a little depending on the specific geometry of the vocal fold. We will choose its constant value based on the 3D FSI results.

While Eq. (6.1) is a reasonable description of the flow momentum along the centerline of the converging-diverging channel, the continuity equation, Eq. (5.1), assumes that the velocity profile in a cross section is nearly uniform. In reality, when the flow enters the glottal gap, the sudden narrowing of the cross section at the entrance causes a significant vena contracta effect. That is, the flow under inertia is more focused to the center as shown in Fig. 6.1, rather than following the exact shape of the channel. The vena contracta effect is more influenced by the high curvature of the entrance and may still exist even if the channel is straight or converging after the entrance. As a result, if the actual cross section area A is used for flow continuity, significant error could be introduced to the intraglottal velocity. As it is shown later in Section 3, without the entrance effect, the velocity at the minimum section may be over-estimated, leading to an erroneous prediction of strong negative pressure at the location.

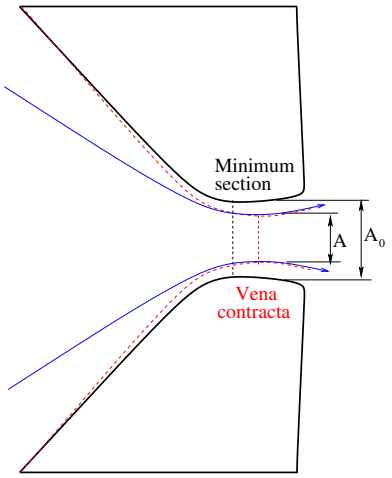

Figure 5.2: Schematic of airflow enters the glottis where the sudden change of geometry at the inlet introduces a vena contracta effect. A_0 is the actual cross section area, and A is the effective area.

To account for such an entrance effect, we define the effective cross section area, A, and the actual cross section area, A_0, and we introduce their ratio, α,

$$\alpha(x) = \frac{A(x)}{A_0(x)} \tag{5.6}$$

when considering the mass conservation along the channel. In the present study, the actual area A_0 is calculated directly from the instantaneous 3D vocal fold geometry, and $\alpha(x)$ will be determined empirically from the 3D FSI simulation as discussed later. With the function $\alpha(x)$ determined a priori, the effective area A can be calculated from Eq. (6.4) and is then used in the contiuity equation, Eq. (5.1).

5.2.2 Setup of the 3D FSI model

We use a simple geometrical setup in the full 3D FSI simulation to provide benchmark for the reduced-order FSI model. The setup is illustrated in Fig. 5.3, where a rectangular box represents the airway and its walls are assumed to be rigid. The total length of the rectangular box is 12 cm and the vocal fold starts from 2 cm from the inlet. The flow is assumed to be incompressible and is governed by the viscous Navier−Stokes equation in the full 3D model. A pair of vocal fold is placed symmetrically in the box with length $L = 20$ mm, width $W = 13$ mm, and depth $D = 10$ mm. The cross section of the vocal fold is uniform and has roughly a trapezoidal shape. The initial glottal gap is at 0.4 mm. The details of the cross section were described in [37, 48]. It was found previously that the medial surface thickness T significantly affects the configuration of the glottal shape during vibration and thus the intraglottal flow [48]. Therefore, two different medial surface thicknesses are used here, a large one with $T = 3.50$ mm and a small one with $T = 1.75$ mm.

For the boundary conditions, the left, right, anterior and posterior surfaces of the vocal fold, i.e., all the sides attached to the rectangular box, are treated as fixed surfaces, while the other

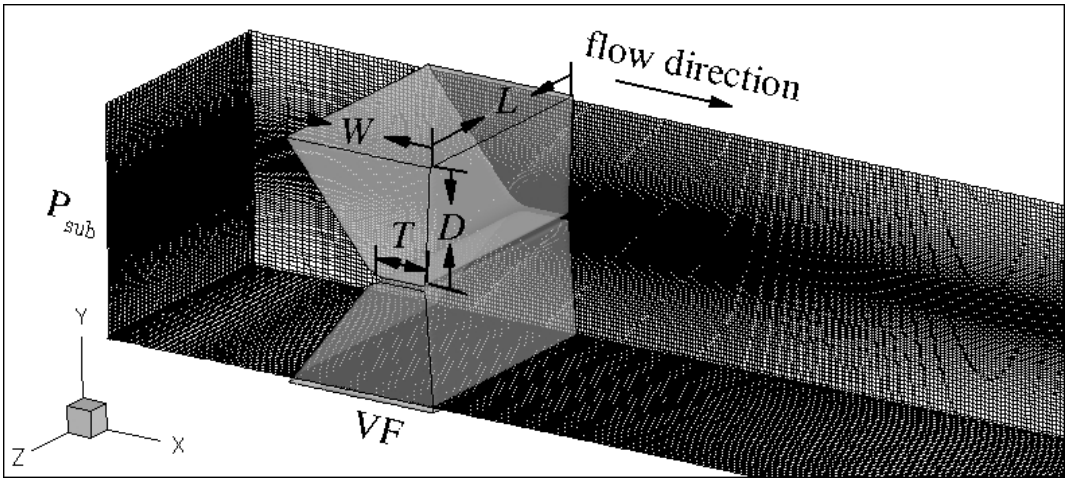

Figure 5.3: The vocal fold model and computational domain used in the study for 3D FSI simulation.

surfaces in contact with airflow are free to move. During vibration, the vocal fold is allowed to have a small gap of 0.2 mm for a minimal amount of flow to go through. The airflow is driven from left (inlet) to right (outlet) by a constant pressure drop between the subglottal pressure P_{sub} at the inlet and reference supraglottal pressure $P_{out} = 0$ kPa at the outlet. The pressure drop is around 1 kPa.

As the current study is focused on the reduced-order modeling for the glottal flow, the tissue model of the vocal fold is not of primary concern. Thus, despite that the real tissue is anisotropic and has a multi-layer structure, the vocal fold here is assumed to be isotropic and homogenous. Nevertheless, we adopt two different constitutive laws for the tissue material, the Saint Venant−−Kirchhoff model and a hyperelastic, two-parameter Mooney−Rivlin model. In both material models, nonlinear strains have been incorporated. More detail of the Saint Venant−Kirchhoff model can be found in our group's previous work [53]. The Mooney−Rivlin model is one of popular models for representing large deformations of soft tissues. The strain energy density function for this model is given as

$$W = \alpha_{10}(\overline{I}_1 - 3) + \alpha_{01}(\overline{I}_2 - 3) + K/2(J-1)^2 \tag{5.7}$$

where K represents the bulk modulus,α_{10} and α_{01} are material constants, and $J = \det(F)$ with F standing for the deformation gradient. In addition, $\overline{I}_1$ and $\overline{I}_2$ are invariants based on J and the principal stretches of the deformation gradient. Further detail of this model for the vocal fold can also be found in our group's previous work [53].

In both tissue models, the material density is $\rho_s = 1040$ kg/m^3 and mass damping is 0.05 s^{-1}. In the Saint Venant−Kirchhoff model, Youngs modulus is set to be $E = 15$ kPa, and Poisson's ratio is $\nu = 0.475$. For the Mooney−Rivlin model, $\alpha_{10} = 2.29$ kPa and $\alpha_{01} = 0.25$ kPa are used in the Mooney−Rivlin model to match the specified stiffness of the Saint Venant−Kirchhoff model at small strain. The air density is $\rho = 1.13$ kg/m^3. Thus, the characteristic intraglottal velocity is $V = \sqrt{2(P_{sub} - P_{out})/\rho} = 42.1$ m/s. We define the jet Reynolds number using $Re_J = \rho V d/\mu$,

where $d \sim 1$ mm is the characteristic glottal gap during opening phase and μ is the air viscosity. In the current study, we set $Re_J = 210$. If the channel height is used in the definition of the Reynolds number, we have $Re = 4200$.

5.2.3 Numerical method and mesh refinement study for 3D simulation

A finite-element method is used to solve the tissue deformation [53]. The vocal fold is meshed with approximately 18,000 20-nodes hexahedral elements and 80,000 vertex nodes. No-slip and no-penetration wall conditions are specified for all flow domain boundaries except the inlet and outlet, where either the inlet or outlet pressure is applied and the velocity is assumed to have a zero normal derivative. An immersed-boundary method is adopted for the flow simulation [60, 53, 1]. A non-uniform Cartesian grid with $320 \times 98 \times 72$ points is used to discretize the flow domain. The subglottal pressure is set to be P_{sub} =0.75, 1.0 or 1.25 kPa, which is within the range of the onset pressure for normal human phonation. The time step size $\Delta t = 0.0025$ ms is used for the FSI simulation, which leads to about 4000 steps for each vibration cycle that is approximately at 100 Hz.

A grid convergence study is done for the case with medial thickness $T = 3.5$ mm and $P_{sub} = 1.0$ kPa, while the Mooney−Rivlin model is employed for the material behavior. The nonuniform Cartesian grid is doubled in the region around the vocal fold and also in the flow region immediately downstream the vocal fold, and the time step size is reduced to 0.002 ms. From the results, a relative difference of 2.0% is observed between the baseline mesh and the fine mesh for the vibration frequency, 4.5% for the vibration amplitude, and 3.9% for the phase delay between the inferior or superior points on the medial surface. As seen later, these errors are much smaller when compared to the differences between the reduced-order model and the full 3D model. Therefore, the baseline mesh is considered to be acceptable for further investigations in this work.

5.3 Results and discussions

5.3.1 Results from 3D FSI simulations

The 3D FSI simulations provide full flow field data, including the velocity and pressure, to benchmark the reduced-order FSI model. Figure 5.4 shows a snapshot of the vortex structures in the flow for $P_{sub} = 1.0$ kPa and the Mooney−Rivlin model. These vortex structures are unsteady and generally follow the pulsatile jet to go downstream while interacting with one another and eventually dissipating. Fortunately, even though these vortices correspond to some degree of pressure fluctuations in the flow, they do not drastically change the pressure in the supraglottal region. Thus, we could assume a constant supraglottal pressure in the reduced-order model for P_e. From the 3D simulations, we obtain that the pressure is around $P_e = 0$ Pa for $T = 3.5$ mm and $P_e = -100$ Pa for $T = 1.75$ mm. In both $T = 1.75$ mm and 3.5 mm cases, the vocal fold exhibits a second-mode like vibration, where the oscillation resembles the second eigenmode of the current vocal fold structure

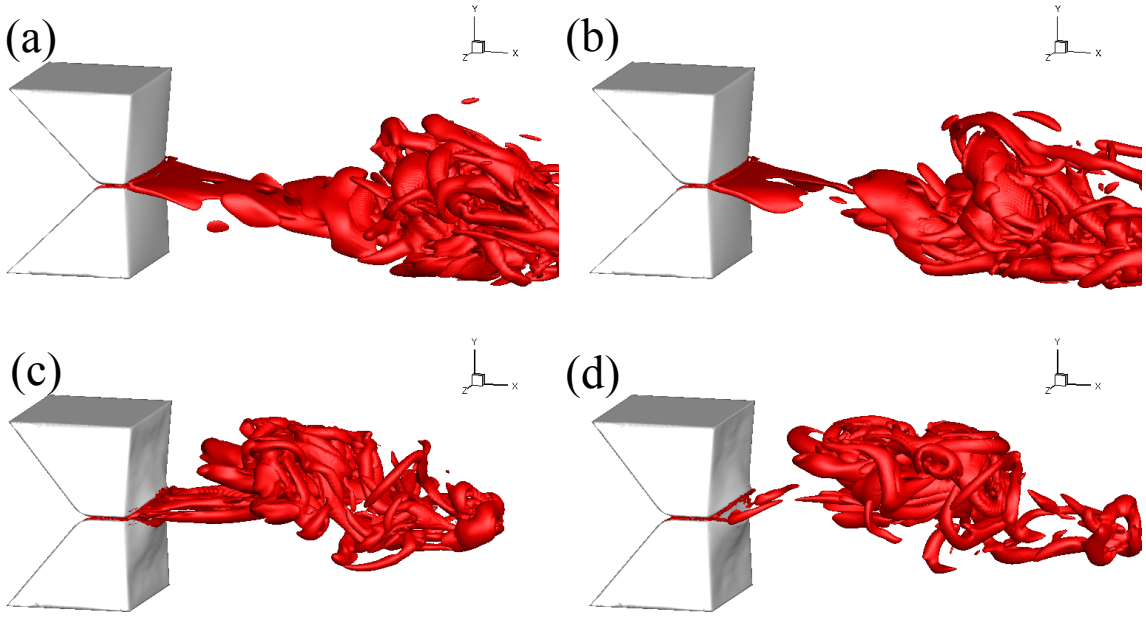

Figure 5.4: Vortices in the supraglottal region obtained from 3D FSI simulations for (a,b) small medial thickness $T = 1.75$ mm and (c,d) large medial thickness $T = 3.5$ mm. The isosurface is defined using the λ-criterion with the contour level at 20 s^{-1}. (a,c) Opening phase; (b,d) closing phase.

and is primarily in the lateral or y-direction [38]. The amplitude of vibration is $d = 0.89$ mm for $T = 1.75$ mm and $d = 1.22$ mm for $T = 3.5$ mm. Here the amplitude of vibration d is defined as the maximum y-displacement of the medial surface at the glottal exit (the gap width at the exit is thus $2d$). In the case of $T = 1.75$ mm, the glottis does not close completely (or reach the minimal gap) during closing phase, so flow is continuous despite being oscillatory. In the case of $T = 3.5$ mm, the glottis reaches the minimal gap and the glottal channel is significantly longer than the small thickness case; thus, the jet is nearly completely cut off during closing phase, while during opening phase the jet has shorter penetration downstream.

We use the velocity field data from the 3D simulations to calculate the area correction coefficient, $\alpha(x)$, which is defined in Eq. (6.4). As shown in Fig. 5.5, the velocity profile across the glottis is nonuniform, and as stated in Section 2.1, introducing such area correction would improve accuracy of the 1D mass conservation equation. This coefficient is calculated by computing the ratio between the avergage streamwise velocity in a cross section, u_{avg}, and the maximum streamwise velocity of the cross section, u_{max}, i.e.,

$$\alpha(x) = \frac{u_{avg}}{u_{max}} = \frac{\frac{1}{A_0}\int u \, \mathrm{d}S}{u_{max}}. \tag{5.1}$$

If the flow inside the glottis is symmetric, then u_{max} is also the centerline velocity. During vibration, $\alpha(x)$ varies somewhat depending on the instantaneous shape of the glottal gap. However, the

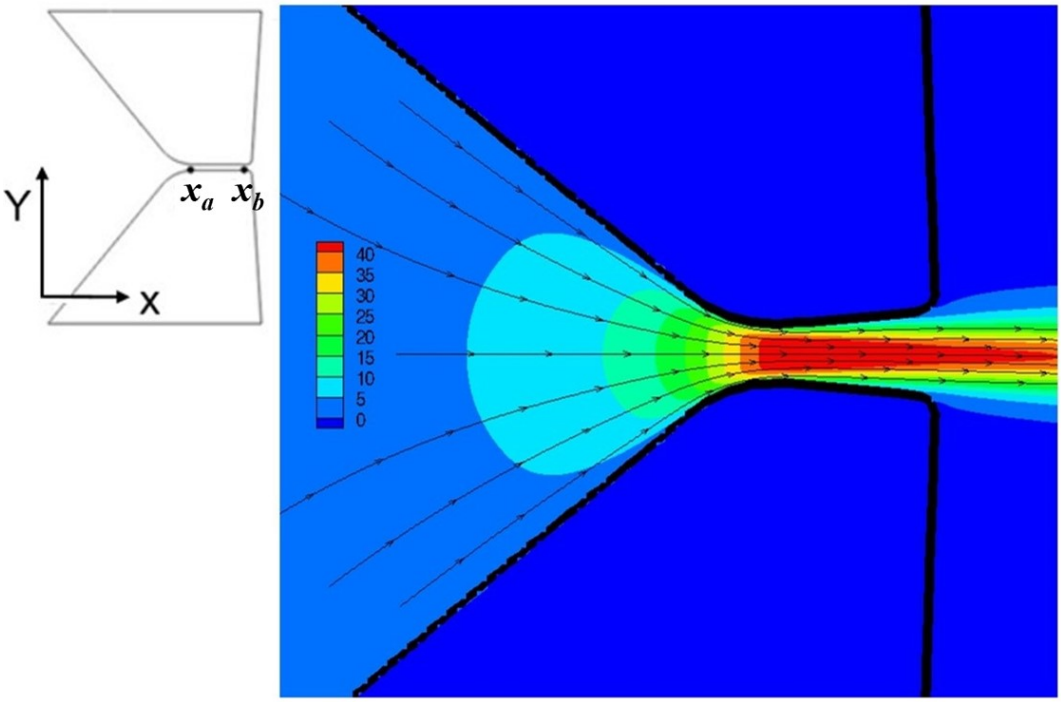

Figure 5.5: Streamline plot and contours of the streamwise velocity within the $z = 0$ slice for $T = 1.75$ mm.

Table 5.1: Four reduced-order flow models used for comparison

Model	Governing equation	Entrance effect	Separation location
B1	Bernoulli equation	No	Minimal area
B2	Bernoulli equation	No	Glottal exit
M1	1D momentum equation	No	–
M2	1D momentum equation	Yes	–

coefficient is around 1 at the inlet and 0.75 at the exit from the simulation results. The inlet location x_a and the exit location x_b are marked out in Fig. 5.5. We use a quadratic function to approximate α and demand that it has zero derivative at x_b. The result gives the following expression for $\alpha(x)$,

$$\alpha(x) = \frac{(x - x_b)^2}{4(x_a - x_b)^2} + 0.75 \quad \text{for} \quad x_a \le x \le x_b \tag{5.2}$$

As shown later, it turns out that the same function for α can be used for different cases of the medial thickness, subglottal pressure and tissue behavior.

5.3.2 Comparison of the reduced-order models

We consider two setups of the momentum-based reduced-order FSI model. In the first, the flow is described by Eqns. (5.1) to (5.3) but no entrance effect is incorporated (i.e., $\alpha(x) = 1$); this model is denoted by M1. The second model includes the entrance effect for the flow using the area correction coefficient given by Eq. (5.1), and this model is denoted by M2. In addition to these two models, we consider two Bernoulli based flow models, i.e., removing the last term in Eq. (6.1) that involves τ. These two models are denoted by B1 and B2, respectively. For B1, we set the location of flow separation always at the minimum cross section area within the glottis, at which and further downstream the pressure is set to $p = P_e$. For B2, we set the separation location always at the glottal exit with the same pressure specification. These four models are summarized in Tab. 5.1. For all reduced-order models, the same vocal fold model as that in the 3D model is used for FSI simulation. In each case, data collection is done after sustained vibration is established.

Figure 5.6 shows the vibration pattern of the vocal fold within the mid-plane $z = 0$ that is predicted by different FSI models. In this case, $T = 1.75$ mm, $P_{sub} = 1.0$ kPa, and the Mooney-−Rivlin model are used. Furthermore, for all cases with the smaller medial thickness, $\chi_{min} = 0.5$ has been adopted; and for all cases with the larger medial thickness, $\chi_{min} = 0.2$ has been adopted to account for more pressure loss in this case. The original rest shape of the vocal fold is included in the figure as a reference. The vibration pattern from the 3D simulation indicates a second-mode like vibration, where the vocal fold oscillation is primarily in the lateral or y-direction. In contrast, model B1 produces a vibration pattern that resembles the first eigenmode of the vocal fold, where the vocal fold oscillates primarily in the streamwise or x-direction and the eigen frequency is at 73 Hz for the current vocal fold structure. Even though this oscillation mode also leads to opening and closing of the glottis, the vibration frequency is significantly lower than the second eigenmode whose frequency is at 126 Hz for the current vocal fold structure. The other three reduced-order models, B2, M1, and M2 all produce a second-mode like vibration. However, the amplitude of the vibration is different among these models. For B2 and M1, the vibration amplitude is significantly greater than that of the 3D FSI model. Detailed comparisons are shown in Tab. 5.2 for the vibration frequency f, amplitude d, and phase delay ϕ between the glottal inlet and exit (i.e., the phase difference between points 1 and 2 indicated in Fig. 5.5). The data in the table show that for all these quantities, M2 produces the closest result to that of the 3D FSI model.

For the large medial thickness case of $T = 3.5$ mm, the comparison of the vibration pattern is shown in Fig. 5.7, where $P_{sub} = 1.0$ kPa and the Mooney−Rivlin model are used. In this case, B1, M1, and M2 achieved the second-mode dominant vibration and are similar to the 3D FSI model. B2 model did not reach a steady vibration pattern, and instead the deformation becomes overly large, causing the simulation to diverge. Further examining the patterns shown in this figure, we see that in B1 the glottis switches between a divergent shape and a straight shape in a vibration cycle, while in both M1 and M2, the glottis has a convergent shape during opening, a divergent shape during closing, and a straight shape in between, i.e., a similar sequence of deformation to

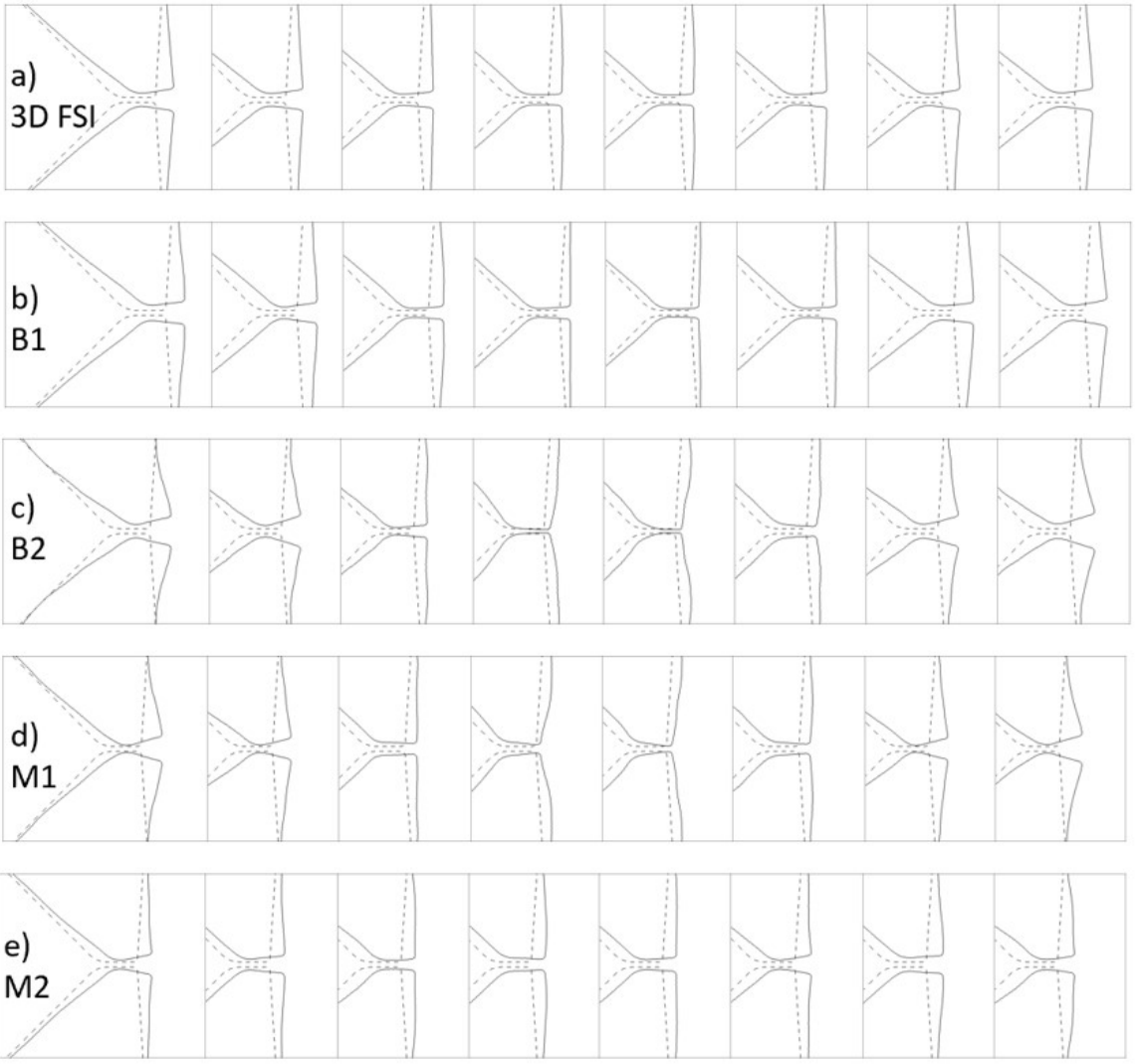

Figure 5.6: Vibration pattern in the mid-plane $z = 0$ obtained by different FSI models for the vocal fold with small medial thickness: a) 3D FSI simulation, b) B1, c) B2, d) M1, and e) M2. The dashed lines indicate the original shape of the vocal fold.

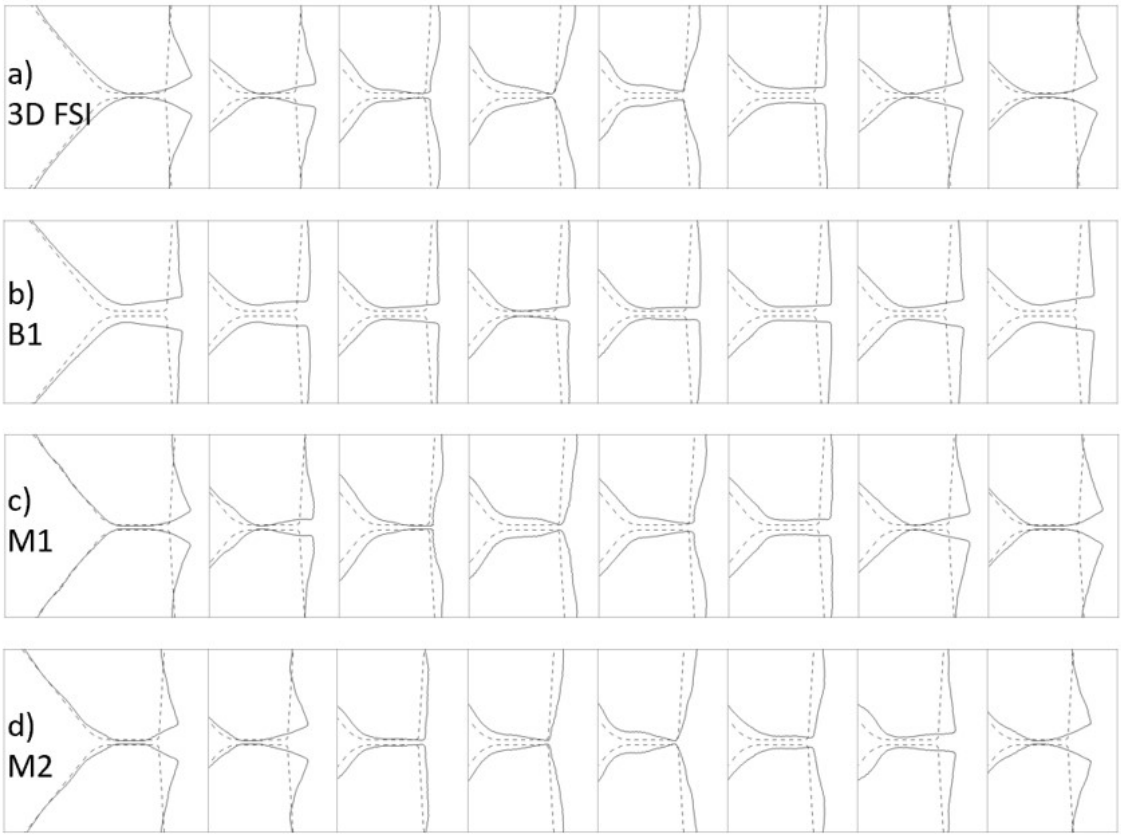

Figure 5.7: Vibration pattern in the mid-plane $z = 0$ obtained by different FSI models for the vocal fold with large medial thickness: a) 3D FSI simulation, b) B1, c) M1, and d) M2. The dashed lines indicate the original shape of the vocal fold.

Table 5.2: Reduced-order models compared with 3D FSI for vocal fold in terms of vibration frequency f, amplitude d, and phase delay ϕ.

T (mm)	Model	f (Hz)	difference	d (mm)	difference	$\phi(^\circ)$	difference ($^\circ$)
54em1.75	3D FSI	132	-	0.89	-	-19	-
	B1	78	40.1%	1.27	42.8%	-9	10
	B2	140	7.7%	1.44	62.0%	10	29
	M1	144	10.8%	1.38	54.9%	21	40
	M2	144	7.7%	0.78	12.5%	-15	4
54em3.50	3D FSI	140	-	1.22	-	157	-
	B1	136	2.3%	1.31	7.4%	98	59
	B2	-	-	-	-	-	-
	M1	144	2.9%	1.25	2.5%	186	29
	M2	144	2.9%	1.20	1.4%	161	4

that predicted by the 3D FSI model. The quantitative comparison in Tab. 5.1 shows that even though M1 and M2 produce close results to the 3D FSI, but M2 is better in terms of the vibration amplitude and the phase delay.

5.3.3 Comparison of pressure distribution

To further study the difference among the four reduce-order models, we compare the pressure distribution along the flow, especially in the region within the glottis, since the pressure directly causes the vocal fold displacement and provides the mechanism for sustained vibration. For the comparison, we use the vocal fold deformation obtained from the 3D FSI simulation and calculate the pressure distribution using the four 1D flow models summarized in Tab. 5.1. This way, the glottal configuration is the same across different models, and we can focus on the pressure calculation given by these flow models.

Figure 5.8 shows the pressure distribution for the case of $T = 1.75$ mm at both closing and opening phases. At the closing phase, M2 has the closest distribution to the 3D FSI among the four reduced-order models. For B1, B2, and M1, the pressure drops too fast as the flow enters the glottis. This is because for M2, introducing the entrance effect moves the minimal cross sectional area further downstream within the glottis and thus improves the pressure prediction near the glottal entrance. At the opening phase, B1 and M2 both produce reasonable pressure distribution close to the 3D FSI result, though M2 also generates a negative pressure zone in the glottis like the 3D FSI model. Both B2 and M1 have a presence of strong negative pressure, especially for B2 since its separation location is set at the glottal exit and thus over-predicts the negative pressure at the narrowest cross section. Overall, we see that including the entrance effect allows M2 to have better performance than the other 1D models.

(a)

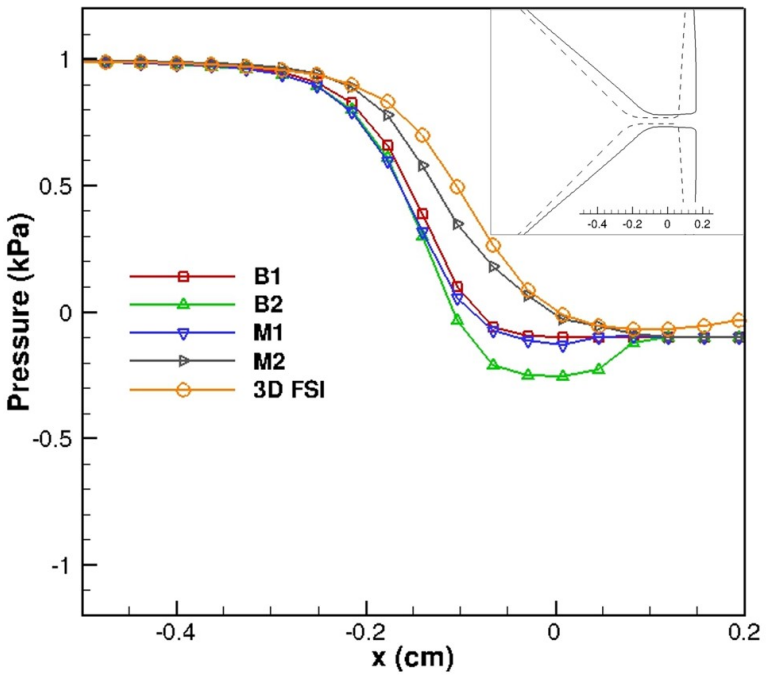

(b)

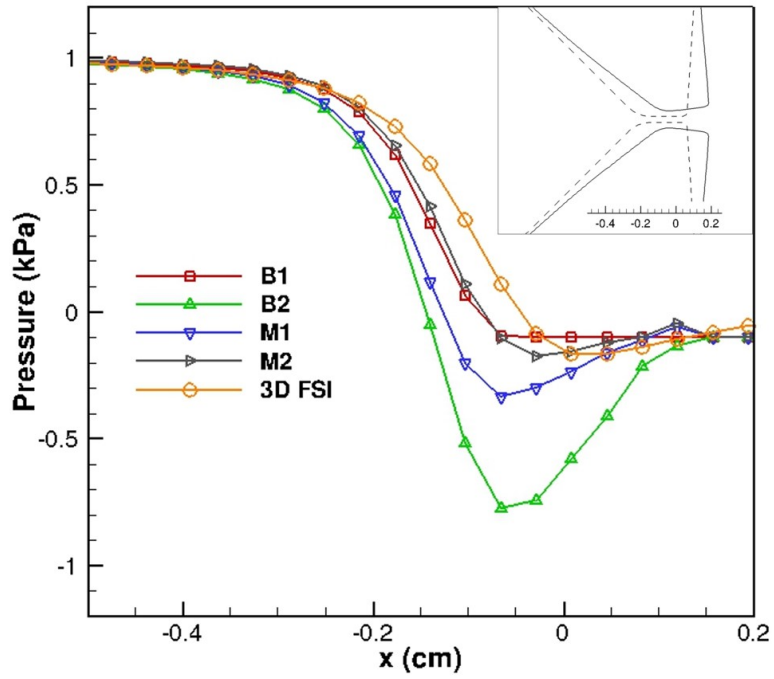

Figure 5.8: Comparison of pressure distribution for different models where $T = 1.75$ mm. (a) Closing phase, and (b) opening phase.

(a)

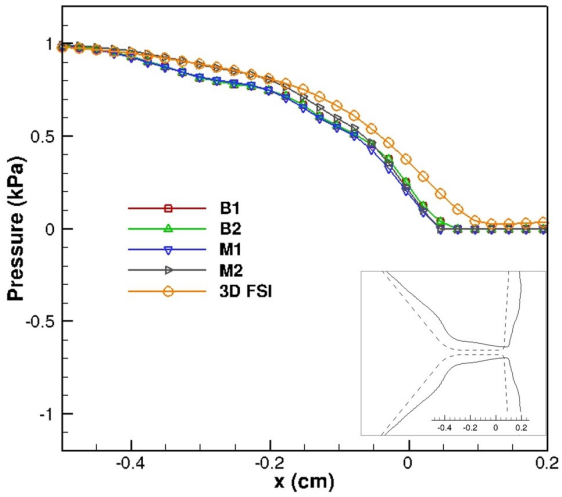

(b)

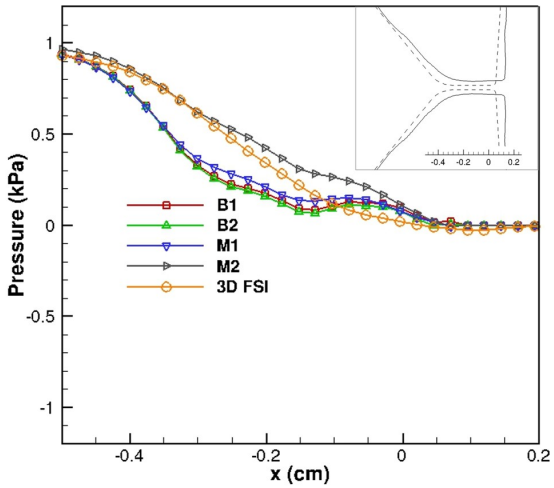

(c)

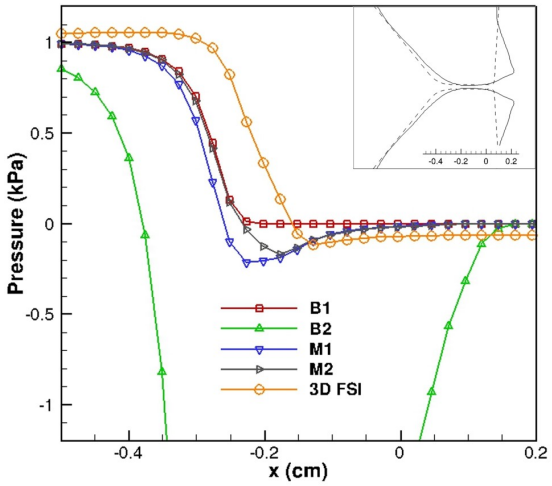

Figure 5.9: Comparison of pressure distribution for different models where $T = 3.5$ mm. (a) Opening phase, (b) maximum opening, and (c) closing phase.

Figure 5.9 shows the pressure distribution for the case of $T = 3.5$ mm at opening, maximum opening, and closing phases, where the glottal shape is convergent, straight, and divergent, respectively. For the closing phase in (a), the glottal exit has the minimal cross sectional area. Consequently, B1 and B2 have the same separation point and thus the identical pressure prediction. M1 also produces a very close result to those of B1 and B2 since no pressure loss in the divergent section is involved and the frictional stress is small. M2 gives better pressure prediction near the entrance (between $x = -0.4$ and -0.2 cm). After $x = -0.1$ cm, all reduced models have similar results.

When the glottis is straight, Fig. 5.9(b) shows that M2 again has the best prediction, and the pressure drops too fast near the entrance for the other 1D models. For the closing phase with a divergent glottis, Fig. 5.9(c) shows that B1, M1, and M2 all have significant error with low pressure prediction near the entrance. B2 predicts an overly low pressure; thus in the FSI simulation, this model broke down and did not reach a converging result. Similar to the 3D FSI, M2 also produces a negative pressure zone with proper magnitude, despite that the location of the zone is slightly upstream in comparison with the 3D FSI. This negative pressure zone is instrumental for the closure of the glottis.

5.3.4 Effects of the subglottal pressure and tissue model

To further assess the performance of model M2, we vary the subglottal pressure, so that $P_{sub} = 0.75$, 1.0, or 1.25 kPa, and we repeat the comparison of M2 with the 3D FSI model. In this study, only B1 is selected as a reference since B2 may not produce a converged result. The other parameters remain the same for this comparison. Figure 5.10 shows the comparison of the vibration frequency, amplitude, and phase delay for $T = 1.75$ mm as P_{sub} is varied. The 3D FSI results show that as the subglottal pressure is raised, the vibration frequency only slightly increases; the vibration amplitude more than doubled; and the phase delay remains nearly constant. For all three subglottal pressure levels, the results from M2 agree well with the 3D FSI, while the B1 produces a different vibration mode that has a much lower frequency.

Figure 5.11 shows the comparison for $T = 3.5$ mm under different subglottal pressures. In this case, the Bernoulli based model, B1, predicts the correct vibration mode whose frequency and amplitude are close to those of the 3D FSI; however, the momentum-based model, M2, has clearly better performance in that its frequency, amplitude, and phase delay all have visibly better agreement with those of the 3D FSI. These results indicate that the performance of model M2 is not significantly influenced by the subglottal pressure.

All the results presented here have been based on a Mooney−Rivlin model for the material behavior of the vocal fold tissue. To further expand the study and ensure that the new model is insensitive to the choice of the material parameters of the vocal fold, we used a Saint Venant−Kirchhoff tissue model to repeat both the 3D and reduced-order FSI simulation. $P_{sub} = 1.0$ kPa, and the same two medial thickness values are used. The results are shown in Tab. 5.3 for B1,

(a)

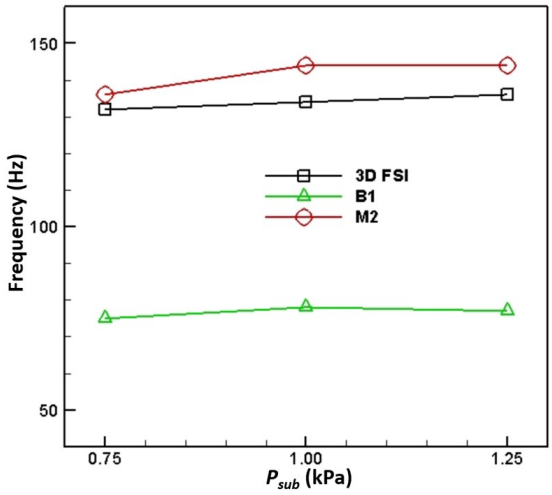

(b)

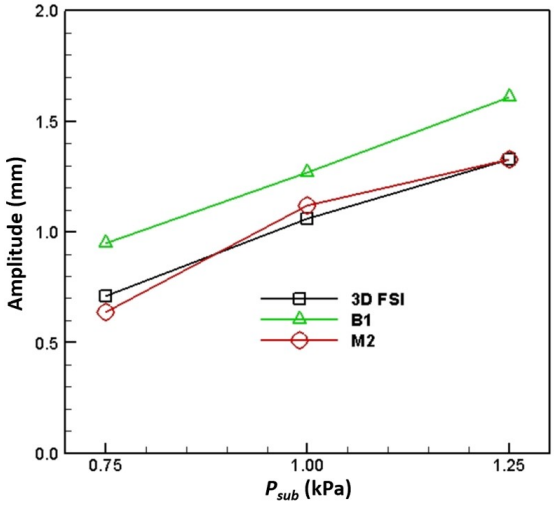

(c)

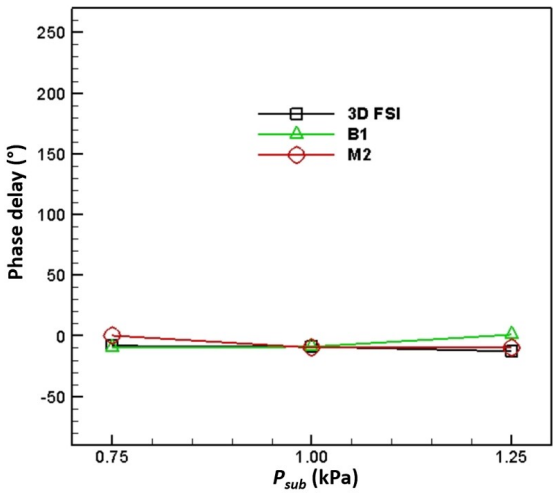

Figure 5.10: Comparison of B1, M2, and 3D FSI at different subglottal pressures for $T = 1.75$ mm. (a) Vibration frequency, (b) amplitude, and (c) phase delay.

(a)

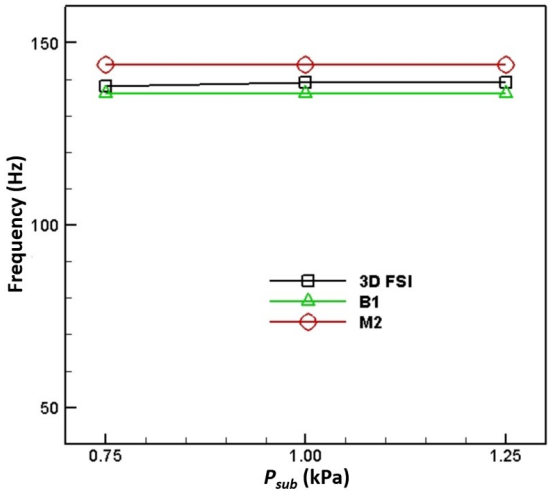

(b)

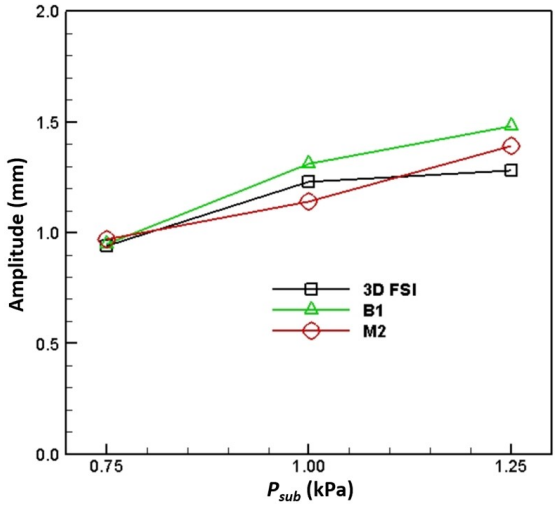

(c)

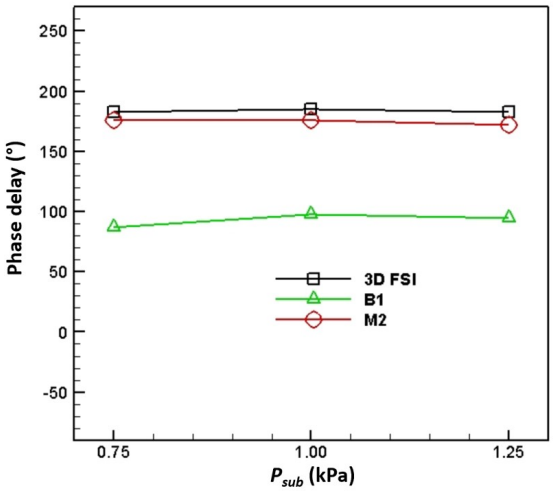

Figure 5.11: Comparison of B1, M2, and 3D FSI at different subglottal pressures for $T = 3.5$ mm. (a) Vibration frequency, (b) amplitude, and (c) phase delay.

Table 5.3: Comparison of the reduced-order models with the 3D FSI using a Saint Venant−Kirchhoff material model for the vocal fold tissue

T (mm)	model	f (Hz)	difference	d (mm)	difference	$\phi(^\circ)$	difference ($^\circ$)
34em1.75	3D FSI	126	-	1.07	-	-9	-
	B1	72	42.9%	1.35	26.2%	-5	4
	M2	128	1.6%	1.05	1.9%	5	14
34em3.50	3D FSI	133	-	0.97	-	76	-
	B1	128	3.8%	1.25	28.9%	62	14
	M2	128	3.8%	1.06	9.3%	83	7

M2, and 3D FSI. The data show that M2 again has better agreement with the 3D FSI in terms of vibration frequency, amplitude, and phase delay for both $T = 1.75$ mm and 3.5 mm. Therefore, the choice of the material model of the vocal fold does not affect performance of model M2 for the FSI simulation.

5.3.5 Further discussions

Unlike the Bernoulli based models, the 1D flow model introduced in the present work does not need an explicit specification of the separation point in the glottis. Instead, partial loss of the kinetic energy in the divergent section is considered in the new model. This consideration allows for incomplete pressure recovery in the section, including downstream the separation point. Thus, the intraglottal pressure predicted by the model goes through a much smoother transition from the glottal entrance to the exit, a feature that the actual pressure distribution should have as shown by the 3D simulation results in Section 3.4. We point out that even though the energy consideration in the present model is different from boundary layer separation consideration in the Bernoulli model, the two perspectives are still largely congruent with each other. This is because the boundary layer separation leads to significant mixing of the separated flow and is the primary reason for energy loss in the flow.

The introduction of a correction to the cross sectional area addresses the effect of the geometry at the glottal entrance and thus further improves the pressure prediction by the new model. Although the numerical solution to this model requires an iteration process, the computational cost of the simple governing PDE is minimal compared to that of solving the 3D Navier−Stokes equation or that of solving the 3D solid mechanics of the tissue deformation. Finally, the present 1D flow model can be reduced to a Bernoulli model by setting $\chi = 1$ before an assumed separation point, i.e., allowing for pressure recovery prior to flow separation, and also by setting $\alpha = 1$, i.e., ignoring the entrance effect. On the other hand, simply modifying the location of separation in the Bernoulli model does not give the same result as the current model. Therefore, the current approach offers more flexibility than the Bernoulli based approach.

It should be pointed out that the current flow model has several limitations. Like the Bernoulli models, the current model reduces the glottal flow to 1D, thus drastically simplifying the flow behavior. Only a constant value of the pressure recovery coefficient χ is assumed in the model for the divergent section. This treatment ignores the difference before and after the separation point that may be located somewhere between the minimum cross section and the glottal exit. As a result, it should be anticipated that this model does not always provide significantly better accuracy than the Bernoulli based models even though it generally has more advantages. The current model contains a free parameter, χ, and a function, $\alpha(x)$, which need to be set properly. The former depends on channel length of the glottis, as shown by the effect of the medial thickness in the current study, and also likely by the degree of the divergent angle if the angle is large; the latter should be more influenced by the curvature of the vocal fold surface near the glottal entrance as well as the Reynolds number. In the current study, $\alpha(x)$ is empirically determined using 3D simulation data from a specific vocal fold model setup. In the future, it would be desirable if a more general form of this function is determined for broader situations.

5.4 Chapter conclusion

We have introduced a new one-dimensional flow model for the glottal flow and for the FSI simulation of vocal fold vibration. This model is based on the reduced momentum equation with the entrance effect and the energy loss/partial pressure recovery in the divergent section included. We used a simple vocal fold configuration and performed 3D FSI simulations to assess the performance of the reduced-order FSI model. Two different medial thicknesses, three subglottal pressures, and two material behaviors were considered in the study. The results show that after incorporating the entrance effect, the momentum based flow model provides significantly more accurate predictions of the vibration characteristics than the Bernoulli based models as well as the momentum based model that does not incorporate the entrance effect. Therefore, the new model offers a useful approach in the applications of the reduced-order FSI model for the vocal fold such as parameter identification.

Chapter VI

A reduced-order flow model for vocal fold vibration: from idealized to subject-specific models

6.1 Introduction

The lifetime prevalence of voice disorders in the United States adult population is 30% with point prevalence rates of 6.6% to 7.5% [128]. Voice disorders are debilitating and can lead to significant socioemotional consequences, loss of income, and long-term disability. Certain voice disorders, e.g., unilateral vocal fold paralysis, may require surgery for voice restoration. Due to many factors such as surgical techniques, patient variations, and experience of surgeons, the revision rates of the surgeries can vary widely, and there are sometimes inconsistent or even undesirable clinical outcomes. Thus, there is significant need for a clinical tool to assist surgeons with pre-operative planning and to improve patient outcomes. Since the voice production directly depends on vocal fold vibration, a result of fluid–structure interaction (FSI) between the glottal airflow and vocal fold tissue, developing patient-specific computational models capable of simulating vibration of surgically modified vocal folds and predicting the surgical outcome would be useful in individualized surgical planning for patients.

Numerous computational models with different levels of complexity are available to simulate the FSI process of vocal fold vibration. In the early stage, lumped-mass structural models coupled with a low-order fluid model were often used [28, 29, 44, 30]. With drastic simplification but high computational efficiency, these models provided insightful information about the physical process such as onset of self-sustained oscillations and basic parameter effects. With tremendous growth of computational power, 2D or 3D models of the glottal flow simulation, as well as finite-element method (FEM) based tissue models have been commonly adopted for more accurate simulations of vocal fold vibrations [31, 32, 36, 33, 37–39, 129, 130, 35, 131, 132]. Even though simplified geometries of vocal fold were assumed in these references, the fundamentals of the FSI process in vocal fold vibration have been better understood, such as the vortex dynamics, tissue deformation, acoustics, and effects of geometrical and material properties.

In addition to growth of computing technology, recent development in medical imaging technologies, e.g., computed tomography (CT) and magnetic resonance imaging (MRI), allows the computational models to become more realistic and even subject-specific. These imaging modalities may provide detailed 3D anatomy of the larynx as well as the interior structure of the tissue [40, 41, 2],

which can be incorporated into a computational FSI model as the laryngeal geometry and the tissue structure of the specific subject that is being modeled. Examples of such patient-specific FSI models include Mittal et al. [43], Alipour et al. [133], Xue et al. [42], and also Chang et al. [48]. More details about the development techniques for such computational models can be found in recent reviews of Alipour et al. [44] and Mittal et al. [26].

Although medical imaging techniques can provide detailed anatomy of the larynx for vocal fold modeling, imaging data only provide geometric information that can be used for 3D spatial representations of the tissue and air domain. A high-fidelity 3D model is still limited by the uncertain tissue properties of individual patients, which depends on factors such as fiber composition [134] as well as active control due to muscle activities [25]. These uncertain parameters are important to capture the subject-specific vibration features [46]. It is possible to solve an inverse problem to determine these parameters by performing multiple system simulations and continuously updating their estimated values. However, 3D simulations, especially those of the glottal airflow, are prohibitive, making the procedure rarely practical. It is thus desirable to much simpler model for parameter identification prior to high-fidelity simulations. In a previous work of ours [135], we used a 1D calibrated Bernoulli flow model coupled with 3D FEM model of the vocal fold to determine the stiffness properties of individual samples of rabbit vocal fold, and the resulting FSI model was able to capture the subject-specific vibration as compared with the *in vivo* experimental measurement.

Bernoulli based equations have long been used for vocal fold vibration. Decker and Thomson [47] compared the Bernoulli equation with the Navier−stokes equation for the 2D vocal fold vibration, and they found that the Bernoulli model has to rely on heuristic specification of flow separation location within the glottis in order to produce similar results as the Navier−stokes equation. Similar conclusion was drawn later by Chang [48], who found that the Bernoulli equation may lead to a significantly different vibration mode of the vocal fold than the 3D FSI model. To address the limitation of the Bernoulli equation, in a recent work [66], we developed a new 1D momentum equation based flow model that was originally designed to solve separated flow in the collapsible tube [123, 124] and has been recently introduced for vocal fold modeling [125]. In this model, we took into account for the entrance effect, which is due to inertial flow entering the glottis from a sharply converging shape in the subglottal region. Using an idealized vocal fold geometry, we compared this 1D flow model with 3D model in FSI simulations and found that the 1D model produces consistent results with those from the 3D model for different medial thicknesses, subglottal pressures, and tissue models. In the present study, we aim to extend this model to more general situation to different tissue stiffness properties as well as subject-specific, anatomical vocal fold models. Similar to the previous study [66], we will use the full 3D FSI to assess performance of the 1D model in the case of idealized geometries; however, for the subject-specific models, we will directly compare the simulation results with the vibratory characteristics derived from *in vivo* experimental measurement. Therefore, this study represents a significant step toward application of reduced-order models in patient-specific modeling.

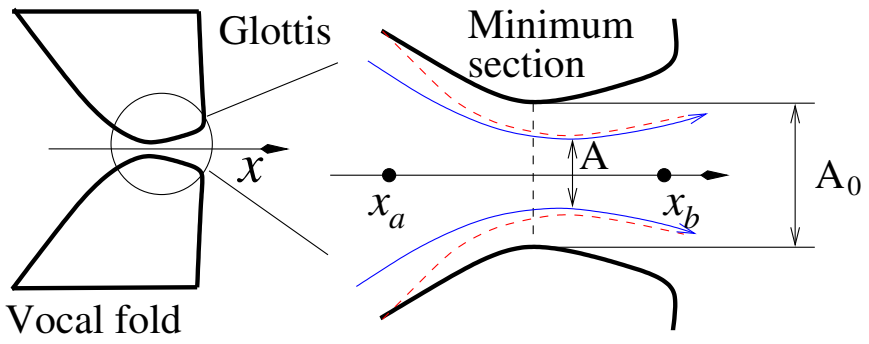

Figure 6.1: Schematic of airflow entering the glottis where sudden change of the geometry at the inlet introduces a vena contracta effect. A_0 is the actual cross section area, and A is the effective area. The blue arrow lines represent the streamlines and the red-dashed lines the boundary layer thickness.

6.2 Modeling methods and case setup

6.2.1 The one-dimensional viscous flow model

We consider the airflow flowing in the narrow glottal section between the two medial surfaces of the vocal fold, which in general has a converging-diverging shape as shown by a schematic in Fig. 6.1. The flow is considered to be viscous and incompressible due to its low Mach number (Ma $\sim$ 0.1). Due to separation from the vocal fold surface and viscous effect, the total pressure may experience significant loss. Considering the mass and momentum conservation equation, Cancelli and Pedley [123] developed a 1D flow model to describe a collapsible tube. The model can be written as

$$\begin{aligned} \frac{\partial A}{\partial t} + \frac{\partial Au}{\partial x} &= 0 \\ \rho\frac{\partial u}{\partial t} + \rho u\frac{\partial u}{\partial x} &= -\frac{\partial p}{\partial x} + \tau\frac{s}{A} \\ \tau &= \tau_{fric} + \tau_{\chi} \end{aligned} \tag{6.1}$$

where ρ, u and p are respectively the density, velocity, and pressure, s is the perimeter around the cross section, A is the effective cross section area, and τ is the total stress that combines the viscous stress, τ_{fric}, and an additional stress, τ_{χ}, that is associated with loss of kinetic energy due to flow separation. In Cancelli and Pedley [123], the loss of the kinetic energy term is modeled as

$$\tau_{\chi} = \frac{A}{s}(1-\chi)\,\rho u\frac{\partial u}{\partial x}, \tag{6.2}$$

where $0 \le \chi \le 1$ is a constant representing pressure recovery; $\chi = 1$ means there is no separation loss, and $\chi = 0$ means all kinetic energy is lost and there would be no pressure recovery. Here we simply set $\chi = 1$ in the converging section and $\chi = \chi_{min}$ for the diverging section, where χ_{min} is the minimum value of χ that will be set for specific vocal fold geometry.

In Cancelli and Pedley [123], the the viscous stress τ_{fric} is estimated using fully-developed flow in a tube of constant cross section, i.e., $\tau_{fric} = -C_0\mu(\, s/A)\, u$, where C_0 is the parameter related the shape of cross section, e.g., $C_0 = 2$ for the circular section and $C_0 = 3$ for a rectangular section with aspect ratio higher than 10. We assume that the viscous effect is grouped into τ_χ for the diverging section. Thus, τ_{fric} is only calculated for the converging section.

In addition to the model described by Eq. (6.1), we also consider the entrance effect in the present flow model. That is, when the glottal airflow enters the narrow glottal gap from the much wider subglottal region, it experiences a significant vena contracta effect, and consequently, the effective cross sectional area of the flow core, A, is smaller than that of the actual cross sectional area, A_0, as illustrated in Fig. 6.1. Without such entrance effect, the negative pressure at the minimum section could be over-estimated, leading to inaccurate pressure load on the vocal fold surface. To calculate the effective area A, we introduce a correctional coefficient, $\alpha(x)$, so that

$$A(x) = \alpha(x)A_0(x). \tag{6.3}$$

In our previous work, we empirically determined $\alpha(x)$ based on the 3D simulation of the FSI problem by calculating it from $\alpha(x) = u_{avg}/u$, where u_{avg} is the average velocity in the cross section and u is the centerline velocity. Based on the simulation data, a quadratic function was used to approximate $\alpha(x)$ from the glottal inlet x_a to the exit x_b shown in Fig. 6.1,

$$\alpha(x) = 1 - C_1 + C_1\frac{(x - x_b)^2}{(x_a - x_b)^2} \quad \text{for} \quad x_a \le x \le x_b. \tag{6.4}$$

Thus, $\alpha = 1$ at x_a and $1 - C_1$ at x_b, respectively. C_1 is the parameter to be set in the flow model based on the overall shape of the glottis.

For the boundary conditions of the 1D flow, we set a specified subglottal pressure $p = P_0$ at the inlet and $p = P_e$ at the glottal exit. The specific choices of these parameters, as well as the loss coefficient χ_{min} in Eq. (6.2) and C_1 in Eq. (6.4) for the area correction function will be specified later in the case studies. To solve the nonlinear boundary value problem, we use a shooting method as described in Li et al. [66].

6.2.2 Setup of the FSI model for idealized geometries

Figure 6.2 shows the idealized vocal fold considered in the present study. This geometric model was also used in our previous studies [130, 66]. The rectangular channel of 120 mm in length represents the larynx, and its walls are assumed to be all rigid. The inlet has a fixed subglottal pressure P_0 =1.0 kPa, and the outlet has a reference pressure of $P_{out} = 0$ kPa for all the cases in consideration. The airflow is assumed to be incompressible and is governed by the viscous Navier−Stokes equation in the full 3D model. A pair of vocal fold bands are placed symmetrically in the channel at $x = 20$ mm from the inlet. The length, width, and depth are $L = 20$ mm, $W = 13$ mm, and $D = 10$ mm, respectively. These length parameters are chosen to represent human vocal fold [31]. The cross section of vocal fold is uniform and the glottal gap is set to be 0.4 mm initially. The details

of the cross section profile were described in previous works [37, 130]. The medial thickness, T, has significant effects on the flow and the vocal fold vibration [48], as the medial surfaces are the primary loading surfaces for the sustained vibration. Two different values of T will be considered, a larger one of $T = 3.50$ mm and a smaller one of $T = 1.75$ mm. The surfaces of the vocal fold in contact with the air are free to move, while the other boundaries are fixed. The flow is driven by the pressure difference between the inlet and outlet of the channel.

The objective of simulating the vocal fold with idealized geometry is to verify the reduced-order flow model as the tissue stiffness properties are changed. Therefore, we do not consider the anisotropic tissue behavior or a multi-layer structure as proposed in many previous works [31, 38, 35] which would be better representation of the real tissue. Instead, the vocal fold here is assumed to be isotropic and homogeneous, and is governed by a hyperelastic, two-parameter Mooney−Rivlin model. The Mooney−Rivlin model is one of popular models for representing large deformations of soft tissues. The strain energy density function for this model is given as

$$\mathcal{W} = \alpha_{10}(\overline{I}_1 - 3) + \alpha_{01}(\overline{I}_2 - 3) + K/2(J-1)^2 \tag{6.5}$$

where K represents the bulk modulus, α_{10} and α_{01} are material constants, and $J = \det(F)$ with F standing for the deformation gradient. In addition, $\overline{I}_1$ and $\overline{I}_2$ are invariants based on J and the principal stretches of the deformation gradient. Further detail of this model for the vocal fold can be found in our group's previous work [53]. To verify the reduced-order model, idealized vocal folds with different tissue properties (α_{10} and α_{01}) are employed. The tissue density is $\rho_s = 1040$ kg/m^3 and mass damping is 0.05 s^{-1} for all the cases. The air density is $\rho = 1.13$ kg/m^3. Thus, the characteristic intraglottal velocity is $V = \sqrt{2(P_0 - P_{out})/\rho} = 42.1$ m/s. We define the jet Reynolds number using $Re_J = \rho V d/\mu$, where $d \sim 1$ mm is the characteristic glottal gap during opening phase and μ is the air viscosity. In the current study, we set $Re_J = 210$. If the channel height is used in the definition of the Reynolds number, we have $Re = 4200$.

A finite-element method is used to solve the tissue deformation [53]. The mesh for each vocal fold band includes approximately 18,000 20-nodes hexahedral elements and 80,000 vertex nodes. For 3D FSI simulations, an in-house immersed-boundary method is employed for the flow simulation [53, 60]. A nonuniform Cartesian grid with $320 \times 98 \times 72$ points, and time step size $\Delta t = 0.0025$ centisecond (cs) are used for spatial and temporal discretization, respectively. A mesh-independent study is performed with the medial thickness $T = 3.5$ mm and $\alpha_{10} = 2.29$ kPa and $\alpha_{01} = 0.25$ kPa in the Mooney−Rivlin model. The non-uniform grid is doubled in the region around the vocal fold and the time step is is decreased to $\Delta t = 0.002$ cs. Comparing the results from the two different meshes, a relative difference of 2.0% is obtained between the baseline mesh and the fine mesh for the vibration frequency, 4.5% for the vibration amplitude, and 3.9% for the phase delay between the inferior or superior points on the medial surface. Therefore, the baseline mesh is deemed satisfactory for further investigations of the idealized vocal fold in this work. For the hybrid FSI simulations, the FEM model of the vocal fold remains the same, but the flow is replaced by the 1D flow model described in Section 2.1 and the 1D flow pressure is simply interpolated onto the vocal fold surface according to the x-location of the point on the surface.

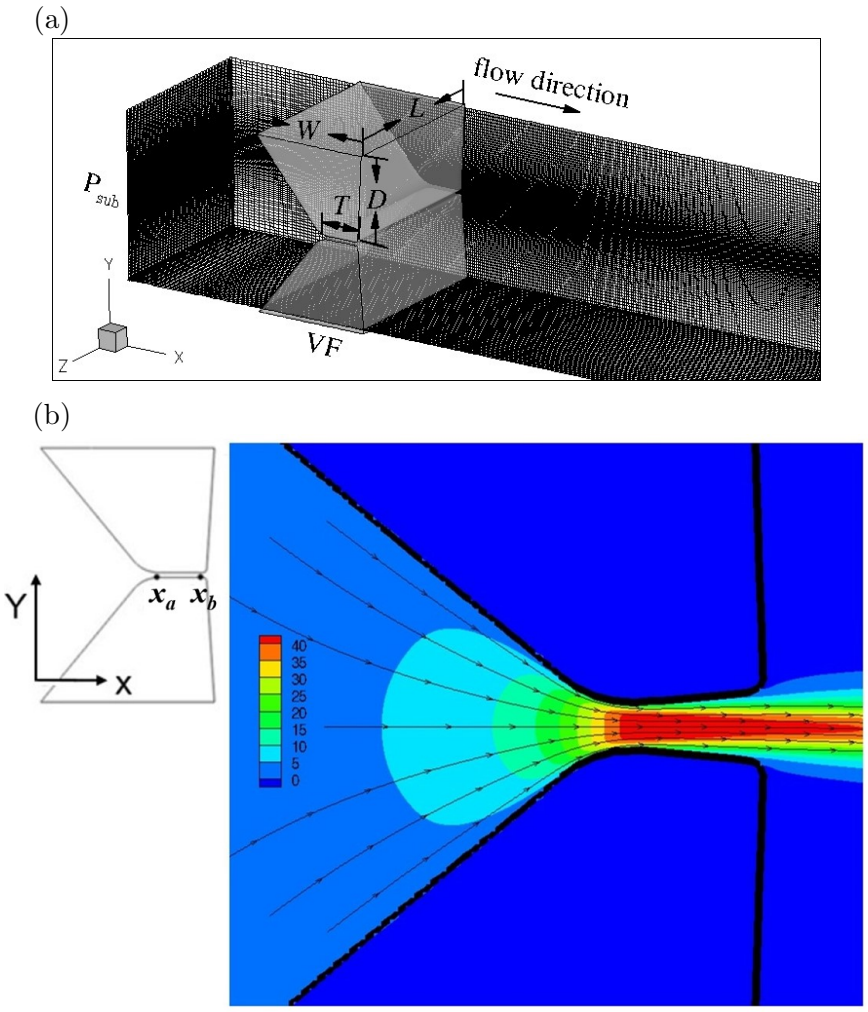

Figure 6.2: (a) The idealized vocal fold for FSI simulations. (b) Streamlines and contours of the velocity magnitude within the mid-plane when the vocal fold is open. The flow data is obtained from a 3D simulation with $T = 1.75$ mm, and it is used to determine the area correction coefficient, $\alpha(x)$.

6.2.3 Subject-specific vocal fold models based on MRI data

We also use the anatomical vocal models developed in a previous work of ours [48] and combine them with the present 1D flow model to perform FSI simulation. We will validate the results against the available experiment data from the specific samples that are associated with these anatomical models. The experimental procedure as well as creation of the vocal fold model were previously described in Chang et al. [48]. We only summarize the major steps here to provide sufficient context for the present study.

First, an *in vivo* phonation experiment was performed using rabbits. In the experiment, five live male New Zealand white breeder rabbits were used, and their vocal fold were sutured for adduction [2]. Phonation was evoked by pressurized air introduced from the trachea, and vocal fold vibration was captured with a high-speed camera (KayPENTAX, Montvale, NJ) at 10,000 frames per second. The subglottal pressure, volume flow rate, and acoustic intensity were recorded in acoustic and aerodynamic measurements. More details about the experiment procedure can be in Ge et al. [136] and Novalske et al. [2].

After the phonation experiment, the rabbit larynx was excised and high-resolution MRI was performed to obtain details of morphology of the vocal fold while the vocal fold maintained the adducted phonatory position. Multislice images in the axial, coronal, and sagittal planes were captured with a Varian 9.4 T horizontal bore imaging system (Varian Inc, Palo Alto, CA). Acquired data were reconstructed in MATLAB using an inverse Fourier transform. Details of the scanning procedure were described in [135].

The 3D anatomical vocal fold model was generated for each of the five samples after manual segmentation from the MRI data and surface mesh reduction/smoothing [135]. Figure 6.3 shows such geometrical model of the larynx reconstructed from MRI data for sample 1. We can see internal and external surfaces of the larynx from different views in Fig. 6.3(a) and (b). Two layers of the internal structure of the vocal fold tissue were identified from the images [135]. These are the vocal fold cover and body in the reconstructed model as shown in Fig. 6.3(c), and they have different stiffness properties.

In Chang et al. [135], an iterative procedure was used to estimate the stiffness properties of the vocal fold. Specifically, the vocal fold tissue was assumed to be isotropic and governed by the Saint Venant−Kirchhoff model [130, 53] with the density $\rho_s = 1000$ kg/m^3 and Poissons ratio of 0.3. The Young's moduli of the cover and body layers in each of the five samples were determined by attempting to match the vibration frequency and amplitude of the FSI simulation with those obtained from the high-speed imaging data. In the FSI simulation, a Bernoulli based flow model was used for the FSI simulation whose flow path and separation location have been calibrated using a representative 3D simulation using initial guesses of the vocal fold properties through an eigenfrequency analysis. Fig. 6.4 shows the streamlines in different views from the vocal fold at open phase for sample 1. A segment of the streamline at the center shown in Fig. 6.4(a) was taken, along which the 1D flow model was applied (thus the x-coordinate in Eq. (6.1) represents the

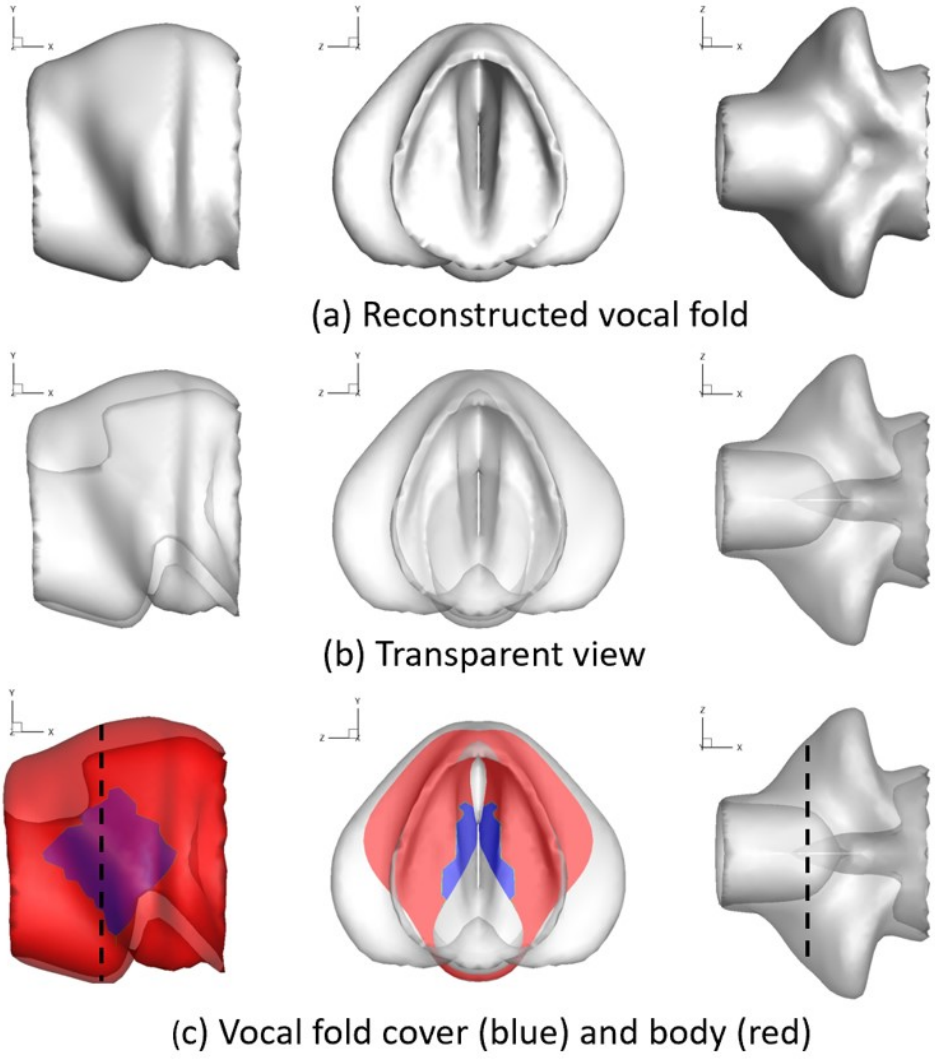

Figure 6.3: Reconstructed larynx geometry from a rabbit larynx sample. The dashed lines in left and right figures of (c) indicate the position of the slice seen in the middle.

arc length along the curved streamline). The same approach was repeated for the other samples. Fig. 6.4(c) shows the velocity magnitude in a slice parallel to the flow path in the glottis when the vocal fold is at opening position. Within the glottis, the flow is concentrated to the center instead of following the exact shape of vocal fold surface. Therefore, it is necessary to include the entrance effect as discussed in Section 2.1. For these anatomical models, we set $C_1 = 0.4$ in Eq. (6.4) for $\alpha(x)$ based on the flow data from representative 3D simulations.

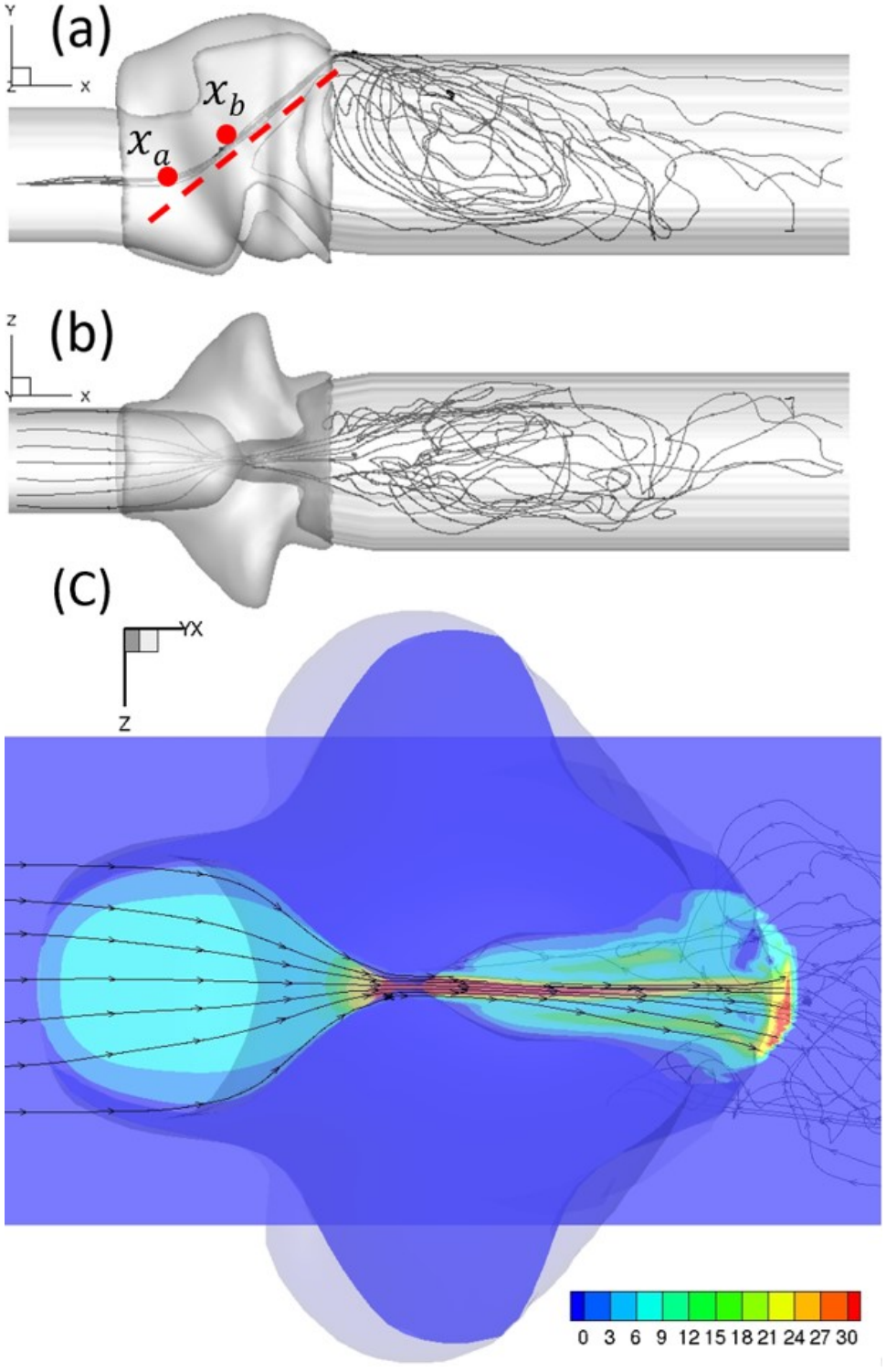

Figure 6.4: Streamlines at the vocal fold open phase from the 3D FSI simulation. The view in (c) is for a slice indicated by the dashed line in (a), where the color contours represent the velocity magnitude (m/s).

6.3 Results and discussions

6.3.1 Comparison of reduced-order and 3D simulations for idealized vocal fold models

3D FSI simulation can provide most detailed information about the tissue deformation and flow field, such as the vibration pattern and vortex structures in the entire 3D domain. For the reduced-order flow model developed in this study, the 1D flow representation is employed along the centerline from the inlet of flow path to the exit of glottis. Therefore, the 3D flow information such as vortices is completely ignored. On the other hand, the tissue model in the hybrid FSI and that in the 3D FSI are the same. The goal of the present reduced-order flow model is to produce vibratory characteristics that are as close as possible to those from the full 3D FSI model.

The case setups are listed in Tab. 6.1, where we consider two options for the medial thickness T and three options for the stiffness properties. Since the two-parameter Mooney−Rivlin model is employed to describe the tissue behavior, the constants α_{01} and α_{10} are simply multiplied by a factor of 1, 2, or 3 for the baseline, intermediate, or the stiffest case. The vibration frequency of the vocal fold for each case is between 100 and 300 Hz, as will be seen later. For all these cases, the pressure recovery coefficient $\chi_{min} = 0.5$, and the entrance effect coefficient $C_1 = 0.25$ in Eq. (6.4) are chosen in the 1D flow model, including $T = 1.75$ and 3.5 mm. As described in Section 2.1, the coefficient C_1 is determined based on the 3D flow data of the same vocal fold model.

Figure 6.5 shows a comparison of the vibration pattern in the mid-plane $z = 0$ for three stiffness cases and the small thickness of $T = 1.75$ mm. In each case, one steady vibration cycle is shown from both the hybrid FSI and the 3D FSI, while the dashed lines indicate the initial position and the solid lines indicate the deformed position. It can be seen that the second vibration mode is established in both hybrid FSI and 3D FSI simulations for all three cases, where the vocal fold oscillation is primarily in the lateral or y-direction. From case S1 to case S3, the amount of deformation keeps decreasing due to the increased tissue stiffness. The hybrid model agrees reasonably well with 3D FSI for all the three cases. Figure 6.6 shows a quantitative comparison of these cases, including the vibration amplitude, vibration frequency, and phase delay. The vibration amplitude is the maximum y-displacement of the vocal fold measured at the glottal exit in a cycle. In the figure, the amplitude decreases with increasing tissue stiffness as expected since the subglottal pressure is fixed. In case 3 where the tissue is the stiffest, the vocal fold has little deformation. The frequency increases with the tissue stiffness. The phase delay is calculated using the temporal difference between the glottal inlet and the exit in the mid-plane in terms of displacement. As the tissue stiffness is varied, the phase delay does not change much and remains around zero, indicating the glottal inlet and exit have mostly in-phase motion. The in-phase motion is also consistent with the vibration pattern in Fig. 6.5. From the figure, we see that for all three stiffness cases, the hybrid FSI model shows good agreement with the 3D FSI model regarding the amplitude, frequency, and phase delay.

Figure 6.7 shows a comparison of the vibration pattern between the hybrid model and the 3D

Table 6.1: Case setup for the idealized vocal fold with different thicknesses and stiffness constants

T (mm)	Case	α_{10} (kPa)	α_{01} (kPa)
34em1.75	S1	2.29	0.25
	S2	4.58	0.50
	S3	9.16	1.00
34em3.50	L1	2.29	0.25
	L2	4.58	0.50
	L3	9.16	1.00

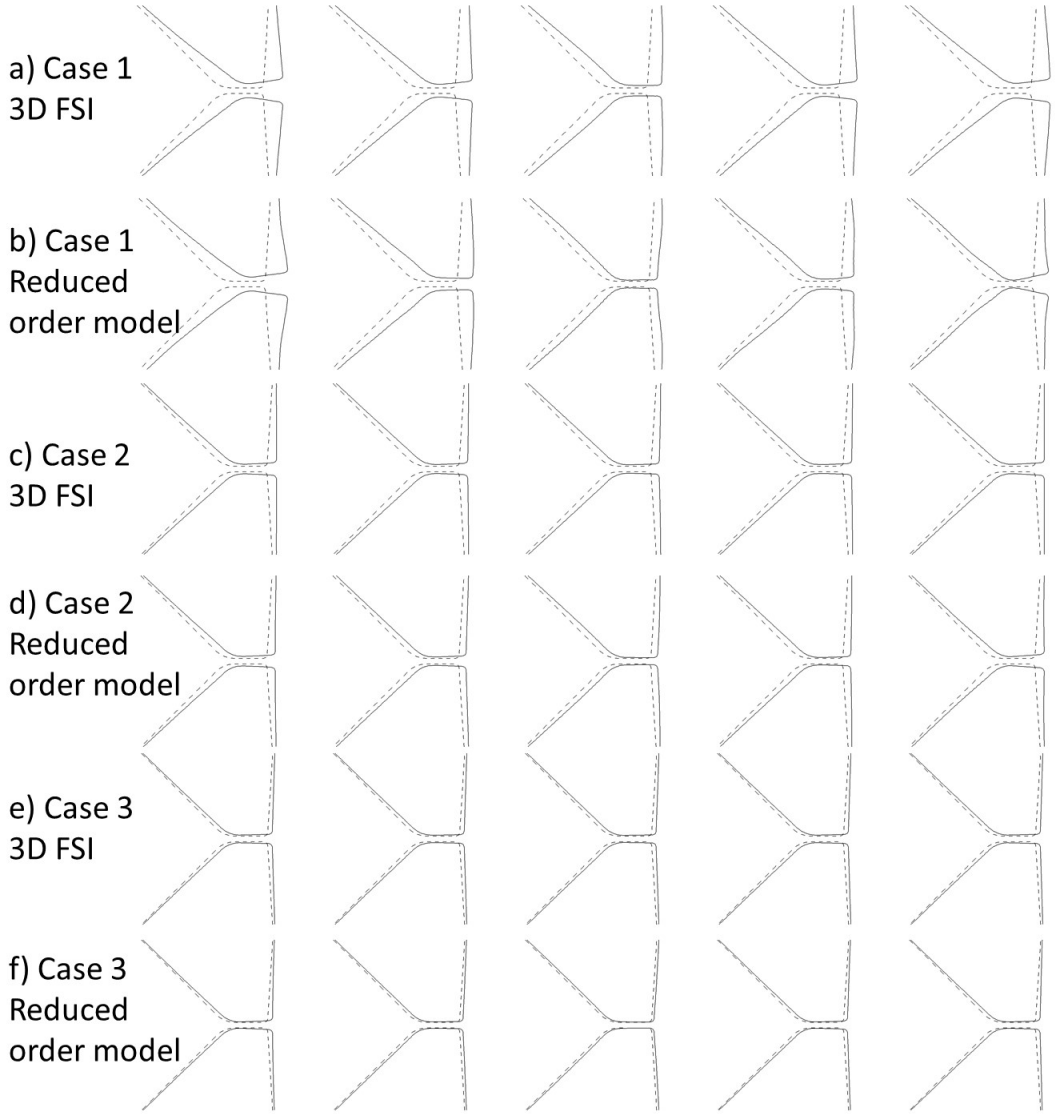

Figure 6.5: Comparison of vibration pattern for small thickness of $T = 1.75$ mm between the hybrid FSI and full 3D FSI simulations.

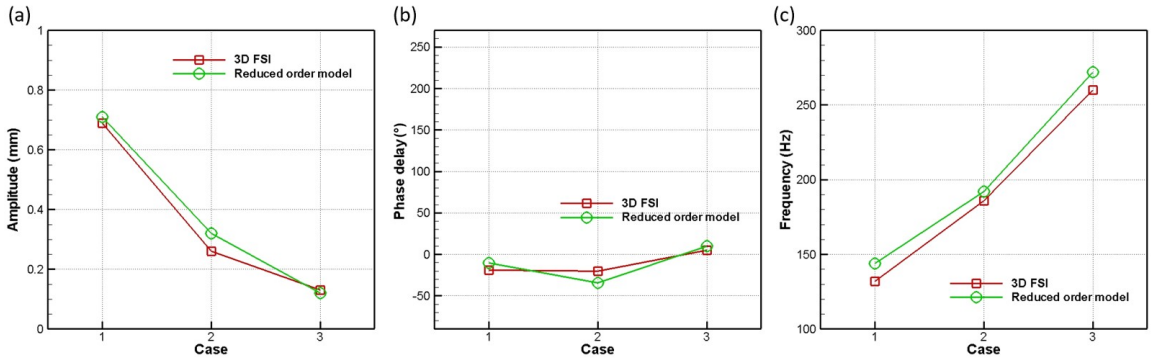

Figure 6.6: Comparison of vibration amplitude, phase delay, and frequency for small thickness of $T = 1.75$ mm between the hybrid FSI and full 3D FSI simulations.

FSI for large thickness case of $T = 3.5$ mm. All three cases display a second-mode dominant vibration pattern, and the deformation produced by the reduced-order flow model agrees very well with the 3D model for all three stiffness cases. Figure 6.8 shows a quantitative comparison of the vibration amplitude, vibration frequency, and phase delay. In the figure, the overall effect of the tissue stiffness on the vibration amplitude and frequency is similar to that in the small thickness cases. That is, as the stiffness is increased from case L1 to case L3, the vibration amplitude decreases and the frequency increases. At the same stiffness, the large thickness case displays greater vibration amplitude than the small thickness case. In particular, the vibration amplitude is around 1.0 mm, 0.6 mm, and 0.4 mm for cases L1, L2, and L3, respectively, but it is 0.7 mm, 0.3 mm, and 0.1 mm for cases S1, S2, and S3, respectively. Furthermore, the phase delay in the three large T cases is close to 180°, meaning the glottal inlet and exit have nearly an out-of-phase motion. On the other hand, the vibration frequency is very close between the large thickness and small thickness cases when the tissue stiffness is the same, which indicates that the geometrical difference between the two medial thicknesses does not affect much the vibration frequency but has significant effects on other vibratory characteristics such as the vibration amplitude and phase delay. Finally, Fig. 6.8 shows that the hybrid FSI model agrees well with the 3D FSI model for all stiffness cases.

6.3.2 Comparison between reduced-order simulation of subject-specific vocal fold models and experimental data

To further evaluate the performance of the reduced-order flow model in more practical applications, we utilize the previously constructed subject-specific vocal fold models from MRI data of rabbits and couple them with the 1D flow equation described in Section 2.1. The results of hybrid FSI simulations will be compared directly with the available experimental data for model validation.

Data from five animal samples are used in this study, which includes the FEM model of each vocal fold and *in vivo* experimental data for the subglottal pressure and high-speed measurement

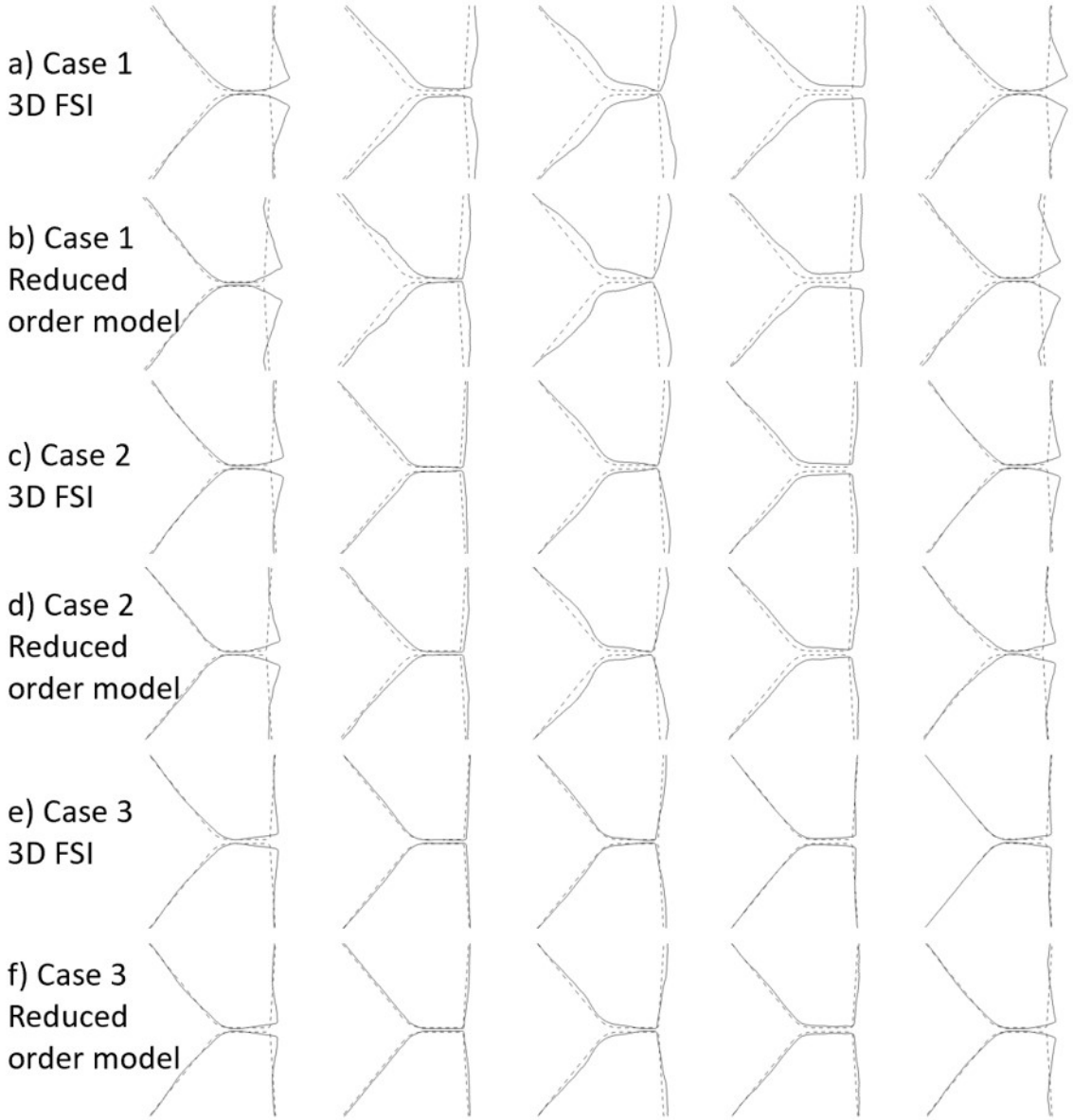

Figure 6.7: Comparison of vibration pattern for large thickness of $T = 3.5$ mm between the hybrid FSI and full 3D FSI simulations.

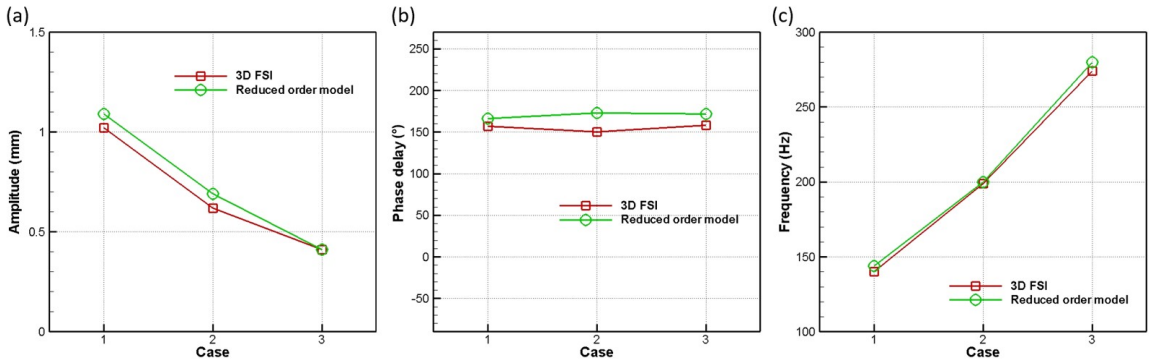

Figure 6.8: Comparison of vibration amplitude, phase delay, and frequency for large thickness of $T = 3.5$ mm between the hybrid FSI and full 3D FSI simulations.

Table 6.2: Subglottal pressure P_0 and Young's moduli of each rabbit sample (E_b for the vocal fold body and E_c for the cover)

Sample	P_0 (kPa)	E_b (kPa)	E_c (kPa)
R1	1.05	60	12
R2	0.78	80	8
R3	0.72	80	8
R4	1.00	90	9
R5	0.95	90	9

of the vibratory characteristics. As discussed in Section 2.3, the vocal fold was assumed to include two structural layers: body and cover, with corresponding Young's modulus E_b and E_c. These parameters have been estimated previously for each vocal fold sample [48] and are listed here in Table 6.2 along with the subglottal pressure used in the *in vivo* experiment, P_0. For all these cases, the pressure recovery coefficient $\chi_{min} = 0.1$ and the entrance effect coefficient $C_1 = 0.4$ are used in the reduced-order flow model. Compared with the idealized geometries, a higher C_1 (or stronger entrance effect) and lower pressure recovery are used here because the diverging section of the rabbit glottis has a greater expansion ratio.

In each animal experiment, the vocal fold was manually adducted by suturing and adjusting the tension between the thyroid and cricoid cartilages until phonation was audibly perceived [2]. Thus, the internal tension and tissue stiffness vary significantly from sample to sample. Furthermore, the anatomy and vocal fold morphology also contain significant individual variations. Thus, these samples provide a set of meaningful study cases to test accuracy and robustness of the present reduced-order modeling approach. Figure 6.9(a) shows a representative high-speed montage from one cycle of vocal fold vibration for rabbit sample R1, which is from a superior view of the glottis. From the figure, only slight vocal fold collision is observed during vocal fold closure for this sample. Figure 6.9(b) shows one vibration cycle from the hybrid FSI simulation using the present 1D flow

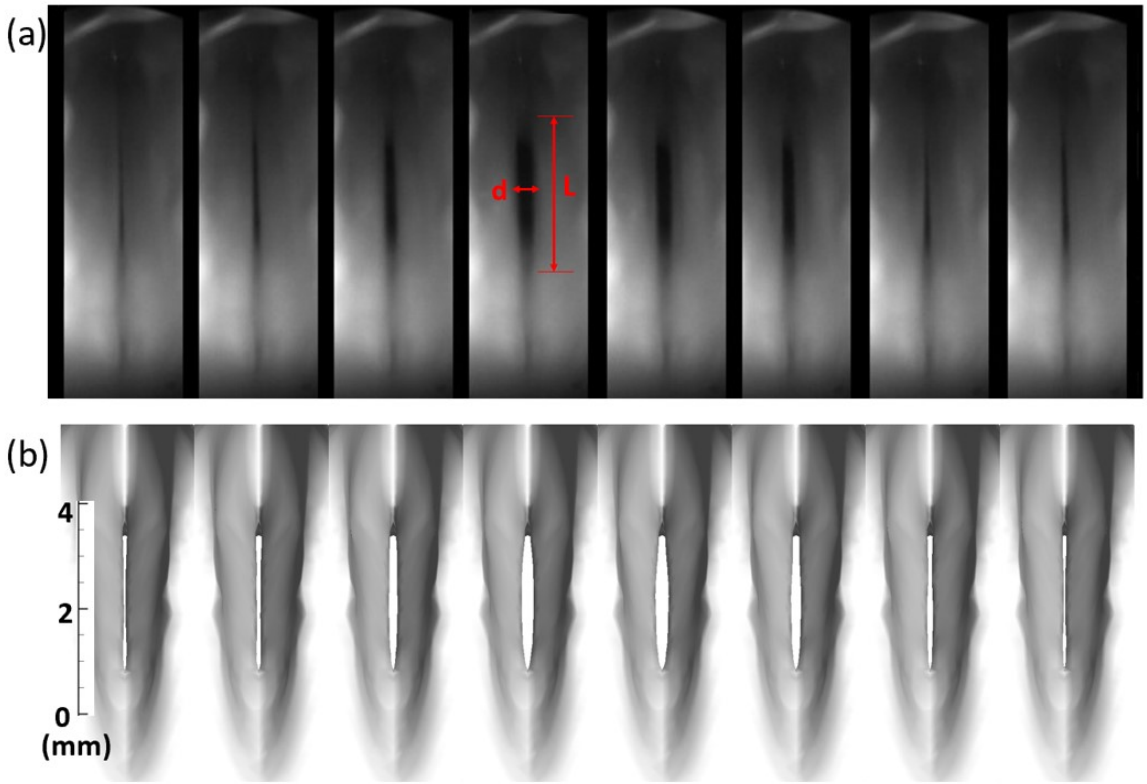

Figure 6.9: Comparison of vibration pattern comparison between the present hybrid FSI simulation and the high-speed imaging in the experiment [2] for sample R1. The vocal fold length L and gap width d are shown.

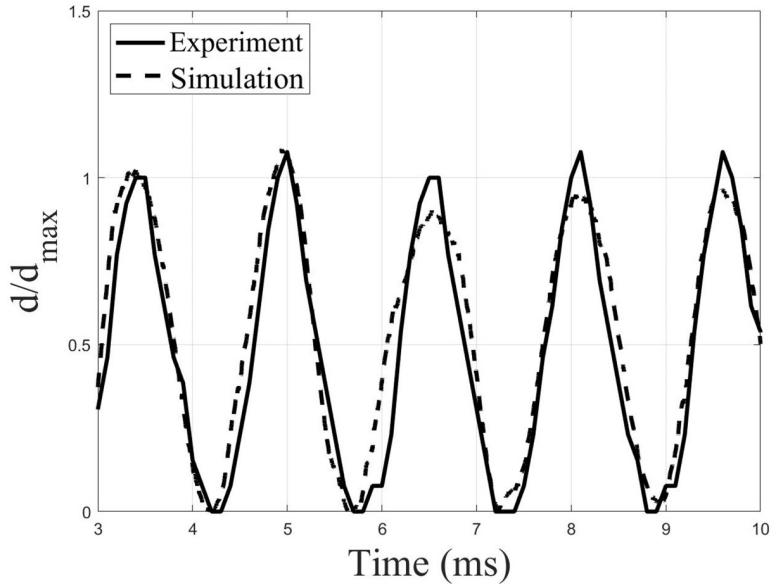

Figure 6.10: Waveforms of the normalized glottal gap width from the experiment and simulation for rabbit sample R1.

model and the corresponding reconstructed 3D anatomical vocal fold model. It can be seen that the dynamical shape of the glottis from the simulation in general agrees well with that from the experiment for both opening and closing phases. Similar comparisons between experimental and simulation results are also achieved for the other four rabbit samples.

Figure 6.10 shows a comparison of the the normalized glottal gap width in a sequence of vocal fold oscillations between the simulation and experiment. The gap width d is normalized by the average peak magnitudes d_{max} so that we can focus on comparison of the waveform. Note that the high-speed imaging does not provide a length scale. Thus, using a normalized length also facilitates comparison between the simulation and the high-speed data. From the figure, it can be seen that the waveform obtained from the simulation agrees well with the experiment. We further compute the normalized root-mean-square (r.m.s.) error of the waveform between the simulation and experiment and list the data for all five samples in Tab. 6.3. The results show that the error is within 17%. Thus, the simulated waveform from the hybrid FSI model is reasonably close to the that from the experiment. Figure 6.11 shows a quantitative comparison between experiment and numerical simulation for all 5 samples in terms vibration frequency and normalized amplitude, d_{max}/L, where L is the vocal fold length. From the figure, the frequency and amplitude from the simulation fall into the ranges of experimental results for all the five samples despite significant variations among the individuals. All these results indicate that the present hybrid FSI simulations agree with the experiment for the individual samples.

Finally, we point out that there are a few limitations in the current study. First of all, the entrance effect is determined through an empirical manner using the 3D simulation data. A more generalized approach for arbitrary vocal fold geometry would be more preferable. Second, in this

Table 6.3: The normalized r.m.s. error of the gap width waveform for each rabbit sample

Sample	R1	R2	R3	R4	R5
Error	14.3%	11.3%	15.3%	15.9%	16.9%

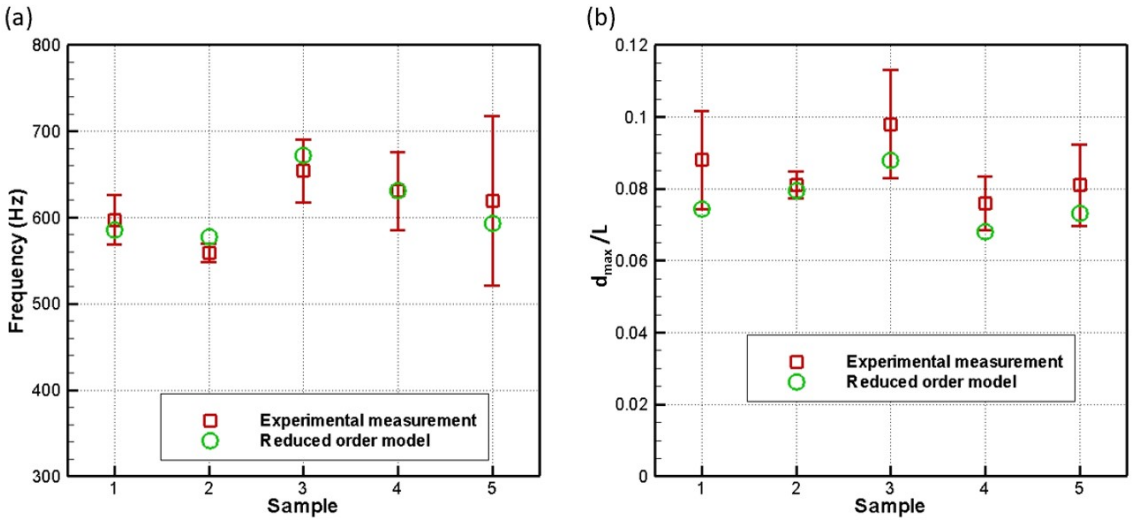

Figure 6.11: Frequency and amplitude comparison between experimental and numerical results for five samples.

study we consider only healthy vocal fold only which is symmetric, and extension of the current modeling approach to asymmetric vocal fold under disease condition, e.g., unilateral vocal fold paralysis, needs further exploration. Third, the vocal fold model in the current study was based on *ex vivo* MRI scan, and it would be desirable to construct the model from an *in vivo* scan for clinical applications. These issues will be investigated in future studies.

6.4 Chapter conclusion

In this study, we have presented a reduced-order flow model and its application for FSI simulation of vocal fold vibration. The drastically simplified flow model is based on 1D mass and momentum conservation equations but also includes the entrance effect within the glottis. The energy loss and partial pressure recovery in the divergent section of the glottis have been taken into account in the model. We test performance of this model in two scenarios: 1) idealized vocal fold geometries and 3D FSI simulation by an immersed-boundary method being used as benchmarks, and 2) subject-specific models constructed from MRI data of rabbit vocal folds and *in vivo* experimental data being directly used as benchmarks for validation. In the first scenario, the medial thickness and tissue stiffness are varied, and in the second scenario, five rabbit samples were used in the study. In all these tests, after coupling the reduced-order flow model with the 3D FEM model of the vocal fold tissue, the resulting FSI simulations demonstrate good agreements with

the benchmarks in vibratory characteristics. Thus, the present reduced-order flow model shows promises in application of patient specific modeling of vocal fold vibration.

Chapter VII

Conclusions and future directions

In this dissertation, we have advanced a high-fidelity simulation tool for the computational modeling of fluid–structure interaction (FSI) problems, especially those involving complex anatomy and large deformation of soft tissues in human body. The flow simulation in this tool is based on Cartesian grid and an immersed-boundary approach that allows efficient calculations on high-performance computers. To accelerate the three-dimensional flow simulation, we have implemented a parallel algorithm based on the idea of domain decomposition in either 1D, 2D, or 3D. Specific implementation issues related to the immersed-boundary method have been addressed. The code was tested using benchmark problems and was shown to scale up to several thousand of processor cores. Practical applications in the hummingbird's flapping flight and biomedical flows in vocal fold and heart valves were demonstrated.

We applied the FSI method first to the aortic valve and studied the valve deformation in relation to blood flow characteristics as well as the force on the valve. In particular, we used 3D FSI simulations to investigate the effect of bending rigidity on the deformation pattern, flow rate, valve resistance, and vortex behavior in the flow. From these results, we identified an optimal range of the bending rigidity that is normalized by the pressure gradient along the aorta. From the insight of surface pressure distribution, we further developed a one-dimensional transient flow model by incorporating the leaflet movement and pressure loss. When combined with the 3D valve model, the reduced-order flow model was shown to produce reasonable results in terms of valve opening and closing, as well as flow rate.

We also applied the FSI method to the vocal fold vibration problem with the overarching goal of surgery planning for voice disorders. In this application, we also developed a one-dimensional flow model to describe the transient airflow through glottis and the intraglottal pressure. We used 3D FSI simulations to test the 1D model and assess its performance in predicting the vocal fold's vibratory characteristics. The reduced-order flow model was also extended to subject-specific laryngeal anatomy and was validated against *in vivo* phonation experiment.

In summary, our FSI simulation tools, including both 3D high-fidelity and reduced-order models, have been successfully applied to the computational modeling of heart valve and vocal fold.

For future directions, more sophisticated models can be built on these simulation tools. For the aortic valve, realistic geometry of the aorta based on the actual anatomy can be incorporated

into our model to study the hemodynamics and its interaction with the valve. In addition, the left ventricle's motion and mitral valve can be added to our model to conduct FSI simulation of the entire left heart. For vocal fold vibration, asymmetric vocal fold models with the implant inserted into the tissue can be numerically studied with the current FSI simulation tools. In both heart valve and vocal fold cases, the hyperelastic and anisotropic material properties of soft tissues could be another possible topic for the future FSI study. Overall, these simulation studies will serve to provide useful means in clinical diagnosis, medical device design, and surgical planning.

Bibliography

[1] Ye Chen and Haoxiang Luo. A computational study of the three-dimensional fluid–structure interaction of aortic valve. *Journal of Fluids and Structures*, 80:332–349, 2018.

[2] Carolyn K Novaleski, Tsuyoshi Kojima, Siyuan Chang, Haoxiang Luo, Carla V Valenzuela, and Bernard Rousseau. Nonstimulated rabbit phonation model: Cricothyroid approximation. *The Laryngoscope*, 126(7):1589–1594, 2016.

[3] David Kamensky, Ming-Chen Hsu, Dominik Schillinger, John A Evans, Ankush Aggarwal, Yuri Bazilevs, Michael S Sacks, and Thomas JR Hughes. An immersogeometric variational framework for fluid–structure interaction: Application to bioprosthetic heart valves. *Computer methods in applied mechanics and engineering*, 284:1005–1053, 2015.

[4] Frederick J Schoen and Robert J Levy. Calcification of tissue heart valve substitutes: progress toward understanding and prevention. *The Annals of thoracic surgery*, 79(3):1072–1080, 2005.

[5] Philippe Pibarot and Jean G Dumesnil. Prosthetic heart valves: selection of the optimal prosthesis and long-term management. *Circulation*, 119(7):1034–1048, 2009.

[6] Liang Ge and Fotis Sotiropoulos. A numerical method for solving the 3d unsteady incompressible navier–stokes equations in curvilinear domains with complex immersed boundaries. *Journal of computational physics*, 225(2):1782–1809, 2007.

[7] LP Dasi, L Ge, HA Simon, Fotis Sotiropoulos, and AP Yoganathan. Vorticity dynamics of a bileaflet mechanical heart valve in an axisymmetric aorta. *Physics of Fluids*, 19(6):067105, 2007.

[8] Iman Borazjani, Liang Ge, and Fotis Sotiropoulos. Curvilinear immersed boundary method for simulating fluid structure interaction with complex 3d rigid bodies. *Journal of Computational physics*, 227(16):7587–7620, 2008.

[9] R Van Loon. Towards computational modelling of aortic stenosis. *International Journal for Numerical Methods in Biomedical Engineering*, 26(3-4):405–420, 2010.

[10] Boyce E Griffith. Immersed boundary model of aortic heart valve dynamics with physiological driving and loading conditions. *International Journal for Numerical Methods in Biomedical Engineering*, 28(3):317–345, 2012.

[11] Iman Borazjani. Fluid–structure interaction, immersed boundary-finite element method simulations of bio-prosthetic heart valves. *Computer Methods in Applied Mechanics and Engineering*, 257:103–116, 2013.

[12] Gil Marom, Mor Peleg, Rotem Halevi, Moshe Rosenfeld, Ehud Raanani, Ashraf Hamdan, and Rami Haj-Ali. Fluid-structure interaction model of aortic valve with porcine-specific collagen fiber alignment in the cusps. *Journal of biomechanical engineering*, 135(10):101001, 2013.

[13] Wei Wu, Desiree Pott, Beniamino Mazza, Tommaso Sironi, Elena Dordoni, Claudio Chiastra, Lorenza Petrini, Giancarlo Pennati, Gabriele Dubini, Ulrich Steinseifer, et al. Fluid–structure interaction model of a percutaneous aortic valve: comparison with an in vitro test and feasibility study in a patient-specific case. *Annals of biomedical engineering*, 44(2):590–603, 2016.

[14] Vittoria Flamini, Abe DeAnda, and Boyce E Griffith. Immersed boundary-finite element model of fluid–structure interaction in the aortic root. *Theoretical and computational fluid dynamics*, 30(1-2):139–164, 2016.

[15] Wenbin Mao, Andrés Caballero, Raymond McKay, Charles Primiano, and Wei Sun. Fully-coupled fluid-structure interaction simulation of the aortic and mitral valves in a realistic 3d left ventricle model. *PloS one*, 12(9):e0184729, 2017.

[16] Aymen Laadhari and Gábor Székely. Eulerian finite element method for the numerical modeling of fluid dynamics of natural and pathological aortic valves. *Journal of Computational and Applied Mathematics*, 319:236–261, 2017.

[17] Andrés Caballero, Wenbin Mao, Raymond McKay, and Wei Sun. The impact of balloon-expandable transcatheter aortic valve replacement on concomitant mitral regurgitation: a comprehensive computational analysis. *Journal of the Royal Society Interface*, 16(157): 20190355, 2019.

[18] Peter de Jaegere, Giorgia Rocatello, Bernard D Prendergast, Ole de Backer, Nicolas M Van Mieghem, and Ronak Rajani. Patient-specific computer simulation for transcatheter cardiac interventions: what a clinician needs to know. *Heart*, 105(Suppl 2):s21–s27, 2019.

[19] J De Hart, FPT Baaijens, GWM Peters, and PJG Schreurs. A computational fluid-structure interaction analysis of a fiber-reinforced stentless aortic valve. *Journal of biomechanics*, 36 (5):699–712, 2003.

[20] Boyce E Griffith, Xiaoyu Luo, David M McQueen, and Charles S Peskin. Simulating the fluid dynamics of natural and prosthetic heart valves using the immersed boundary method. *International Journal of Applied Mechanics*, 1(01):137–177, 2009.

[21] Anvar Gilmanov, Trung Bao Le, and Fotis Sotiropoulos. A numerical approach for simulating fluid structure interaction of flexible thin shells undergoing arbitrarily large deformations in complex domains. *Journal of Computational Physics*, 300:814–843, 2015.

[22] Anvar Gilmanov and Fotis Sotiropoulos. Comparative hemodynamics in an aorta with bicuspid and trileaflet valves. *Theoretical and Computational Fluid Dynamics*, 30(1-2):67–85, 2016.

[23] Ming-Chen Hsu, David Kamensky, Fei Xu, Josef Kiendl, Chenglong Wang, Michael CH Wu, Joshua Mineroff, Alessandro Reali, Yuri Bazilevs, and Michael S Sacks. Dynamic and fluid–structure interaction simulations of bioprosthetic heart valves using parametric design with t-splines and fung-type material models. *Computational mechanics*, 55(6):1211–1225, 2015.

[24] Wenbin Mao, Kewei Li, and Wei Sun. Fluid–structure interaction study of transcatheter aortic valve dynamics using smoothed particle hydrodynamics. *Cardiovascular engineering and technology*, 7(4):374–388, 2016.

[25] Ingo R Titze and Daniel W Martin. Principles of voice production, 1998.

[26] Rajat Mittal, Byron D Erath, and Michael W Plesniak. Fluid dynamics of human phonation and speech. *Annual Review of Fluid Mechanics*, 45:437–467, 2013.

[27] NIDCD. National institute on deafness and other communication disorders, 2007.

[28] MP De Vries, HK Schutte, AEP Veldman, and GJ Verkerke. Glottal flow through a two-mass model: comparison of navier–stokes solutions with simplified models. *The Journal of the Acoustical Society of America*, 111(4):1847–1853, 2002.

[29] Jack J Jiang and Yu Zhang. Chaotic vibration induced by turbulent noise in a two-mass model of vocal folds. *The Journal of the Acoustical Society of America*, 112(5):2127–2133, 2002.

[30] Byron D Erath, Matías Zañartu, Kelley C Stewart, Michael W Plesniak, David E Sommer, and Sean D Peterson. A review of lumped-element models of voiced speech. *Speech Communication*, 55(5):667–690, 2013.

[31] Fariborz Alipour, David A Berry, and Ingo R Titze. A finite-element model of vocal-fold vibration. *The Journal of the Acoustical Society of America*, 108(6):3003–3012, 2000.

[32] Eric J Hunter, Ingo R Titze, and Fariborz Alipour. A three-dimensional model of vocal fold abduction/adduction. *The Journal of the Acoustical Society of America*, 115(4):1747–1759, 2004.

[33] Douglas D Cook and Luc Mongeau. Sensitivity of a continuum vocal fold model to geometric parameters, constraints, and boundary conditions. *The Journal of the Acoustical Society of America*, 121(4):2247–2253, 2007.

[34] James S Drechsel and Scott L Thomson. Influence of supraglottal structures on the glottal jet exiting a two-layer synthetic, self-oscillating vocal fold model. *The Journal of the Acoustical Society of America*, 123(6):4434–4445, 2008.

[35] Zhaoyan Zhang. Effect of vocal fold stiffness on voice production in a three-dimensional body-cover phonation model. *The Journal of the Acoustical Society of America*, 142(4):2311–2321, 2017.

[36] Scott L Thomson, Luc Mongeau, and Steven H Frankel. Aerodynamic transfer of energy to the vocal folds. *The Journal of the Acoustical Society of America*, 118(3):1689–1700, 2005.

[37] Haoxiang Luo, Rajat Mittal, Xudong Zheng, Steven A Bielamowicz, Raymond J Walsh, and James K Hahn. An immersed-boundary method for flow–structure interaction in biological systems with application to phonation. *Journal of computational physics*, 227(22):9303–9332, 2008.

[38] Haoxiang Luo, Rajat Mittal, and Steven A Bielamowicz. Analysis of flow-structure interaction in the larynx during phonation using an immersed-boundary method. *The Journal of the Acoustical Society of America*, 126(2):816–824, 2009.

[39] X Zheng, Qian Xue, R Mittal, and S Beilamowicz. A coupled sharp-interface immersed boundary-finite-element method for flow-structure interaction with application to human phonation. *Journal of biomechanical engineering*, 132(11):111003, 2010.

[40] Erik R Swanson, Davood Abdollahian, Tsunehisa Ohno, Pingjiang Ge, David L Zealear, and Bernard Rousseau. Characterization of raised phonation in an evoked rabbit phonation model. *The Laryngoscope*, 119(7):1439–1443, 2009.

[41] Erik R Swanson, Tsunehisa Ohno, Dave Abdollahian, and Bernard Rousseau. Effects of raised-intensity phonation on inflammatory mediator gene expression in normal rabbit vocal fold. *OtolaryngologyHead and Neck Surgery*, 143(4):567–572, 2010.

[42] Qian Xue, Xudong Zheng, Rajat Mittal, and Steven Bielamowicz. Subject-specific computational modeling of human phonation. *The Journal of the Acoustical Society of America*, 135 (3):1445–1456, 2014.

[43] Rajat Mittal, Xudong Zheng, Rajneesh Bhardwaj, Jung Hee Seo, Qian Xue, and Steven Bielamowicz. Toward a simulation-based tool for the treatment of vocal fold paralysis. *Frontiers in physiology*, 2:19, 2011.

[44] Fariborz Alipour, Christoph Brucker, Douglas D Cook, Andreas Gommel, Manfred Kaltenbacher, Willy Mattheus, Luc Mongeau, Eric Nauman, Rudiger Schwarze, Isao Tokuda, et al. Mathematical models and numerical schemes for the simulation of human phonation. *Current Bioinformatics*, 6(3):323–343, 2011.

[45] Siyuan Chang, Carolyn K Novaleski, Tsuyoshi Kojima, Masanobu Mizuta, Haoxiang Luo, and Bernard Rousseau. Subject-specific computational modeling of evoked rabbit phonation. *Journal of biomechanical engineering*, 138(1):011005, 2016.

[46] Abie H Mendelsohn and Zhaoyan Zhang. Phonation threshold pressure and onset frequency in a two-layer physical model of the vocal folds. *The Journal of the Acoustical Society of America*, 130(5):2961–2968, 2011.

[47] Gifford Z Decker and Scott L Thomson. Computational simulations of vocal fold vibration: Bernoulli versus navier–stokes. *Journal of Voice*, 21(3):273–284, 2007.

[48] Siyuan Chang. *Computational Fluid-structure Interaction for Vocal Fold Modeling*. PhD thesis, Vanderbilt University, 2016.

[49] Satyajit Marawar, Federico P Girardi, Andrew A Sama, Yan Ma, Licia K Gaber-Baylis, Melanie C Besculides, and Stavros G Memtsoudis. National trends in anterior cervical fusion procedures. *Spine*, 35(15):1454–1459, 2010.

[50] Charles S Peskin. Flow patterns around heart valves: a numerical method. *Journal of computational physics*, 10(2):252–271, 1972.

[51] Charles S Peskin. Numerical analysis of blood flow in the heart. *Journal of computational physics*, 25(3):220–252, 1977.

[52] Boyce E Griffith and Neelesh A Patankar. Immersed methods for fluid–structure interaction. *Annual Review of Fluid Mechanics*, 52, 2020.

[53] Fang-Bao Tian, Hu Dai, Haoxiang Luo, James F Doyle, and Bernard Rousseau. Fluid–structure interaction involving large deformations: 3d simulations and applications to biological systems. *Journal of computational physics*, 258:451–469, 2014.

[54] Ye Chen and Haoxiang Luo. Pressure distribution over the leaflets and effect of bending stiffness on fluid–structure interaction of the aortic valve. *Journal of Fluid Mechanics*, 883, 2020.

[55] Jialei Song, Bret W Tobalske, Donald R Powers, Tyson L Hedrick, and Haoxiang Luo. Three-dimensional simulation for fast forward flight of a calliope hummingbird. *Royal Society open science*, 3(6):160230, 2016.

[56] Edward Givelberg and K Yelick. Distributed immersed boundary simulation in titanium. *SIAM Journal on Scientific Computing*, 28(4):1361–1378, 2006.

[57] B Yildirim, Sun Lin, Sanjay Mathur, and Jayathi Y Murthy. A parallel implementation of fluid–solid interaction solver using an immersed boundary method. *Computers & Fluids*, 86: 251–274, 2013.

[58] Jeffrey K Wiens and John M Stockie. An efficient parallel immersed boundary algorithm using a pseudo-compressible fluid solver. *Journal of Computational Physics*, 281:917–941, 2015.

[59] Vamsi Spandan, Valentina Meschini, Rodolfo Ostilla-Mónico, Detlef Lohse, Giorgio Querzoli, Marco D de Tullio, and Roberto Verzicco. A parallel interaction potential approach coupled with the immersed boundary method for fully resolved simulations of deformable interfaces and membranes. *Journal of computational physics*, 348:567–590, 2017.

[60] Haoxiang Luo, Hu Dai, Paulo JSA Ferreira de Sousa, and Bo Yin. On the numerical oscillation of the direct-forcing immersed-boundary method for moving boundaries. *Computers & Fluids*, 56:61–76, 2012.

[61] Jialei Song, Haoxiang Luo, and Tyson L Hedrick. Three-dimensional flow and lift characteristics of a hovering ruby-throated hummingbird. *Journal of The Royal Society Interface*, 11 (98):20140541, 2014.

[62] Zheng Li, Ye Chen, Siyuan Chang, and Haoxiang Luo. A reduced-order flow model for fluid–structure interaction simulation of vocal fold vibration. *Journal of biomechanical engineering*, 142(2), 2020.

[63] Rajat Mittal, Haibo Dong, Meliha Bozkurttas, FM Najjar, Abel Vargas, and Alfred von Loebbecke. A versatile sharp interface immersed boundary method for incompressible flows with complex boundaries. *Journal of computational physics*, 227(10):4825–4852, 2008.

[64] James DeBonis. Solutions of the taylor-green vortex problem using high-resolution explicit finite difference methods. In *51st AIAA Aerospace Sciences Meeting including the New Horizons Forum and Aerospace Exposition*, page 382, 2013.

[65] Andrea D Beck and Gregor J Gassner. Numerical simulation of the taylor-green vortex at re= 1600 with the discontinuous galerkin spectral element method for well-resolved and underresolved scenarios. In *1st International Workshop on High-Order CFD Methods at the 50th AIAA Aerospace Sciences Meeting, Nashville, TN*, 2012.

[66] Zheng Li, Ye Chen, Siyuan Chang, and Haoxiang Luo. A reduced-order flow model for fluid–structure interaction simulation of vocal fold vibration. *Journal of biomechanical engineering*, 142(2), 2020.

[67] BJ Bellhouse, FH Bellhouse, and KG Reid. Fluid mechanics of the aortic root with application to coronary flow. *Nature*, 219(5158):1059–1061, 1968.

[68] Rainer G Leyh, Claudia Schmidtke, Hans-Hinrich Sievers, and Magdi H Yacoub. Opening and closing characteristics of the aortic valve after different types of valve-preserving surgery. *Circulation*, 100(21):2153–2160, 1999.

[69] Andrea Salica, Giuseppe Pisani, Umberto Morbiducci, Raffaele Scaffa, Diana Massai, Alberto Audenino, Luca Weltert, Lorenzo Guerrieri Wolf, and Ruggero De Paulis. The combined role of sinuses of valsalva and flow pulsatility improves energy loss of the aortic valve. *European Journal of Cardio-Thoracic Surgery*, 49(4):1222–1227, 2015.

[70] W Milton Swanson and Richard E Clark. Dimensions and geometric relationships of the human aortic value as a function of pressure. *Circulation research*, 35(6):871–882, 1974.

[71] H Reul, A Vahlbruch, M Giersiepen, TH Schmitz-Rode, V Hirtz, and S Effert. The geometry of the aortic root in health, at valve disease and after valve replacement. *Journal of biomechanics*, 23(2):181185–183191, 1990.

[72] A.A.H.J Sauren. The mechanical behaviour of the aortic valve. *Ph.D. Thesis*, pages 2153–2160, 1981.

[73] J Li, XY Luo, and ZB Kuang. A nonlinear anisotropic model for porcine aortic heart valves. *Journal of biomechanics*, 34(10):1279–1289, 2001.

[74] Eli J Weinberg and Mohammad R Kaazempur-Mofrad. On the constitutive models for heart valve leaflet mechanics. *Cardiovascular Engineering*, 5(1):37–43, 2005.

[75] R Rukmani and R Usha. Arbitrary squeeze flow between two disks. *International Journal of Mathematics and Mathematical Sciences*, 17(4):779–782, 1994.

[76] Matthieu Hillairet. Lack of collision between solid bodies in a 2d incompressible viscous flow. *Communications in Partial Differential Equations*, 32(9):1345–1371, 2007.

[77] John E Hall. *Guyton and Hall Textbook of Medical Physiology E-Book*. Elsevier Health Sciences, 2015.

[78] Ajit P Yoganathan, Zhaoming He, and S Casey Jones. Fluid mechanics of heart valves. *Annu. Rev. Biomed. Eng.*, 6:331–362, 2004.

[79] K Peck, J Wang, J Shaw, and A Dart. Aortic valve area (ava) and dimensionless performance index (dpi) predicts progression of aortic stenosis. *Heart, Lung and Circulation*, 25:S265–S266, 2016.

[80] MJ Thubrikar, JL Heckman, and SP Nolan. High speed cine-radiographic study of aortic valve leaflet motion. *The Journal of heart valve disease*, 2(6):653–661, 1993.

[81] Giulia Luraghi, Wei Wu, Francesco De Gaetano, Josè Felix Rodriguez Matas, Geoff D Moggridge, Marta Serrani, Joanna Stasiak, Maria Laura Costantino, and Francesco Migliavacca. Evaluation of an aortic valve prosthesis: Fluid-structure interaction or structural simulation? *Journal of Biomechanics*, 2017.

[82] Roland Fries, Thomas Graeter, Diana Aicher, Helmut Reul, Christoph Schmitz, Michael Böhm, and Hans-Joachim Schäfers. In vitro comparison of aortic valve movement after valve-preserving aortic replacement. *The Journal of Thoracic and Cardiovascular Surgery*, 132(1): 32–37, 2006.

[83] EJ Gutmark and FF Grinstein. Flow control with noncircular jets. *Annual review of fluid mechanics*, 31(1):239–272, 1999.

[84] Shozo Koshigoe, Ephraim Gutmark, Klaus C Schadow, and Arnold Tubis. Initial development of noncircular jets leading to axis switching. *AIAA journal*, 27(4):411–419, 1989.

[85] Atieh Yousefi, David L Bark, and Lakshmi P Dasi. Effect of arched leaflets and stent profile on the hemodynamics of tri-leaflet flexible polymeric heart valves. *Annals of biomedical engineering*, 45(2):464–475, 2017.

[86] Michael Markl, Mary T Draney, D Craig Miller, Jonathan M Levin, Eric E Williamson, Norbert J Pelc, David H Liang, and Robert J Herfkens. Time-resolved three-dimensional magnetic resonance velocity mapping of aortic flow in healthy volunteers and patients after valve-sparing aortic root replacement. *The Journal of thoracic and cardiovascular surgery*, 130(2):456–463, 2005.

[87] David Kamensky, Ming-Chen Hsu, Yue Yu, John A Evans, Michael S Sacks, and Thomas JR Hughes. Immersogeometric cardiovascular fluid–structure interaction analysis with divergence-conforming b-splines. *Computer methods in applied mechanics and engineering*, 314:408–472, 2017.

[88] Yongyuth Sahasakul, William D Edwards, James M Naessens, and A Jamil Tajik. Age-related changes in aortic and mitral valve thickness: implications for two-dimensional echocardiography based on an autopsy study of 200 normal human hearts. *American Journal of Cardiology*, 62(7):424–430, 1988.

[89] John O Dabiri. Optimal vortex formation as a unifying principle in biological propulsion. *Annual Review of Fluid Mechanics*, 41:17–33, 2009.

[90] Michael S Sacks, David B Smith, and Erik D Hiester. The aortic valve microstructure: effects of transvalvular pressure. *Journal of Biomedical Materials Research: An Official Journal of The Society for Biomaterials, The Japanese Society for Biomaterials, and the Australian Society for Biomaterials*, 41(1):131–141, 1998.

[91] W David Merryman, Hsiao-Ying Shadow Huang, Frederick J Schoen, and Michael S Sacks. The effects of cellular contraction on aortic valve leaflet flexural stiffness. *Journal of biomechanics*, 39(1):88–96, 2006.

[92] Wei Sun, Caitlin Martin, and Thuy Pham. Computational modeling of cardiac valve function and intervention. *Annual review of biomedical engineering*, 16:53–76, 2014.

[93] Ming-Chen Hsu, David Kamensky, Yuri Bazilevs, Michael S Sacks, and Thomas JR Hughes. Fluid–structure interaction analysis of bioprosthetic heart valves: significance of arterial wall deformation. *Computational mechanics*, 54(4):1055–1071, 2014.

[94] J De Hart, GWM Peters, PJG Schreurs, and FPT Baaijens. Collagen fibers reduce stresses and stabilize motion of aortic valve leaflets during systole. *Journal of biomechanics*, 37(3): 303–311, 2004.

[95] MD De Tullio, A Cristallo, E Balaras, and R Verzicco. Direct numerical simulation of the pulsatile flow through an aortic bileaflet mechanical heart valve. *Journal of Fluid Mechanics*, 622:259–290, 2009.

[96] Jung Hee Seo, Vijay Vedula, Theodore Abraham, Albert C Lardo, Fady Dawoud, Hongchang Luo, and Rajat Mittal. Effect of the mitral valve on diastolic flow patterns. *Physics of fluids*, 26(12):121901, 2014.

[97] Ajit P Yoganathan, Aurelio Chaux, Richard J Gray, Yi-Ren Woo, Michele DeRobertis, Frank P Williams, and Jack M Matloff. Bileaflet, tilting disc and porcine aortic valve substitutes: in vitro hydrodynamic characteristics. *Journal of the American College of Cardiology*, 3(2 Part 1):313–320, 1984.

[98] Choon Hwai Yap, Neelakantan Saikrishnan, Gowthami Tamilselvan, and Ajit P Yoganathan. Experimental technique of measuring dynamic fluid shear stress on the aortic surface of the aortic valve leaflet. *Journal of biomechanical engineering*, 133(6):061007, 2011.

[99] Neelakantan Saikrishnan, Lucia Mirabella, and Ajit P Yoganathan. Bicuspid aortic valves are associated with increased wall and turbulence shear stress levels compared to trileaflet aortic valves. *Biomechanics and modeling in mechanobiology*, 14(3):577–588, 2015.

[100] Morteza Gharib, Edmond Rambod, Arash Kheradvar, David J Sahn, and John O Dabiri. Optimal vortex formation as an index of cardiac health. *Proceedings of the National Academy of Sciences*, 103(16):6305–6308, 2006.

[101] Réka Faludi, Mariola Szulik, Jan D'hooge, Paul Herijgers, Frank Rademakers, Gianni Pedrizzetti, and Jens-Uwe Voigt. Left ventricular flow patterns in healthy subjects and patients with prosthetic mitral valves: an in vivo study using echocardiographic particle image velocimetry. *The Journal of thoracic and cardiovascular surgery*, 139(6):1501–1510, 2010.

[102] Partho P Sengupta, Gianni Pedrizzetti, Philip J Kilner, Arash Kheradvar, Tino Ebbers, Giovanni Tonti, Alan G Fraser, and Jagat Narula. Emerging trends in cv flow visualization. *JACC: Cardiovascular Imaging*, 5(3):305–316, 2012.

[103] John J Charonko, Rahul Kumar, Kelley Stewart, William C Little, and Pavlos P Vlachos. Vortices formed on the mitral valve tips aid normal left ventricular filling. *Annals of biomedical engineering*, 41(5):1049–1061, 2013.

[104] Umberto Morbiducci, Raffaele Ponzini, Giovanna Rizzo, Marcello Cadioli, Antonio Esposito, Francesco De Cobelli, Alessandro Del Maschio, Franco Maria Montevecchi, and Alberto Redaelli. In vivo quantification of helical blood flow in human aorta by time-resolved three-dimensional cine phase contrast magnetic resonance imaging. *Annals of biomedical engineering*, 37(3):516, 2009.

[105] Alex J Barker, Craig Lanning, and Robin Shandas. Quantification of hemodynamic wall shear stress in patients with bicuspid aortic valve using phase-contrast mri. *Annals of biomedical engineering*, 38(3):788–800, 2010.

[106] Anvar Gilmanov, Alexander Barker, Henryk Stolarski, and Fotis Sotiropoulos. Image-guided fluid-structure interaction simulation of transvalvular hemodynamics: Quantifying the effects of varying aortic valve leaflet thickness. *Fluids*, 4(3):119, 2019.

[107] Damien Garcia and Lyes Kadem. What do you mean by aortic valve area: geometric orifice area, effective orifice area, or gorlin area? *Journal of Heart Valve Disease*, 15(5):601, 2006.

[108] Damien Garcia, Lyes Kadem, David Savéry, Philippe Pibarot, and Louis-Gilles Durand. Analytical modeling of the instantaneous maximal transvalvular pressure gradient in aortic stenosis. *Journal of biomechanics*, 39(16):3036–3044, 2006.

[109] Alison L Marsden and Mahdi Esmaily-Moghadam. Multiscale modeling of cardiovascular flows for clinical decision support. *Applied Mechanics Reviews*, 67(3):030804, 2015.

[110] Kewei Li and Wei Sun. Simulated thin pericardial bioprosthetic valve leaflet deformation under static pressure-only loading conditions: implications for percutaneous valves. *Annals of biomedical engineering*, 38(8):2690–2701, 2010.

[111] Kristen L Billiar and Michael S Sacks. Biaxial mechanical properties of the native and glutaraldehyde-treated aortic valve cusp: part iia structural constitutive model. *Journal of biomechanical engineering*, 122(4):327–335, 2000.

[112] Rong Fan and Michael S Sacks. Simulation of planar soft tissues using a structural constitutive model: finite element implementation and validation. *Journal of biomechanics*, 47(9):2043–2054, 2014.

[113] J Doyle. Qed: static, dynamic, stability, and nonlinear analysis of solids and structures. *Software manual, version*, 4, 2008.

[114] James F Doyle. *Guided explorations of the mechanics of solids and structures*. Cambridge University Press, 2009.

[115] Hiromi Nakai, Masaaki Takeuchi, Hidetoshi Yoshitani, Kyoko Kaku, Nobuhiko Haruki, and Yutaka Otsuji. Pitfalls of anatomical aortic valve area measurements using two-dimensional transoesophageal echocardiography and the potential of three-dimensional transoesophageal echocardiography. *European Journal of Echocardiography*, 11(4):369–376, 2009.

[116] Paul Schoenhagen, Jörg Hausleiter, Stephan Achenbach, Milind Y Desai, and E Murat Tuzcu. Computed tomography in the evaluation for transcatheter aortic valve implantation (tavi). *Cardiovascular diagnosis and therapy*, 1(1):44, 2011.

[117] Takafumi Machida, Masaki Izumo, Kengo Suzuki, Kihei Yoneyama, Ryo Kamijima, Kei Mizukoshi, Manabu Takai, Yasuyuki Kobayashi, Tomoo Harada, Fumihiko Miyake, et al. Value of anatomical aortic valve area using real-time three-dimensional transoesophageal echocardiography in patients with aortic stenosis: a comparison between tricuspid and bicuspid aortic valves. *European Heart Journal-Cardiovascular Imaging*, 16(10):1120–1128, 2015.

[118] Jeannette H Spühler, Johan Jansson, Niclas Jansson, and Johan Hoffman. 3d fluid-structure interaction simulation of aortic valves using a unified continuum ale fem model. *Frontiers in physiology*, 9, 2018.

[119] Gillian M Bernacca, Bernard OConnor, David F Williams, and David J Wheatley. Hydrodynamic function of polyurethane prosthetic heart valves: influences of young's modulus and leaflet thickness. *Biomaterials*, 23(1):45–50, 2002.

[120] Michael J Shelley and Jun Zhang. Flapping and bending bodies interacting with fluid flows. *Annual Review of Fluid Mechanics*, 43:449–465, 2011.

[121] M Abbasi and AN Azadani. Stress analysis of transcatheter aortic valve leaflets under dynamic loading: Effect of reduced tissue thickness. *The Journal of heart valve disease*, 26(4):386–396, 2017.

[122] Ali Mirnajafi, Brett Zubiate, and Michael S Sacks. Effects of cyclic flexural fatigue on porcine bioprosthetic heart valve heterograft biomaterials. *Journal of Biomedical Materials Research Part A: An Official Journal of The Society for Biomaterials, The Japanese Society for Biomaterials, and The Australian Society for Biomaterials and the Korean Society for Biomaterials*, 94(1):205–213, 2010.

[123] Claudio Cancelli and TJ Pedley. A separated-flow model for collapsible-tube oscillations. *Journal of Fluid Mechanics*, 157:375–404, 1985.

[124] Peter Anderson, Sidney Fels, and Sheldon Green. Implementation and validation of a 1d fluid model for collapsible channels. *Journal of biomechanical engineering*, 135(11):111006, 2013.

[125] Arvind Vasudevan, Victor Zappi, Peter Anderson, and Sidney Fels. A fast robust 1d flow model for a self-oscillating coupled 2d fem vocal fold simulation. In *INTERSPEECH*, pages 3482–3486, 2017.

[126] Matthias Heil and Andrew L Hazel. Fluid-structure interaction in internal physiological flows. *Annual review of fluid mechanics*, 43:141–162, 2011.

[127] XY Luo and TJ Pedley. A numerical simulation of unsteady flow in a two-dimensional collapsible channel. *Journal of Fluid Mechanics*, 314:191–225, 1996.

[128] Natasha Mirza, Cesar Ruiz, Eric D Baum, and Jeffrey P Staab. The prevalence of major psychiatric pathologies in patients with voice. *Ear, nose & throat journal*, 82:10, 2003.

[129] Timothy E Shurtz and Scott L Thomson. Influence of numerical model decisions on the flow-induced vibration of a computational vocal fold model. *Computers & structures*, 122: 44–54, 2013.

[130] Siyuan Chang, Fang-Bao Tian, Haoxiang Luo, James F Doyle, and Bernard Rousseau. The role of finite displacements in vocal fold modeling. *Journal of Biomechanical Engineering*, 135(11):111008, 2013.

[131] Jubiao Yang, Xingshi Wang, Michael Krane, and Lucy T Zhang. Fully-coupled aeroelastic simulation with fluid compressibilityfor application to vocal fold vibration. *Computer methods in applied mechanics and engineering*, 315:584–606, 2017.

[132] Jubiao Yang, Feimi Yu, Michael Krane, and Lucy T Zhang. The perfectly matched layer absorbing boundary for fluid–structure interactions using the immersed finite element method. *Journal of fluids and structures*, 76:135–152, 2018.

[133] Fariborz Alipour, Eileen M Finnegan, and Sanyukta Jaiswal. Phonatory characteristics of the excised human larynx in comparison to other species. *Journal of Voice*, 27(4):441–447, 2013.

[134] Kosuke Ishii, Wei G Zhai, Masumi Akita, and Hajime Hirose. Ultrastructure of the lamina propria of the human vocal fold. *Acta oto-laryngologica*, 116(5):778–782, 1996.

[135] Siyuan Chang, Carolyn K. Novaleski, Tsuyoshi Kojima, Masanobu Mizuta, Haoxiang Luo, and Bernard Rousseau. Subject-Specific Computational Modeling of Evoked Rabbit Phonation. *Journal of Biomechanical Engineering*, 138(1):011005, 2015.

[136] Ping Jiang Ge, Lesley C French, Tsunehisa Ohno, David L Zealear, and Bernard Rousseau. Model of evoked rabbit phonation. *Annals of Otology, Rhinology & Laryngology*, 118(1): 51–55, 2009.